IMAGING AND CHARACTERIZING THE CORROSION OF NITINOL AND ALUMINUM *IN SITU*

by

Bradley Garrett LeGallais

Submitted in partial fulfilment of the requirements
for the degree of Master of Science

at

Dalhousie University
Halifax, Nova Scotia
June 2018

Table of Contents

List of Tables

List of Figures

Abstract

In the first chapter, the corrosion resistance of mechanically polished and as received nitinol was characterized. Two treatments were applied to improve the corrosion resistance: placing samples in 90ºC distilled water and in a 3% solution of H_2O_2. Potentiodynamic cyclic voltammetry curves and measuring the mass loss in an aggressive solution were used to characterize the corrosion resistance. The H_2O_2 and water treatments were found to substantially improve the corrosion resistance. Nitinol discs were imaged during a cyclic voltammetry scan. This enabled us to characterize the corrosion mechanism in situ.

In the second chapter the effect of the electrolyte flow on the corrosion of aluminum 1100 and 5052 was investigated. Corrosion was found to be more severe when the sample was left in a still solution. The surface of Al 5052 was imaged during corrosion. We found flow did not affect the corrosion propagation mechanism.

List of Abbreviations and Symbols Used

Ag/AgCl: Silver-Silver Chloride Reference Electrode

AS: As Received

CCD: Charge-Coupled Device

CE: Chemically Etched

E^o: Standard Electrode Potential

EDS: Energy Dispersive X-Ray Spectroscopy

EP: Electropolished

FD: Fine Drawn

GIXRD: Grazing Incidence X-Ray Spectroscopy

H_2O_2: Hydrogen Peroxide Treated

PBS: Phosphate Buffered Saline

PE: Potential Energy

R: Universal Gas Constant

RCE: Rotating Cylindrical Electrode

SCE: Standard Calomel Electrode

SBF: Simulated Body Fluid

SEM: Scanning Electron Microscopy

SF: Sensitivity Factor

T: Temperature

WT: Water Treated

XPS: X-Ray Photoelectron Spectroscopy

z: Number of Electrons Transferred

α: Incident Grazing Angle

Θ: Angle of Reflection

ΔG: Gibbs Free Energy of Formation

μ: Linear Absorption Coefficient

Acknowledgments

I learned a lot during my time in the graduate program at Dalhousie which has allowed me to substantially improve my skills as a researcher. I would foremost like to thank my supervisor Dr. Harm Rotermund for his advice and support throughout my graduate studies and for making this research possible. I would like to give a huge thanks to, now, Dr. Eduardo Machado whose discussions taught me much about electrochemistry experiment and theory. As well, thanks are due to all past and present group members Mengnan Guo, David Alberico, Stefan Juckes, and Qifeng Tian whose support and insight made this work possible. Andy George had been essential to my work by performing the XPS study described in this paper. Dr. Jeff Dahn allowed me to make use of his groups XRD and distilled water machine which were both essential for this work. As well, he kindly donated his time to assist me in learning how to use the XRD. I would like to thank my committee members Dr. Daniel Labrie and Laurent Kreplak for their advice and their time.

Chapter 1: Introduction

In this thesis we will explore the corrosion properties of nitinol, in chapter 2, and aluminum, in chapter 3. Nitinol is an interesting implant material, that is used in various applications. It is generally held to have a high level of corrosion resistance but is known to widely vary with different surface treatments. In this study we will characterize the effects of the surface morphology on the corrosion resistance. As well, we will apply a treatment in boiling water and in a hydrogen peroxide solution to improve the corrosion resistance. The surface chemistry and structure will be investigated using x-ray photoelectron spectroscopy, x-ray diffraction, and scanning electron microscopy to ascertain the mechanism by which the corrosion resistance is improved. Finally, we will image, in real time, the surface of nitinol discs as they corrode to determine the corrosion propagation mechanism. To the best of our knowledge, real time videos of nitinol taken as it corrodes have never yet to be reported in the literature.

Chapter 3 deals with effects of electrolyte flow on the corrosion resistance of aluminum. The effects of flow on the corrosion of aluminum has not been heavily studied and the literature includes several conflicting reports. We will determine the effect both a still and a flowing electrolyte on the breakdown potential of aluminum, a higher breakdown potential is correlated with more corrosion resistance. Furthermore, we will image, in real time, the surface of an aluminum plate to determine the corrosion propagation mechanism and if this mechanism changes due to flow.

Chapter 2: Nitinol Corrosion

2.1 Introduction

2.1.1 History of Nitinol

Nitinol, an acronym for Nickel Titanium Naval Ordnance Laboratory, is an equitatomic alloy of nickel and titanium. This novel alloy was discovered by William J. Buelher in 1959; he was tasked with finding a material for the nose cone of Polaris submarine-launched ballistic missiles which could better resist a high temperature environment during re-entry. After casting, what would be called nitinol, Buelher noted that cool bars when dropped produced a leaden like sound. Bars warmed in boiling water rang with a bell-like quality signaling that this material had interesting properties due to a phase change. Subsequent tests found the material to have a high strength and to be very ductile [1]. During a meeting, a strip of folded nitinol was heated with a cigarette lighter and to the surprise of the audience the material retook its original shape [1]. The property of nitinol shape memory was discovered.

2.1.2 Shape Memory

Shape memory derives from a phase transition between the low temperature martensite and the high temperature austenite phases. Martensite is softer, and is much easier to deform compared to austensite, which has a much higher tensile strength. This phenomenon allows nitinol to experience a large degree of reversible strain unlike other metals such as steel or titanium. In the austenite phase the material is made up of two interlocking simple cubic structures. When the temperature falls a new and more complex martensite phase forms. Martensite is composed of a monoclinic structure, oP4 in Pearson notation [2]. Due to the complex martensite structure an applied stress

leads to twinning. Twinning is major a type of deformation where no atomic bonds are broken, unlike the movement of slip planes. Slip planes are close packed directions of the material where dislocation, slip, can most easily occur.

Nitinol heated to approximately 770 K will form new austenite bonds and "remember" that shape. After shape setting, when nitinol in then martensite phase is deformed and then heated the material will be restored to its original shape that it possessed prior to deformation. This phenomenon is known as "shape memory". So long as nitinol is not plastically deformed, the deformed martensite phase will revert to its original shape as the crystal structure changes to the austensite phase. Nitinol in the martensite phase is easily deformed due to twining allowing it to take on different forms. But, when martensite nitinol de-twins and converts back to austensite it is forced to take on its original shape, the only possible shape available. When nitinol is completely in the austensite phase and cooled to the martensite transition temperature some austensite will remain in a metastable state. The material needs to be cooled to the austensite finish temperature to convert all the remaining austensite to martensite. The same applies when martensite is heated and starts to form austensite. This leads to a hysteresis loop for nitinol's phase transition [3]. By altering the composition and by applying various mechanical treatments, the transition temperatures can range from 170 K to 370 K. Small, ~1%, changes in the nickel atomic concentration give rise to large changes in the martensite to austensite transition temperature. Typically, nitinol will have a hysteresis width between 30-50 K [4]. Superelastic nitinol is engineered to have a transition temperature such that a metastable austenite phase will be present at room or body temperature. When loaded the material will immediately convert all nitinol in the austensite phase into the more ductile martensite phase. Then when unloaded the

material will spontaneously revert to the austenite phase and change back to its original shape [2].

The first shape memory alloy, AuCd, was originally discovered in 1932, making it much older than nitinol, by Arne Ölander [5]. Besides nitinol there have been several other shape memory alloys discovered. These include the Cu based alloys CuAlNi and CuAnZl, Fe based alloys, and several other novel alloys. Cu and Fe alloys while cheaper, lack the ductility of nitinol, are less stable, and more brittle in comparison. Promising work has been done more recently alloying nitinol with either Zr, Hf, or Pd which could be useful for higher temperature applications requiring shape memory materials. Nitinol, as the premier shape memory material, has a plethora of applications including eyeglass frames, endontic files, orthodontic archwires, stents, and even heat engines [3]. Nitinol is practically immune to corrosion when halide ions, usually chloride ions, are not present. For medical implants such as orthodontic archwires and stents the corrosion properties of nitinol are substantially more acute due to the aggressive nature of the body [6]. The topic of this chapter in the thesis will be exploring the corrosion of nitinol by electrochemical tests and by imaging the corrosion in real time. As well, we will attempt to improve the corrosion resistance using some environmentally friendly surface treatments.

2.2 Literature Review

2.2.1 Localized Corrosion

When an oxide free surface on a passive metal is exposed to water corrosion occurs leading to positively charged metal cations passing from the metal into the solution. These metal cations leave behind free electrons in the material, this is known

as the anodic reaction in which base metal is oxidized. If the electrons are not removed via some other reaction the free electrons in the material will build up and create an electric field opposing the dissolution of the metal. Depending on the pH of the electrolyte different reduction reactions can occur to consume the free electrons. In acidic solutions hydrogen ions are reduced to hydrogen gas while in neutral and basic solutions water is reduced to hydrogen gas and a hydroxide anion, these collectively are known as the cathodic reactions. A further cathodic reaction can occur when oxygen is present producing either hydroxide ions or water, if the electrolyte is neutral or acidic respectively. Corrosion can continue to occur so long as the electrons are removed through these reactions. A steady state forms where the rate of anodic and cathodic reactions reach parity. The steady state potential that forms is known as the open circuit potential (E_{ocp}). The amount of material dissolved, from a passive metal, at the corrosion potential is usually of a negligible proportion. On a single electrode the anodic reaction will tend to occur in the most reactive regions. The most reactive regions are listed in order of increasing reactivity: crystal ledges, kinks, dislocations, high index grain faces, impurities grain boundaries, inclusions, second phases, and crevices [7]. Localized corrosion occurs when the anodic and cathodic regions do not shift across the surface, this is known as general corrosion, but remain localized to their respective regions. Passive materials such as stainless steel and nitinol exhibit measurable mass loss only when the electrode is polarized in the anodic direction. As the electrode potential becomes more positive, polarized in the anodic direction, the rate of the anodic reaction will start to increase [7].

The two main types of localized corrosion are crevice and pitting corrosion. These modes of corrosion are far more insidious than general corrosion since they can cause failure due to low levels of mass loss and are exceptionally difficult to detect.

Crevice corrosion is caused by the differential concentration of oxygen inside and outside of a crevice. For example, crevice corrosion is commonly found inside of gaps in junctions or around bolts. Oxygen reduction occurs wherever the metal surface is exposed to the electrolyte. But, as oxygen is consumed in a crevice the amount of oxygen available for reduction is limited by diffusion; outside of the crevice oxygen is much more readily available:

$$O_2 + 2H_2O + 4e^- \rightarrow 4OH^- \quad (1)$$

This differential concentration of oxygen has two effects: metal exposed to lower concentrations of oxygen have more anodic potentials and the limiting current density for oxygen reduction is decreased in comparison to the surface. The Nernst equation can be used to calculate the reduction potential of the reaction. shown in Eq. 2, for different concentrations of oxygen. The Nernst equation is given as:

$$E(O_2) = E^0 - \frac{RT}{zF} ln\left(\frac{[OH^-]^4}{[O_2]}\right) \quad (2)$$

where E^0 is the standard reduction potential, z is the number of electrons transferred, R is the universal gas constant, F is the faraday constant. Calculating the reduction potentials for a 15 mg/L (a common bulk concentration) and 1 mg/L (concentration in a crevice) concentration of oxygen we find 1.596 V and 1.579 V, respectively [8]. The crevice will also become progressively more acidic as oxygen is depleted and a steady state is reached. Chlorine anions and metal cations, produced from corrosion, cannot easily diffuse out a crevice. Metal cations will then react with water molecules producing hydrogen ions decreasing the local pH:

$$M^{2+} + 2H_2O \rightarrow M(OH)_2 + 2H^+ \quad (3)$$

Summarizing, crevice corrosion initiates in a hole on the sample surface and due to the differential concentration of oxygen corrosion occurs. A lack of oxygen and a surplus of metal cations allow the internal electrolyte to become highly acidic and aggressive which induces the propagation of corrosion throughout the material. The initiation stage for crevice corrosion can be long but propagation usually proceeds very rapidly [8].

The other common form of localized corrosion is known as pitting corrosion. Pitting refers to the localized breakdown of the passive layer usually by chloride ions. A chloride ion is a strong Lewis base and interacts with Lewis acids, metal cations, which can initiate the dissolution of the passive layer. Chloride ions are relatively small and have a high diffusivity, they can easily penetrate the oxide layer [8]. There have been several mechanisms proposed to explain how halide anions initiate corrosion pits: the penetration mechanism, film thinning mechanism, and the film rupture mechanism. In the penetration mechanism, aggressive ions are transported through the oxide layer to the interface between the oxide and the metal. The aggressive anions migrate through oxygen vacancies to the interface. There the anions attack and dissolve the metal substrate underneath of the passive layer [9]. This mechanism works well to describe corrosion due to chloride ions, which are similar in size to oxygen atoms. But, both bromide and iodide are also known to initiate pitting corrosion and their larger size makes the penetration mechanism unfeasible as a general explanation. In the film thinning mechanism the aggressive anions adsorb onto the passive layer of the material forming a complex with the oxide, these complexes usually form in clusters. This leads to localized dissolution of the oxide layer until the metal matrix is exposed. The passive layer of aluminum has been found to thin under the presence of aggressive halide anions using XPS [10]. The final mechanism, the film rupture mechanism, proposes

that aggressive anions penetrate through cracks and flaws in the oxide layer. Further flaws are produced as chlorine ions diffuse into the film. These flaws in the oxide layer cannot extend all the way to the metal substrate since the metal would react with water and oxygen molecules and re-oxidize [11]. The anions must then penetrate the distance between the defect and the metal using the two previous mechanisms. These three mechanisms are by no means mutually exclusive and likely all contribute to the initiation of corrosion. Yu *et al.* found evidence that both the penetration and film thinning mechanisms played a key role in the corrosion of Aluminum in a NaCl solution [12].

Corrosion pits have a similar propagation mechanism to crevice corrosion. At the nucleation site corrosion begins underneath the oxide layer. The oxide layer cap, generally porous, prevents diffusion of metal cations and hydrogen ions out of the corrosion pit. Furthermore, halide anions will be electrostatically attracted into the corrosion pit to maintain charge neutrality due to the presence of metal cations released from corrosion. These metal cations react with water molecules to form hydrogen atoms which lowers the pH in the corrosion pit. Directly outside of the corrosion pit, oxygen reduction is driven by electrons freed by corrosion. Oxygen reduction increases the pH directly outside of the corrosion pit due to the production of hydroxide anions. The potential in the corrosion pit drops due to this phenomenon [8]. The pit quickly becomes supersaturated with both chlorine and metal cations which form a salt layer on the bottom of the pit [13]. Eventually as the pit grows the oxide layer cover will break due to an osmotic pressure difference across the cap. This removes the largest barrier to diffusion allowing the pit electrolyte to become diluted. When the oxide cover collapses the pit can either repassivate or continue to corrode; these corrosion modes are called metastable and stable pitting corrosion, respectively. This corrosion

mechanism is illustrated in figure 2.1 for an arbitrary metal undergoing pitting corrosion.

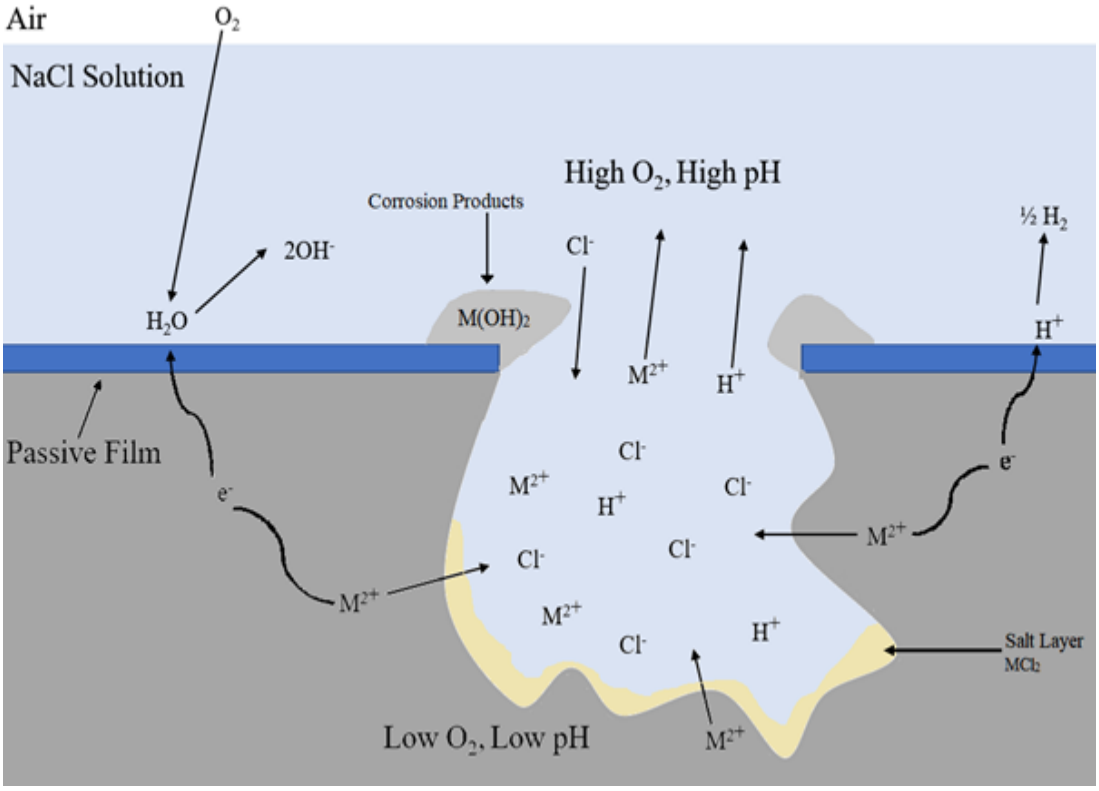

Figure 2.1: An illustration of the pitting corrosion mechanism for an arbitrary metal. Inside of the corrosion pit we find a low pH and a low concentration of oxygen. In the vicinity near the corrosion pit we find instead a high pH, due to the cathodic reaction producing hydroxide anions and hydrogen gas, and a high concentration of oxygen.

Stable corrosion pits form when the current density in the pit is greater than the pit stability product. This is a measurement of the aggressiveness of a pit and its ability to continue to corrode after diffusion with the bulk is no longer impeded [11]. Metastable pit growth is under diffusion control instead of ohmic control; this means the pit current density is independent of the electrode potential. However, a potential at which stable pitting starts to occur, the pitting potential, is known to exist; the fact that pit growth is under diffusion control should preclude a measurable pitting

potential. While metastable pits have current densities that are independent of the electrode potential Pistorius and Burnstein found that the distribution of pits with higher current densities shifts to a larger value with increasing electrode potential [13]. They also found that the number of nucleation sites available increases with the electrode potential. At lower potentials the available nucleation sites are constricted to regions covered by scratches and defects. As the electrode potential increases wider and shallower corrosion pits can form. Pistorius and Burnstein found pits with this morphology have a higher current density; they are more likely to pass the critical pit stability product, the product of the current density and depth, and therefore achieve pit stability [11].

2.2.2 Nitinol Implants

Nitinol is thought to have superior properties in terms of its corrosion resistance, biocompatibility, and elastic properties in comparison with other memory alloys [14]. Biocompatibility and corrosion resistance are especially important because the most notable application of nitinol and the catalyst for this research is its use in stents, which operate in the hostile environment of the body. Superelastic nitinol stents can be compressed and delivered to the occlusion site using a catheter without the need for a balloon catheter, as is the case with stainless steel stents. Once released the nitinol stents self-expand due to the removal of strain; this allows a much less invasive surgery. As well, nitinol stents can also provide a support for graft material designed to repair aneurisms. The conventional surgery requires accessing the aorta, inserting the graft and then sewing the aorta closed. This procedure has a high patient recovery time, up to 6 months, and high morbidity. The nitinol graft can be inserted with a catheter

through the femoral artery, requiring no surgery reducing the average recovery period to 11 days [4]. Figure 2.2 shows the stress strain behavior of nitinol, stainless steel, and biological materials. When comparing the stress strain behavior of nitinol and stainless steel to biological materials nitinol emerges as having the most similar properties. This allows nitinol stents to enable the blood vessel to move and expand freely, in contrast to a stainless-steel stent which forces it to remain fixed in one orientation. As well, nitinol bone implants and the bone itself will have similar material properties in terms of their elasticity, these implants are more biocompatible. On the other hand, stainless steel stents suffer from stent migration due to blood vessel movement and systolic and diastolic blood pressures. Nitinol stents are pseudoelastic allowing them to resist these changes in pressure and remain in position [15]. MRI imaging is commonly used to assess the success of a stenting operation. Materials with high magnetic susceptibilities create large field distortions and artifacts obscuring the image. Nitinol is a non-ferrous alloy and therefore has a much lower magnetic susceptibility compared to stainless steel. When imaging nitinol there are fewer distortions which enable doctors to better assess the outcome of the procedure [4]. The benefits described in this paragraph have not been overlooked and have propelled nitinol stents in only a few decades to account for around half of all stents used throughout the world today [16]. But, challenges relating to corrosion and biocompatibility still remain, these will be discussed in section 1.2.3 and 1.2.4.

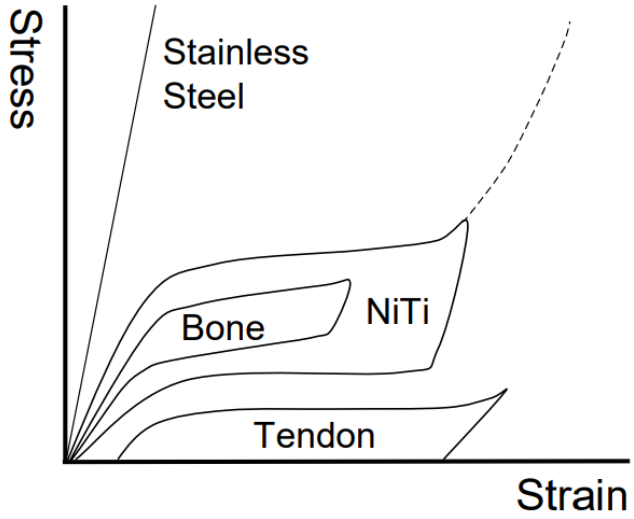

Figure 2.2: The stress-strain relationship for superelastic nitinol stainless steel, bone, and tendon tissue *[4]*.

2.2.3 *In-vivo* Stent Corrosion

Nitinol stents after undergoing surface passivation treatments such as electropolishing and chemical etching have excellent *in-vitro* corrosion resistance but their long term *in-vivo* resistance is less well known. Several studies on early nitinol stents found that pitting corrosion lead to the premature failure of nitinol stents [17, 18]. Every stent explanted by Heintz *et al.* even in as little as 5 months was found to have a multitude corrosion pits on the surface. As expected stents implanted for a longer duration illustrated a more severe degree of pitting corrosion with several covered by large defects and fractures [17]. The authors theorized that the poor corrosion properties of these stents could be due to the adherence of white blood cells and epithelial cells creating an aggressive local environment for the stent [17]. In more recent studies commercial electropolished nitinol stents were observed after explantation to be susceptible to pitting corrosion *in-vivo*. Even mild pitting corrosion could lead to the premature fracture of stents under the cyclic loading experienced by

the implant and the release of metal cations into the surrounding tissue [6, 19]. Corrosion resistance of the explanted stents was thought to be reduced by abrasions resulting from manufacturing and patches of residual original oxide which were not fully removed [6, 19]. Mazanec *et al*. studied five explanted nitinol bone implants for corrosion. No corrosion was observed using SEM observation on the samples, which were implanted in the body between 4 to 12 months [20]. A recent study by Sullivan *et al.* sought to link the *in-vitro* breakdown potential (E_b) with the severity of explanted stent corrosion *in-vivo*. After 6 months implanted in a minipigs artery, the explanted stents with an oxide layer created with high temperature thermal oxidation were found to have undergone severe pitting corrosion [21]. The mechanically polished and electropolished explanted stents exhibited no pitting corrosion after SEM investigation. Their research found that stents with breakdown potentials above 600 mV, relative to the saturated calomel electrode (SCE), would not corrode *in-vivo* [21]. The Ag/AgCl electrode measures a potential 45 mV more noble than the that measured by the SCE electrode. The study by Sullivan *et al.* is contrasted with the previous studies mentioned in which corrosion was commonly found on explanted electropolished stents. This is likely due to differences in the preparation of the stents and the quality of the metal supplied.

2.2.4 Nickel and Biocompatibility

Along with the obvious problem of stent fracture due to corrosion, the release of metal ions into the surrounding tissue also poses a problem, especially concerning nitinol. Nitinol is composed of approximately 50% nickel, which is a known carcinogen and allergen [22]. Shih *et al*. anodically polarized nitinol while being

surrounded by cultured rat smooth muscle cells. Cell growth was inhibited due to nitinol corrosion and the release of nickel into the surrounding tissue. As well, the cells underwent morphological changes and an increase in cell death as the nickel concentration increased, due to corrosion, past 9 ppm [23]. It is very difficult for nickel ions to leave the bulk due to high atomic bonding forces and the protective titanium oxide layer which poses a large impediment to diffusion. Setting aside any corrosion, nitinol implants are usually only responsible for releasing a small amount of nickel. Ries *et al.* investigated the change in the serum nickel concentration. With nitinol amplatzer septal occluders, a nitinol mesh that closes holes on either side of heart cavities, implanted into the body the blood concentration was measured in 67 patients, 24 hrs before and 24 hrs, 1, 3, and 12 months after. The researchers found the mean concentration rose from 0.47 ng/ml to 1.27 ng/ml 24 hours later. This increased to a maximum of 1.50 ng/ml after one month and then slowly decreased back to 0.47 ng/ml after 12 months. The researchers proposed this decrease was due to a calcium-phosphate layer forming after implantation or endophilia cells surrounding the implant stopping nickel diffusion [24]. The surface chemistry and the structure of the oxide greatly affects the rate nickel is released from the material [25]. S.A. Shabalovskaya found that after applying various surface treatments to nitinol, the nickel concentration varied between 0.4% and 27%. The effect of the various surface treatments on adjacent cultured rat splenocytes was found to be drastically different; a high nickel concertation lead to greater amounts of cell death [26]. Thick oxide layers formed at high temperatures, which have a high concentration of nickel oxide, and rougher surfaces have been found to release more nickel ions. In contrast, mechanically polished and electropolished nitinol exhibited much thinner more homogenous titanium oxides. These passivated oxide layers lead to a much lower rate of nickel release [27]. The

surface nickel concentration does not affect the blood nickel concentration over the long-term. But, high surface nickel concentrations been shown to negatively affect the cellular health of neighboring cells.

2.2.5 Nitinol Oxide Layer

When nitinols surface is properly passivated it is known to have a high degree of corrosion resistance and stability in aggressive solutions [28]. This property is due to TiO_2 making up the bulk of the oxide layer to the exclusion of nickel oxides. The Gibbs free energy of formation, ΔG (298 K), for TiO_2, TiO, and NiO oxides is -889.5, -495, and -211.7 kJ mol^{-1} respectively [29]. The free energy of formation is substantially lower for TiO_2 compared to TiO and especially compared to NiO. When oxides are formed at room temperatures we should expect a thin, mainly TiO_2 oxide layer ($\leq$ 10 nm), to form based on the thermodynamics. Treatments at high temperatures, such as those required to set the materials shape (~ 770K), produce a much thicker oxide ($\geq$ 100 nm) with a far greater share of nickel oxides, which reduce the corrosion resistance [28]. As well, titanium oxides exposed to high temperatures will undergo a phase change from the anatase phase to the rutile phase. Hansen *et al.* claims that this phase change increases the density of defects embedded in the surface. This will lead to a reduction in the corrosion resistance [30]. Increasing the temperature of the heat treatments results in thick, porous, and rough oxide layers that easily crack under low strains (<1 %). These cracks open new faces to degrade and are susceptible to crevice corrosion due to differential oxygen concentrations [28]. The rutile and anatase phase of TiO_2 have much larger unit cell volumes, 0.062 nm^3 and 0.136 nm^3 respectively, compared to the austenitic NiTi substrate (0.027 nm^3) [31]. As the oxide

layer grows thicker, due to oxidation, a high level of stress builds up due to this volume difference. This gives rise to a surface that is progressively more cracked surface as the oxide grows. Thick oxides grown at high temperatures also corrode more vigorously when put under strain compounding with their already poor corrosion performance In comparison, the corrosion resistance of thin (≥ 10 nm) air-grown films did not suffer under strains of 6-8%, in the tension mode [28]. Thick, homogenous TiO_2 oxides can be formed by long term exposure to low temperatures (373 K, 1 atm) but this oxidation will create a sublayer below the oxide depleted of titanium [32]. This material may appear to be free of nickel on the surface but any corrosion can unearth the rich Ni sublayer resulting in a high amount of nickel leaching into the body. There are also large differences between different as received oxide layers due to differences in temperature and manufacturing method. Nitinol wires are drawn from an ingot using diamond drawing plates. The resulting material exhibits a gold-brown coloured oxide layer, fine drawn wire. After this step many manufacturers anneal the material at high temperatures further oxidizing the material leaving a black oxide with a poor corrosion resistance [33].

Another factor affecting the corrosion resistance of an oxide layer is the crystallinity of the oxide. Generally amorphous oxide layers are thought to be more corrosion resistant than highly crystalline oxides. Amorphous oxides would lack grain boundaries and other defects associated with crystalline materials that reduce their corrosion resistance. An additional benefit of an amorphous oxide layer is the greater biocompatibility, allowing easier bonding of platelets to the material [34]. Several studies have shown that amorphous oxides are correlated with superior corrosion resistance. Shabalovskaya *et al.* probed the crystal structure of chemically etched nitinol samples boiled in distilled water using electron backscattering diffraction

microscopy. They found that the treatment created an amorphous and homogenous TiO_2 oxide layer. Chemically etched and then heat-treated samples exhibited no crystalline order with an annealing temperature of 500ºC and only started to form a polycrystalline oxide at 700ºC [35]. Oxides formed at high temperatures have a lower resistance to corrosion. McBee and Kruger found that as the Cr content in a stainless-steel oxide was increased the oxide becomes more amorphous, higher chromium content stainless steels are more corrosion resistant [36]. Shih *et al.* set out to directly prove amorphous oxides are superior to polycrystalline oxides. They converted a polycrystalline nitinol oxide layer to an amorphous oxide layer. Shih *et al.* chemically etched nitinol wires and passivated them to form an amorphous oxide. The samples with the amorphous oxides exhibited no breakdowns while those with the polycrystalline oxides corroded at potentials between 0.2 and 0.6 V [37]. Interestingly these corrosion tests were performed in the aortic artery of mongrel dogs. But, no studies were performed outside of the body so the difference in the results between testing in the aorta and testing in a laboratory corrosion cell, especially in terms of blood flow, were not determined. The exact experimental techniques for converting nitinol with a polycrystalline oxide to an amorphous oxide was described in a separate paper published in a non-peer reviewed industrial journal; it cannot be found in academic databases and no pdf exits. The researchers do say that the amorphous samples were created after chemical etching the polycrystalline samples [37]. Chemically etching nitinol samples removes inclusions, defects, and the thick low corrosion resistance oxide. The researchers did not show that the change in oxide layer structure is the cause of this increase in corrosion resistance and not the removal of defects from the surface. In fact, chemical etching is known to increase the corrosion resistance of most materials with a native oxide layer [28, 38]. E. McCafferty in

"Introduction to Corrosion Science" also states that amorphous oxides have a much higher corrosion resistance compared to polycrystalline oxides. But the papers cited to support this investigates the corrosion of amorphous alloys not alloy with amorphous oxides [39]. While the theoretical reasons for the beneficial effect of changing a polycrystalline oxide to an amorphous oxide make physical sense the experimental evidence is severely lacking relative to the strength of the claims.

2.2.6 Water Treatment

When implants are sanitized they are many times autoclaved or sterilized in boiling water. Shabalovskaya *et al.* determined the effect of these sterilization techniques on the biocompatibility of nitinol [40]. The increased temperature was found to have promoted the diffusion of much of the remaining nickel out of the oxide layer. It was found that the elevated temperature led to the growth of the oxide layer from ~4 nm to the 10-20 nm range. The thicker oxide layer had a greatly reduced nickel concentration on the surface (0-1%) and a lowered level of Ni release over time. The corrosion resistance with the thicker oxide was not found to deteriorate under strains of up to 6-8%, in the tension mode [40]. In a later paper, using a scratch test Shabalovskaya *et al.* found that the chemically etched plus water treated samples had a higher pitting potential compared to the as received and chemically etched samples [41]. The independent effects of just the water treatment were not isolated or discussed. In a paper by the same researchers, the ion concentration of the distilled water, used to boil the samples, was tested for its nickel concentration. Using inductively coupled plasma analysis they determined that nickel did diffuse out of the sample when boiled [40]. Michiardi *et al*. followed their thermal treatment with a boiling water bath for 1

hour; they found that Ni release in treated samples virtually ceased 24 hours after immersion [42]. A treatment in boiling water has been used to improve the corrosion properties of other materials. Klages *et al.* applied a similar treatment to stainless steel 316 LVM [43]. The treatment greatly increased the corrosion resistance of the material. The researchers argued that this was caused by the selective dissolution of soluble MnS inclusions on the metal surface. These inclusions are thought to be precursor sites to corrosion in stainless steel. Any effects on the oxide layer thickness or make up was not investigated [43].

2.2.7 Hydrogen Peroxide Treatment

Titanium implants that have been in the body for many years have been found to have thick oxide layers some, on the order of micrometers. Most titanium implants with air grown oxides possess a thickness on the order of nanometers, ~4 nm. H_2O_2 generated in the body due to an inflammatory response to the implant has been proposed as the source of the high rate of *in-vivo* oxidation [44]. In the immediate region surrounding a site of inflammation the hydrogen peroxide concentration can rise to 1.1% [45]. Pan *et al.* showed that when titanium was left in a solution of H_2O_2 a thicker TiO_2 oxide layer formed over several weeks. The titanium oxide layer changed the colour from grey to a light blue due to diffraction effects of the thicker oxide [44]. This also indicates the light-brown as received oxide is thicker than the air grown layer that appears after mechanically polishing. Chu *et al.* oxidized chemically etched nitinol samples by boiling them in a bath of 30% hydrogen peroxide for 2 hours creating a 500 nm thick TiO_2 oxide layer. They found the treatment dramatically reduced the Ni concentration on the sample surface. Chu *et al.* proposed that the mechanism for

oxidation by hydrogen peroxide is different than the one for high temperature oxidation [31]. High temperatures induce the diffusion of Ti metal out of the bulk into the oxide where they are then oxidized. This leaves behind a nickel rich $TiNi_3$ phase just beneath the surface [29, 46]. The mechanism proposed by Chu *et al.* instead suggests that the elevated temperature due to boiling induces Ni atoms to diffuse out of the bulk and the oxide into the surrounding solution. H_2O_2 etching can break the Ni-Ti bond opening sites for oxidation. This leaves behind vacancies which are subsequently oxidized by peroxide radicals [31]. The oxide layer in this case should expand inward with nickel moving towards the surface and oxygen towards the bulk. In contrast, oxidation due to high temperatures leads to an outward growth of the oxide layer and to the formation of the $TiNi_3$ layer, not seen in H_2O_2 treated samples [46]. Chu *et al.* found the Ni concentration decreased from 47.5% to 6.7% when a chemically etched nitinol sample underwent 30% H_2O_2 treatment for 2 hours [31]. This initial surface Ni concentration is uncharacteristically high, it is close to a bulk concentration, for a passivated, chemically etched, sample.

Shabalovskaya *et al.* applied a similar hydrogen peroxide treatment to nitinol. Their samples were first polished to a 1 μm mirror-like finish and then chemically etched with a solution of HF and HNO_3. The researchers used 3% and 30% solution of H_2O_2 and increased the temperature of the solution to 90°C, the treatment was applied for 2 hours. The 3% and 30% H_2O_2 treated samples had oxide layers with a 20 nm and 100 nm thickness respectively. The samples treated with 30% H_2O_2 were found to have a higher current density than those treated with 3% H_2O_2 during potentiostatic tests. The authors attributed this to the higher density of cracks found on the 30% treated samples. The treatment created an oxide layer with a comparable thickness to one grown by a short heat treatment. But, samples that undergo short heat treatments have

a poor corrosion resistance, like those with a native oxide. They proposed this difference was due to the increased homogeneity of the resulting oxide over one created at high temperature. The samples corrosion performance did not deteriorate when strained up to the elastic limit unlike the as received and heat-treated samples. The temperature of this treatment, 90°C, is to far to low to induce atomic diffusion to allow new phases to form, but this elevated temperature was likely able to assist in the diffusion of Ni atoms from the surface of the material. They found the concentration of Ni decreased from 14% to 6% for the 3% treatment and from 14% to 10% for the 30% treatment [45].

2.2.8 Corrosion of Nitinol

Inclusions are known to accelerate corrosion in several ways. Impurities can be preferentially dissolved leaving holes in the oxide that can more easily corrode. As well, inclusions can be more noble in comparison to the surrounding oxide layer which can lead to localized galvanic corrosion. Inclusions are also known to trigger the fatigue failure of nitinol medical devices. Three types of inclusions are found in nitinol: carbides (TiC), intermetallics (Ni_3Ti), and intermetallic oxides ($Ti_2Ni_2O_x$). Bai *et al.* found that $Ti_2Ni_2O_x$ had a potential more noble than the nitinol matrix but they found these inclusions did not cause the breakdown of nitinol [47]. TiC is also suggested to be a cause for pitting corrosion in nitinol [28]. Due to the electro discharge machining process a surface layer, 5 to 22 μm deep, of TiC inclusions is found in as-received nitinol [48]. Electropolishing and chemical etching are known to remove these defective surface layers [28]. Wohlschlögel *et al.* investigated the effects of these inclusions on corrosion. They drew tubes from a variety of nitinol ingots of various

quantities and determined the size distribution of inclusions. They found the size rather than the number of inclusions influenced the corrosion. A sample with larger inclusions would corrode more readily over a sample with a higher concentration of smaller inclusions. Wohlschlögel *et al.* suggested this was due to inclusions acting as crevices where corrosion is initiated [49]. A recent study by B.G. Pound similarly found that the size of the inclusion played a critical role in the onset of pitting corrosion. For electropolished nitinol, Ti_2NiO_x inclusions were found to be associated with pit initiation. Secondary pits initiating around the original site of stable pitting preferentially form around larger inclusions. B.G. Pound proposed that inclusions deplete the nitinol matrix adjacent to the inclusion of titanium. The larger the inclusion the more titanium is depleted therefore and the more susceptible the local area is to corrosion. B.G. Pound found that the type of inclusion plays a secondary role at most in comparison to size [50].

Nitinol is commonly held to have a widely varying corrosion resistance, depending on the surface treatment. This is likely due to differences in the preparation of the oxide which gives rise to different oxide compositions, inclusion distributions, oxide thicknesses, roughness's, and crystallinities [28]. The preparation known to have the poorest corrosion resistance is the as-received state. While this covers a rather broad range of surface conditions it generally refers to a thick oxide layer derived from manufacturing where it was exposed to high temperatures. These potentials are reported versus the SCE electrode. Shabalovskaya *et al*. found the average breakdown potential of nitinol wires increased from 176±258 mV to 1000±72 mV when the as received wires were chemically etched, removing inclusions creating a more homogenous oxide [51, 52]. They also tested fine drawn wires with a light brown oxide and the as received samples with a thicker black oxide. The fine-drawn wires had a

higher degree of corrosion resistance in comparison to the black oxide wires, they had breakdown potentials of 466±58 mV and 176±258 mV respectively [51]. Similarly, Sullivan *et al.* tested the breakdown potentials of commercial stents before and after the stent was mechanically polished and chemically etched; the subsequent average breakdown potentials increased from 143.6±73 mV to 831.7±256 mV [27]. Electropolishing is also known to greatly increase the corrosion resistance of nitinol. B.G. Pound found the breakdown potential of mechanically polished nitinol wires increased from 381±76 mV to 1200 mV after they were electropolished [53]. Eiselstein *et al*. found a similar trend where only 10 out of 57 electropolished wires corroded up to 1.2 V in a potentiodynamic test, the breakdown potential was 407 ± 184 mV [54]. The test conditions for these experiments are summarized in table 2.1. There is clearly a large variation in the breakdown potentials reported in these various studies for different surface treatments and even between nominally the same treatment. These discrepancies will be discussed further in the following paragraphs.

Table 2.1: Assorted studies determining the breakdown potential of nitinol samples. The acronyms are as follows: mechanically polished (MP), as received (AS), chemically etched (CE), fine drawn (FD), electropolished (EP), phosphate buffered saline (PBS), simulated body fluid (SBF), breakdown potential or corrosion potential (Eb), relative to the SCE electrode. The final surface finish is given for the MP samples when applicable. In the surface treatment section samples designated with MP or AS and then CE or EP were either chemically etched or electropolished. The test condition section contains the electrolyte, temperature, and potential sweep rate for the experiment. The surface area refers to the area exposed to the electrolyte.

Sample type	Surface treatment	Test conditions	Surface area (cm^2)	E_b (mv)	Ref
Disc	MP, 1 µm	0.9% NaCl, 37°C, 1 mV/s	.0011	>1200	[47]
Wire	AS	0.9% NaCl, 40°C, .167 mV/s	1.76	176(258)	[51]
Wire	AS, CE	0.9% NaCl, 40°C, .167 mV/s	1.76	1000(72)	[51]
Wire	FD	0.9% NaCl, 40°C, .167 mV/s	1.76	466(58)	[51]
Disc	MP, 1 µm	Hanks, 40°C, 0.0028 mV/s	1.13	520(420)	[55]
Disc	MP, EP	Hanks, 40°C, 0.0028 mV/s	1.13	990(50)	[55]
Stent	MP, 17 µm, CE	PBS, 37°C, 1 mV/s	6.35	831.7(256)	[27]
Stent	AS	PBS, 37°C, 1 mV/s	6.35	143.6(73)	[27]
Wire	MP	0.9% NaCl, 37°C, 1 mV/s	2.30	128(66)	[56]
Wire	EP, 2 of 10 corroded	0.9% NaCl, 37°C, 1 mV/s	2.30	413(37)	[56]
Disc	MP, 1 µm	SBF, 37°C, .167 mV/s	1.78	>1100	[57]
Disc	MP, 600	SBF, 37°C, .167 mV/s	1.78	600	[57]
Disc	EP	SBF, 37°C, .167 mV/s	1.78	>1100	[57]
Wire	MP	PBS, 37°C, .167 mV/s	1.15	306(59)	[54]
Wire	EP, 10 of 57 corroded	PBS, 37°C, .167 mV/s	1.15	407(184)	[54]

Mechanical polishing can be used to remove the oxide layer derived from manufacturing allowing a thin more corrosion resistant passive layer to form. But, different researchers suggest that mechanical polishing leaves nitinol with a highly variable corrosion resistance. A rougher surface will contain deeper valleys which act similarly to crevices, to some degree inhibiting diffusion which allows corrosion to occur at a lower potential. As well, work by Tuissi *et al.* has shown that the size of inclusions decreases as the size of the polishing particle decreases, from 600 grit to diamond suspensions, meaning a flatter surface. As discussed in the beginning of this section nitinol corrosion is strongly dependent on the size of the inclusions [57]. Bai and Rotermund tested discs ground from wires polished up to a mirror-like surface finish, using 1 µm diamond paste. They reported that no corrosion was observed on any of the nitinol samples, on both 500 grit and 1 µm mirror-like samples, past 1200

mV where oxygen evolution starts to account for the rise in the measured current, table 2.1 [47]. On the other hand, B.G. Pound [56] and Thierry *et al.* [55] found that the breakdown potential of mechanically polished nitinol was 128 ± 66 mV and 520 ± 420 mV respectively. Tuissi *et al.* tested the corrosion resistance of nitinol polished to a 600 grit and 1 μm mirror-like finish. They found that the mirror-like samples exhibited no corrosion up to 1100 mV but the 600 grit samples did undergo corrosion at 600 mV [57]. Eiselstein *et al.* performed cyclicvoltammetry experiments on 50 mechanically polished and 57 electropolished nitinol samples. They found that the breakdown potential of MP nitinol was 309 ± 59, 283 ± 18, 246 ± 65, 138 ± 67 mV for a pre-test corrosion electrolyte exposure time of 156, 60, 12, and 1 hours respectively. This is a dramatic difference, considering that most researchers leave their samples in solution for approximately 1 hour prior to testing many studies may be underestimating the breakdown potential.

Clearly there is indeed a large discrepancy in the corrosion resistance of mechanically polished nitinol. Likely a part of this discrepancy is due to different pre-corrosion exposure times. Usually, researchers use an exposure time of 1 hour but sometimes it can be as high as 12 or 24 hours. The corrosion resistance of implant materials is usually tested in one of the three common physiological solutions: Hanks's solution, phosphate buffered saline solution (PBS), and 0.9% NaCl solution. Work by B.G. Pound found that in the case of nitinol corrosion is most aggressive and has the lowest breakdown potential with the 0.9% NaCl electrolyte [53]. Simulated body fluid (SBF) was not tested by B.G. Pound but it has very similar salt concentrations to PBS. The discrepancy in breakdown potentials is not due to the physiological solution used, the solution used is only of secondary importance. The potential sweep rate is said to not significantly affect the corrosion resistance of the material when the rate is equal to

or below 1 mV/s [58]. Bai and Rotermund tested the surface exposed by grinding a wire flat. The surface they tested would not be enriched by inclusions since it is from the bulk of the metal [47]. Tuissi *et al*. and Thierry *et al.* tested samples cut from a sheet of nitinol [55, 57]. Bai and Rotermund's sample would lack an enriched TiC sub-surface layer due to manufacturing, unlike those from the other two papers. This is a possible explanation of the difference in the corrosion performance between Bai and Rotermund's 1 μm samples and those tested by Thierry *et al.* and Tuissi *et al.* As well, Thierry *et al.* and Tuissi *et al.* tested a sample with a much larger surface area compared to Bai and Rotermund [55, 57]. A larger surface area would encompass more inclusions and defects where localized corrosion can initiate. Depending on the surface concentration of defects critical for corrosion this substantially smaller area may not contain inclusions large enough to initiate corrosion. As discussed in the previous four paragraphs nitinol has a widely varying corrosion resistance depending mainly on the oxide layer structure as well as the concentration of inclusions, the size of inclusion, and the surface area of the sample.

2.2.9 Spatial Interactions among Corrosion Pits

Pitting was long assumed to occur randomly in both time and space but several studies have shown that pit propagation is heavily influenced by neighboring corrosion pits. When a pit is corroding metal cations and hydrogen ions will diffuse out of the pit. Change in the local environment around the pit can be detected upwards of three pit diameters away [59]. The surrounding oxide layer is thinned by a decrease in pH driven by nearby pitting. This increases the probability that pits will form close to the pits which have reached already stability. Wu *et al.* created a stochastic model to

describe the transition from metastable to stable pitting corrosion. They also found that experimental evidence can only be accurately modeled when interactions between neighboring metastable pits were taken into consideration [60]. Current spikes due to individual metastable pitting events were found to be correlated in time. This gives further evidence that pits interact with each other during propagation [61]. The small number of metastable pits that nucleate will enable further nucleation of more pits close by, building up to a transition to stable pitting leading to even more metastable pits nucleating around those pits.

The studies discussed above were performed by analyzing the current time plots on Al and SS samples under potentiostatic conditions. Lunt *et al.* instead created a 5 X 5 array of SS electrodes, with a 0.09 mm spacing between electrodes, to gain more direct evidence of this phenomenon. This allowed them to inhibit or induce stable pitting on each electrode and then investigate the effect corroding electrodes had on their neighbors. They found that the electrodes to closest to an electrode polarized at the breakdown potential were more likely to corrode [62]. These same researchers proposed a stochastic model that included the effects of local concentration, alterations in the potential field, and damage to the adjacent oxide layer [59]. Punckt *et al.* imaged the corrosion of a SS 316 disc using both light microscopy and a novel technique known as ellipsomicroscopy for surface imaging, which indicates the relative thickness of the oxide layer, to capture videos of corrosion in real time. Using these techniques, the authors could correlate current spikes with pitting events seen in the video [63, 64]. Their work reinforced Lunt *et al.*, suggesting that pitting is not random in time and space and that stable pits induce corrosion around themselves. They found this phenomenon occurring on a sample piece of SS 316, in potentiostatic conditions, instead of on an array of electrodes [63, 64].

Another form of corrosion that is known to exhibit spatial interactions is the corrosion of magnesium. Magnesium corrosion has been found to propagate via multiple different mechanisms depending on the chloride concentration. At low concentrations dark thread-like tracks, filiform like, have been visualized crossing the surface. At higher concentrations a single corrosion front has been observed. Williams *et al.* investigated the root of this mechanism change using in-situ imaging and varying concentrations of NaCl. They proposed that the changing corrosion mechanism is due to the decreased conductivity of the electrolyte, as the concentration of NaCl is decreased. A lower conductivity limits the distance over which galvanic coupling can occur. The shortest possible distance between possible galvanic couples is a line perpendicular to the anodic region. This inhibits the radial propagation of corrosion, the front. In the high concentration case longer galvanic coupling distances that are not perpendicular to the corrosion front are possible [65]. One key difference between the corrosion of nitinol and Mg is the continuously moving anodic region. Regions of Mg that have corroded become cathodic relative to a small anodic region that is continuously moving; virgin Mg does not take part in the reaction until the anodic region moves in [66]. In contrast the non-corroded regions of nitinol act as the cathode not the previously anodic regions. A study by Chu *et al.* looked at the differences between the corrosion mechanisms of Mg, Mg-Zn-Ca-Mn, and Mg-Y alloys. They imaged the surface of each alloy under immersion, with no potential applied. They found the same results as Williams *et al.* for pure Mg but they found Mg-Zn-Ca-Mn alloys corrode via filiform corrosion independent of the NaCl concentration. Corrosion in Mg-Y alloys was found to follow the alloy grain structure as they propagated throughout the sample [67].

2.2.10 Outlook

Both the hydrogen peroxide and water treatments have been shown to improve the corrosion resistance of chemically etched nitinol wires. But, the chemically etched nitinol control wires already both have very high breakdown potentials [35, 45]. The difference in the corrosion resistance between the chemically etched and treated samples was not great. Both the hydrogen peroxide and the water treatment were applied, separately, in this thesis to mechanically polished and as received nitinol wires. We will characterize the corrosion resistance before and after these treatments and determine if they are still effective. The corrosion resistance will be characterized using cyclic voltammetry scans, to find the breakdown potential, and by characterizing mass loss behavior of each of the various treated samples. Furthermore, we will compare the relative effects on the corrosion resistances of both the water and hydrogen peroxide treatments to determine which is superior. In the study by Shabalovskaya *et al.* the water treatment was found to produce a more amorphous oxide, which are thought to be more corrosion resistant, in comparison to the air grown oxide [35]. We will determine the crystallinity of the mechanically polished, water, and hydrogen peroxide treated oxide layers. This may provide insight as to how the hydrogen peroxide treatment increases the corrosion resistance. We will also investigate the surface composition and structure of the oxide layer using XPS and SEM to determine what factors are most important for predicting and improving the corrosion resistance of nitinol. The surface of nitinol has yet to be imaged *in situ* when it is undergoing corrosion. We will image the surface of a nitinol disc while it is undergoing linear polarization. This should provide novel information about the corrosion mechanism in nitinol and possible spatial interactions between neighboring regions of corrosion.

2.3 Materials and Methods

2.3.1 Sample Preparation

A variety of sample shapes, such as wires, discs, and plates were used in this thesis. To enable the use of grazing incidence x-ray diffraction (GIXRD) on superelastic nitinol plate samples, 1cm^2, (Kellogg's Research Labs) were prepared. Using a Crystalbond adhesive the samples were mounted onto aluminum pucks prior to polishing. Prior to grinding, nitinol wires had Teflon heat shrink tubing, with their interior filled with epoxy, and then had rubber heat shrink tubing shrunk onto the Teflon, the epoxy hardened around the wire after heating. This tubing allowed a tight seal with the wire and was intended to reduce crevice corrosion. The samples were first wet ground with 1500 grit abrasive paper (Buelher) to remove the as received oxide layer. The samples were then polished respectively with 9, 3 and finally a 1 μm diamond suspensions (Buelher) at 100 rpm (Buelher Beta Polisher). Before moving to the next step, the samples were washed with ethanol and distilled water. Disc samples, 0.38 mm in diameter, were produced by wet grinding superelastic nitinol wires (Component Supply Co Inc.) flat with 600 grit abrasive paper. The samples were then polished with 9, 3, and 1 μm diamond suspensions, with washing between steps, until they appeared to be mirror like under a microscope.

Prior to the water treatment (WT) some of the wires were polished with 600 grit abrasive paper (Buehler). The wires were then placed in a Teflon container and 90°C preheated distilled water was added. The Teflon container was then inserted into a Thermo Haake C3 heat controlled bath, set at 90°C. The water inside the Teflon container was replaced two times, the samples were treated for a total time of three

hours. In case any ions leeched from the sample into the solution, the water was changed to allow the continued dissolution of potential impurities or nickel on the surface. The hydrogen peroxide (H_2O_2) treatment similarly involved pre-heating a solution of 3% H_2O_2 (ACP and Sigma-Aldrich 30% H_2O_2 ACS reagent) to 90°C. Some H_2O_2 would inevitably evaporate when the wires were pre-heated. To standardize the amount of H_2O_2 left after when the wires were immersed great care must be taken. The temperature of the hot plate and the temperature of the solution must be controlled precisely or the amount of H_2O_2 will vary with each trial. The pre-heated solution was then added to the wire containing Teflon container and placed in the heat bath, set at 90°C. The samples were removed 2.5 hours later. After the treatment, for potentiodynamic tests, the wires were coated with lacquer so only a section of the wire with a 1 cm long length was exposed to the electrolyte. The cut end of the wire was coated as well to restrict corrosion to the uniform wire surface. The wires remained uncoated for the mass loss and XPS experiments. Finally, the samples were sonicated in ethanol and dried with a heat gun prior to testing. The same treatments were also applied to the superelastic nitinol plate samples but unlike the wires they were only treated after mechanical polishing.

2.3.2 Mass Loss Tests

The corrosion performance of alloys in an aggressive $FeCl_3$ solution has been correlated to their resistance to corrosion in common environments such as in seawater or in the body. Samples which experience corrosion of a higher degree of severity are correlated with a higher breakdown potential in potentiodynamic experiments [68]. Superelastic nitinol wires 0.38 mm in diameter (Component Supply Co Inc.) where cut

to 5 cm long. The wires had a golden-brown native oxide layer, this means they were not annealed after fine drawing. The wires were sonicated in acetone, ethanol, and then dried with a heat gun prior to immersion. The samples were placed in a test tube that was also sonicated in acetone, ethanol and then dried with a heat gun. To prevent corrosion at the cut end of the wire 0.5 ml of chloroform was placed into the bottom of the test tube. Chloroform does not mix with aqueous solutions and is inert. Due to the corrosion resistance of nitinol a solution of 0.028 M (4.5%) $FeCl_3$ (Sigma-Aldrich Iron(III)Chloride 97% ACS reagent) was used to accelerate the onset of corrosion. Corrosion tests with 4.5% NaCl (ACP NaCl 99% ACS reagent) were also attempted but no measurable change in mass occurred within a month and the experiment was discontinued. Samples were sonicated in acetone and then ethanol before weighing to dislodge any debris that may be stuck on the surface. After sonication the samples were dried with the heat gun and weighed. Samples, removed from the solution, were not returned to the solution after weighing. Wires with an as-received oxide, as-received oxide water treated, as received hydrogen peroxide treated, 600 grit samples, and 600 grit water treated samples were tested; the treatments will be summarized in a following paragraph. For each day immersed, a minimum of three samples were removed from the test tubes and weighed using a Sartorius Research R160P scale, accurate up to ten micrograms.

2.3.3 Nitinol Wire Potentiodynamic Tests

Five different surface finishes were tested in this experiment: as received, as received with water treatment, 600 grit, 600 grit with water treatment, and as received with hydrogen peroxide treatment. Two electrolytes were used in this experiment, a

.154 M NaCl, 0.9%, solution (ACP 99% NaCl, ACS reagent), and a solution of HCl (Sigma-Aldrich 37% HCl, ACS reagent) and NaCl. The acidic solution was composed of .054 M HCl and .1 M of NaCl to keep the chlorine ion concentration constant. The addition of HCl greatly lowers the pH from approximately 7 to 1.27. Samples were tested in a 5 ml glass cuvette. Prior to an experiment the cuvette was sonicated in ethanol, rinsed with distilled water, and then ringed with the test electrolyte.

A standard three electrode cell was used in this experiment. A 2 cm long platinum wire was used as the counter electrode. A micro silver silver-chloride (Ag/AgCl) electrode (eDAQ, model ET073) was used as the reference. A saturated KCl solution filling solution, which was replenished regularly, was used giving the potential .197 V at 25 °C versus the standard hydrogen electrode (SHE). The potential of the Ag/AgCl electrode was periodically compared to a reference SHE electrode to make sure no potential drift was occurring. All potentials were reported against the Ag/AgCl electrode unless stated otherwise. The nitinol wire samples were used as the working electrode. The measurement was performed by an Autolab PGSTAT 2014 potentiostat. Prior to the potentiodynamic experiment the open circuit potential was measured for 30 minutes to determine the potential was stabilized before the experiment was initiated. The potential was started 100 mV below the open circuit potential (E_{ocp}). The potential was increased at a rate of 1 mV/s until the current threshold was reached or the applied potential reached 1.5 V, above this value water splitting dominates the measured current. The current threshold was set at 50 mA, above this the scan direction would reverse. The experiment would end when the potential reached its starting value.

2.3.4 X-Ray Photoelectron Spectroscopy

A Kratos Axis Ultra X-ray photoelectron spectrometer, using a Al-Kα source with a 15 mA current generated by 15 kV electrons, was used to perform XPS. The CASA XPS software was used to fit the XPS spectra with theoretical peaks. The XPS spectra were taken in a 600 μm lens mode with a 30 eV potential energy. To get the correct peak area for each chemical species a corrected sensitivity factor must be used, this requires the transmission function that is unique to the specific XPS instrument. The transmission function is given by:

$$T = b(PE10^{y}) \tag{4}$$

where PE is the potential energy, KE is the kinetic energy, $x = log\left(\frac{KE}{PE}\right)$, and b is 0.01. The exponent y is given by the formula:

$$y = a_0 + a_1 x + a_2 x^2 + a_3 x^3 \tag{5}$$

where a_0 =1.1066, a_1 = 5.0677, a_2 = -4.0724, and a_3 = 0.9033. Using the transmission function, you find the new sensitivity factor using the relationship:

$$SF_{Corr} = (KE)(SF)(T) \tag{6}$$

where SF is the sensitivity factor for the specific atomic peak. Dividing the peak area by this new sensitivity factor gives the corrected peak area. The survey scan was taken from 0 to 1200 eV along with four high resolution scans. The four regions scanned from 276-296 eV, 445-475 eV, 512-542 eV, and 835-885 eV correspond to the C1s, Ti2p, O1s, and Ni2p peaks respectively. The binding energy was calibrated to the C-C C1s peak, it has a binding energy of 284.8 eV. The surface composition was investigated for samples polished with 1 μm diamond suspension and samples similarly polished and then treated either with hydrogen peroxide or distilled water. Three plate

samples of each finish were tested. As well, XPS spectra from nitinol wires with G600, G600+WT, AS, AS+WT, and AS+H_2O_2 surface finishes were also taken.

2.3.5 Grazing Incidence X-Ray Diffraction

Amorphous oxides are thought to have a higher corrosion resistance in comparison to polycrystalline oxides. As well, amorphous oxides have superior biocompatibility properties, as described in section 1.2.7. Crystalline materials have well defined diffraction peaks while amorphous materials produce broad peaks with very large full width at half max values. GIXRD allows the diffraction pattern from a thin film to be characterized. GIXRD uses a small angle of incidence to penetrate less of the materials substrate. The small angle information depth can be estimated using the following equation:

$$\tau = \frac{\sin\alpha \sin(2\theta - \alpha)}{\mu(\sin\alpha + \sin(2\theta - \alpha))} \tag{7}$$

where μ is the linear absorption coefficient (μ = .0528 μm^{-1} for TiO_2, Cu-Kα radiation), α is the grazing angle, and Θ is the angle of reflection [69]. The information depth is different depths for X-rays diffracted at different angles. For instance, the minimum information depth for an incidence angle of 1º is 314 nm with the detector angle at 10º, the lowest angle in our experiment. This value increases as the detection angle increases until it reaches a plateau at 90º with a value of 325 nm. Assuming an oxide thickness of 10 nm and solving for the incidence angle required to eliminate signals from the substrate, with the detector at 90º we get an angle of 0.03º. This angle is clearly to low to be experimentally feasible, at least with our hardware. It is useful to use an angle below the critical angle for total internal reflection. Due to total internal reflection the

signal will come almost entirely from the thin film, not the substrate. The x-ray beam penetrates only a few nm into the material due to an evanescent wave that forms on the surface. This could allow us to avoid the problem of several hundred nanometer penetration depths which leads to the substrate signal to dominate [69].

A Siemens D5000 XRD was used in this experiment. The samples were mounted using double sided tape into the center of the powder diffraction holder. Three metal pieces, unpolished samples, were placed where pegs that lock the holder in place are located. This lowers the holder to the same level as a normal powder sample. We used a 0.2º divergence slit, 1.0º anti scatter slit, 0.6 mm fixed slit, and the potential difference and current were set at 40 kV and 30 mA respectively. The detector was swept from 10º to 90º. In total 9 nitinol plates (1x1 cm) were tested: 3 1 μm mechanically polished (MP), 3 mechanically polished and water treated (MP+WT), and 3 mechanically polished and hydrogen peroxide treated (MP+H_2O_2) samples. These were the same nine samples that underwent XPS analysis. GIXRD spectra were obtained using a 1.5º incidence angle; a small number of scans were also performed at 10º and 1°.

2.3.6 *In-situ* Optical Experiment

Using an optical set-up corrosion can be investigated *in situ* during a potentiodynamic sweep. This allowed the visual detection of corrosion and the correlation of the electrochemical data with the state of the sample surface. The optical set up is shown in figure 2.3. A green LED is used to illuminate the sample surface, back left of the image. The colour green was used to reduce optical cross-talk with a red, 632.8 nm, HeNe laser in the perpendicular track. The LED and the CCD camera

(Sony XC-ST50, 768x494, 25 fps) are in two separate paths that are combined by a beam splitter. The light from the LED is focused by the objective lens onto the polished sample surface. The CCD records the image at 25 fps. The brightness and contrast can be adjusted using the monitor. The system has lateral resolution of approximately 2 µm [70]. Ellipsomicroscopy for surface imaging (EMSI) can be used to detect local changes in the oxide layer thickness around corrosion pits. Even though our experimental set up allows simultaneous imaging with EMSI and the light microscope, EMSI cannot be used. This is due to the production of hydrogen bubbles which occur when either Nitinol or Aluminum corrode which severely distorts the resulting images; these appear immediately after the initiation of corrosion.

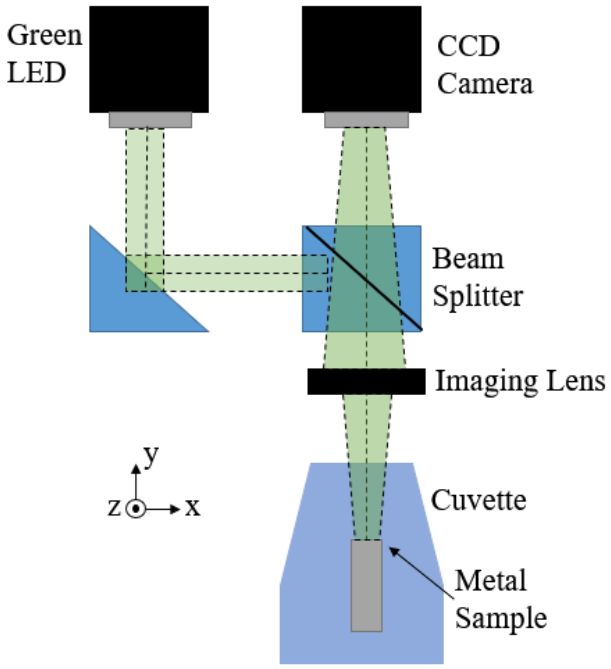

Figure 2.3: A schematic of the optical microscope set up.

The preparation of the nitinol disc samples was described in section 1.3.2. The wires were originally hydrogen peroxide treated to prevent crevice corrosion. But, no corrosion was found on these, before water splitting, so the as received finish was used instead. These samples were tested in an aggressive solution of 1.2 M HCl to initiate corrosion. The same three-electrode cell was used to test the corrosion properties of the discs as the nitinol wires. A miniature Ag/AgCl electrode and 2 cm long platinum electrode was used in this experiment for the reference and counter electrodes, the same potentiostat was used. The open circuit potential was measured for 30 minutes prior to the experiment to reduce noise in the cyclic voltammetry plot. The experiment started 100 mV below the open circuit potential, E_{corr}. The potential was increased at a rate of 1 mV/s. The potential was not reversed at a final potential of 1.5 V; instead the experiment was stopped before the sample was destroyed to allow an SEM investigation after the experiment.

2.4 Results

2.4.1 X-Ray Photoelectron Spectroscopy

In table 2.2 and shown in figure 2.4, the summary of the XPS data is shown for the investigation into the surface composition of nitinol plates. XPS was performed on three samples for each sample type. Four elements were found consistently on each surface: titanium, nickel, carbon, and oxygen. Trace amounts of sodium and nitrogen were found but their percentage was small enough for those peaks to be disregarded (>1%). A Shirley background function was used to model the background signal that arises due to inelastic scattering. This function assumes the inelastically scattered electrons lose a random amount of energy. It does not overestimate the peak signal like

the linear background. There was no significant difference, unpaired t-test with a 95% confidence interval, in the oxygen and carbon concentrations in the three sample types. There was also no significant difference between the titanium concentration in the MP and the MP+WT samples, this was likely due to one anomalous MP+WT sample. On other hand, the MP+WT samples had a lower concentration of Ni compare to the MP samples that bordered very closely on significance. There was a marked decrease in the amount of titanium and an increase in the amount of nickel in the MP+H_2O_2 samples. There was a significant increase in the nickel and a decrease in the titanium concentration when comparing the MP and MP+WT samples to the MP+ H_2O_2 samples. Summarizing, the MP and MP+WT samples had no statistical difference in the Ti concentration, but one did marginally exist for Ni. There was a marked increase of Ni and a decrease of Ti in the MP+ H_2O_2 samples.

Table 2.2: Shown below is the average atomic percent composition of the three different sample types: mechanically polished (MP), MP and then water treated (MP+WT), and MP and then hydrogen peroxide treatment (MP+H_2O_2). Three of each sample type were tested. The individual atomic peaks are broken down into the percentage of each chemical species found on the material. The Ti/Ni ratio is also given. The standard deviation is included for each average in brackets.

Peak	MP	MP+WT	MP+H_2O_2
O1s	43 (1)	47 (4)	46 (3)
C1s	41 (0)	37(7)	41 (4)
Ni2p	3 (1)	1 (.7)	7 (1)
Ti2p	13 (0)	15 (3)	6 (1)
Ti/Ni	5 (1)	14 (7)	1 (0)
C1s			
C-C	71 (2)	61 (8)	74 (1)
C-OH, C-O	14 (1)	20 (4)	9 (1)
C=O	7 (1)	8(5)	2 (1)
O-C=O	8 (1)	11 (1)	15 (3)
Ni2p			
Ni Metal	91 (2)	79 (11)	7 (1)
NiO	9.1 (2)	21 (11)	46 (9)
$Ni(OH)_2$	0 (0)	0 (0)	47 (10)
O1s			
Metal Oxide	62 (4)	71 (10)	46 (4)
Ti_2O_3	23 (0)	18 (4)	41 (4)
OH, C-O	11 (1)	7 (5)	8 (1)
C=O	5 (3)	4 (3)	4 (1)
Ti2p			
Ti Metal	12 (1)	8 (1)	0 (0)
TiO_2	76 (2)	84 (1)	64 (4)
Ti_2O_3	9 (1)	6 (0)	33 (2)
TiO	3 (1)	2 (0)	3 (2)

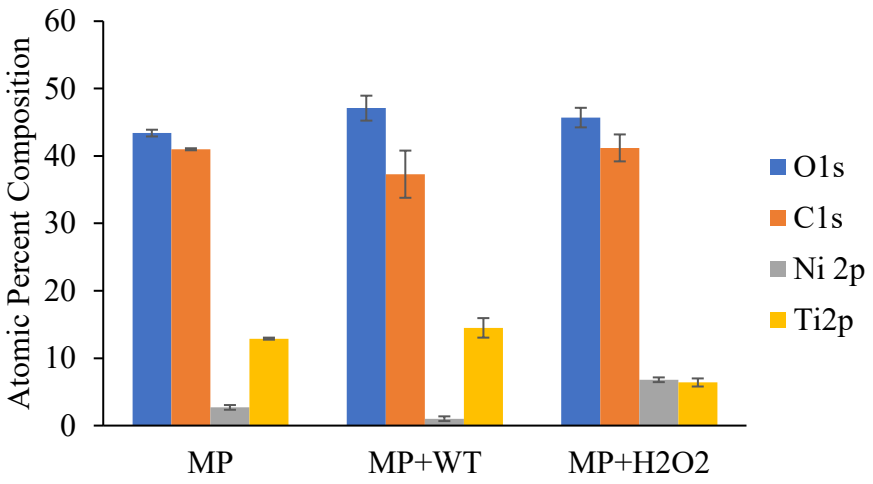

Figure 2.4: The summary of the survey scan data, shown in table 2.2, for the average percent composition of the O1s, C1s, Ni2p, and the Ti2p XPS peaks.

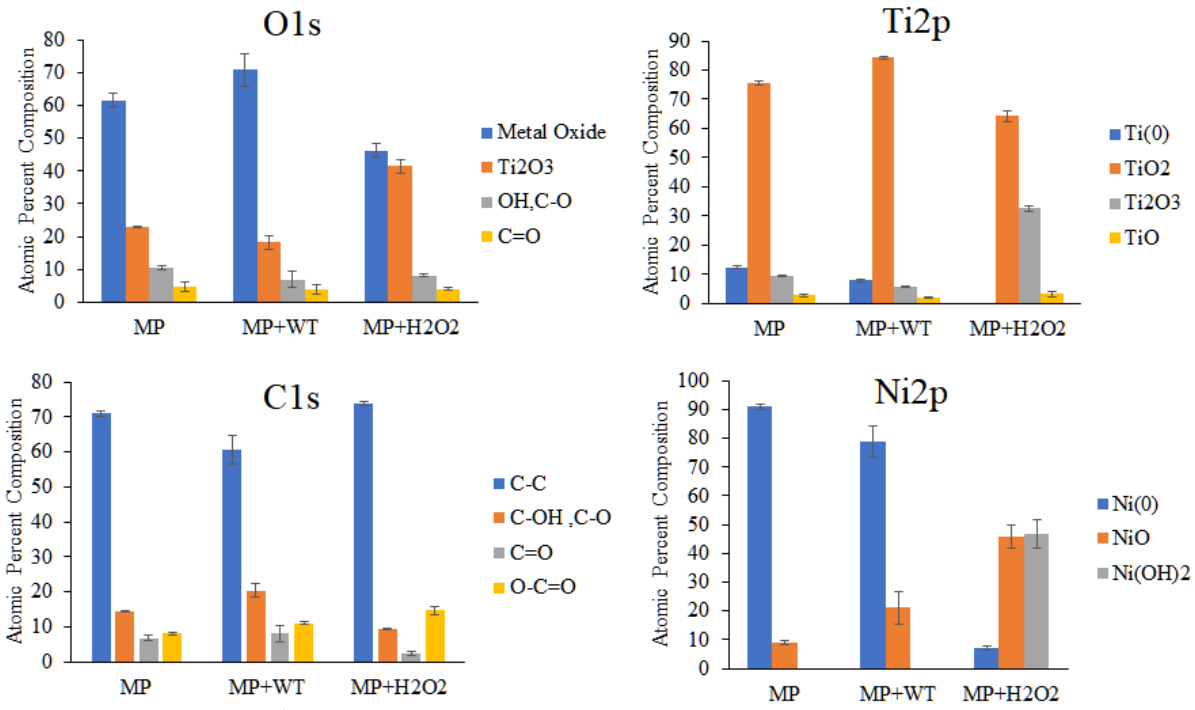

Figure 2.5: A breakdown of the average percent, shown in table 2.2, composition from the O1s, C1s, Ni2p, and Ti2p peaks.

Looking at the breakdown of each specific peak we find that there were changes in the species observed between the samples, shown in table 2.2 and figure 2.5. A typical high resolution XPS spectra for a MP+WT and MP+H_2O_2 sample is show in

figures 2.6 and 2.7. To model the MP spectra the same fit was used as the MP+WT samples, only the MP+WT spectra are shown. The largest difference between different types of samples were found in the nickel 2p, oxygen 1s, and titanium 2p peaks. In the nickel spectra, for MP and MP+WT samples two major peaks were found for Ni 2p, Ni(0) and NiO. These peaks were located at 851.7 and at 853.7 eV respectively, an example is shown in figure 2.6. A special peak shape, a Lorentzian asymmetric lineshape LA(1.1, 2.2, 10), was used for the Ni(0) metal peak to model the asymmetry [71]. Asymmetry arises specifically in metallic XPS peaks due to the availability of conduction electrons for shake-up like events after photoemission of core electrons. This phenomenon manifests itself as a higher intensity tail on the side of greater binding energy. Satellite peaks are common in nickel 2p peaks; the satellite peak is located 3.65 eV above the Ni(0) peak [71]. In the MP and MP+WT samples nickel appears mainly as Ni(0), nickel metal, with a smaller concentration of nickel oxide, NiO, composing the remnants. There is an increase in the amount of NiO when the WT was applied to the MP samples. In the MP+ H_2O_2 samples the amount of Ni(0), shown in figure 2.7, decreased dramatically while the NiO and a new $Ni(OH)_2$ peak dominated. The first Ni(0), NiO, and $Ni(OH)_2$ peaks were located at 852.0, 853.9, and 854.8 eV respectively. Due to large peak widths, to model the Ni2p spectra multiple satellite peaks for each of the three species were required. The constraints on the full width at half max, peak separations, and relative areas for the various satellite peaks were taken from a paper by Biesinger *et al*. who modelled the peak shapes of various nickel species [72].

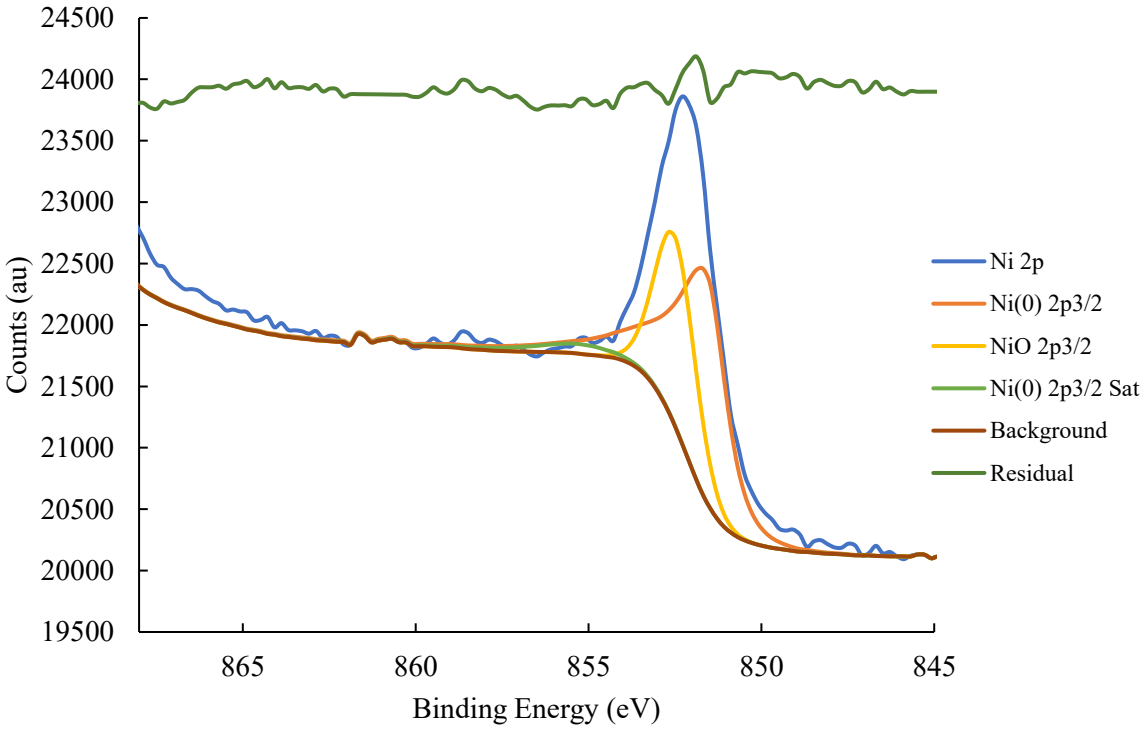

Figure 2.6: High resolution XPS spectra of the Nickel $2p_{3/2}$ peak for MP+WT sample 3.

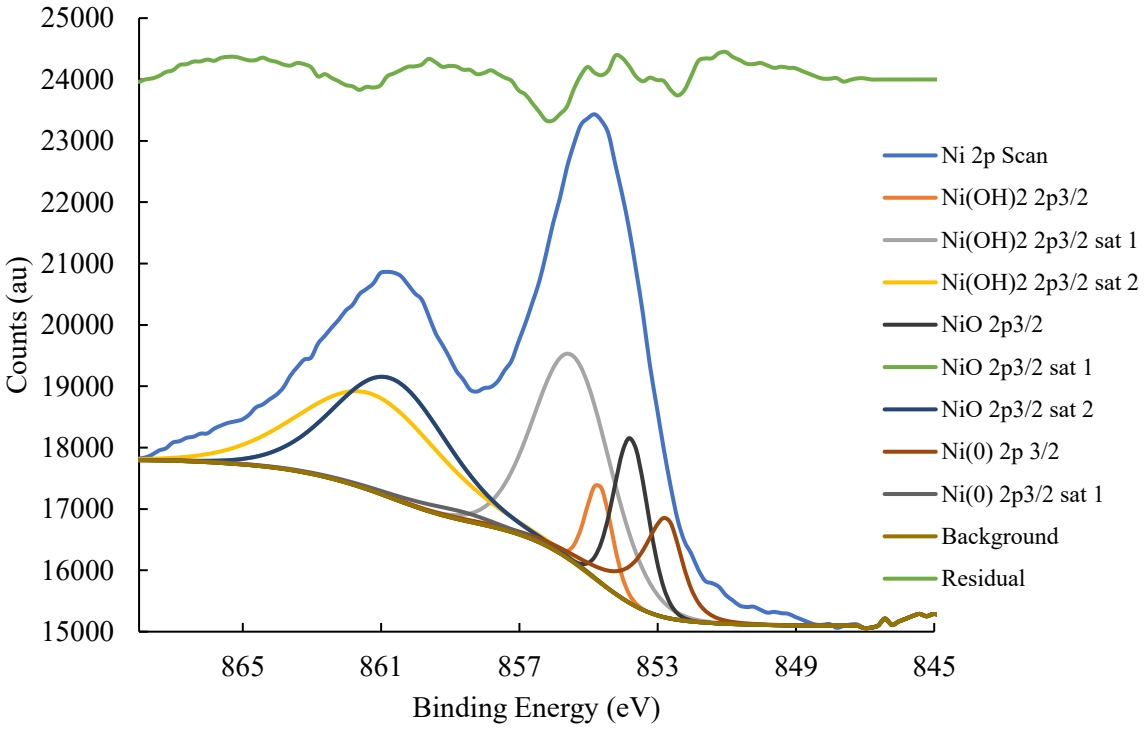

Figure 2.7: High resolution XPS spectra of the Nickel $2p_{3/2}$ peak for MP+H_2O_2 sample 3.

In the MP samples the titanium peak is dominated by TiO_2 oxide but there was also a clear Ti(0) metal peak. Ti_2O_3 oxide was also found as well as a trace amount of TiO. The samples that underwent WT had a significant increase in their TiO_2 concentration. The titanium spectra of the MP+ H_2O_2 and MP+WT samples are shown in figures 2.8 and 2.9 respectively. An asymmetrical peak shape, LA(1.1,5,7), is used to model the titanium metal peak [73]. The MP+WT samples had their TiO_2, Ti_2O_3, TiO, and Ti(0) 2p3/2 peaks located at an average binding energy of 458.5, 456.7, 455.1, and 453.7 eV respectively. The surface of the MP+WT samples had much lower concentrations of Ti_2O_3, TiO, and Ti(0) in comparison to the MP samples. The MP+H_2O_2 samples was found to have no Ti(0) component, only oxide was found. For the MP+H_2O_2 samples the average binding energy of the TiO_2, Ti_2O_3, and TiO 2p3/2 peaks was 458.5, 457.7, and 455.3 eV. The relative compositions of the various oxides also differed significantly. The percentage of TiO_2 decreased while the percentage of Ti_2O_3 greatly increased. This change in the oxide layer composition was also found in the O1s peak where the amount of Ti_2O_3 also saw a large and expected increase. The amount of TiO remained constant between all three samples groups.

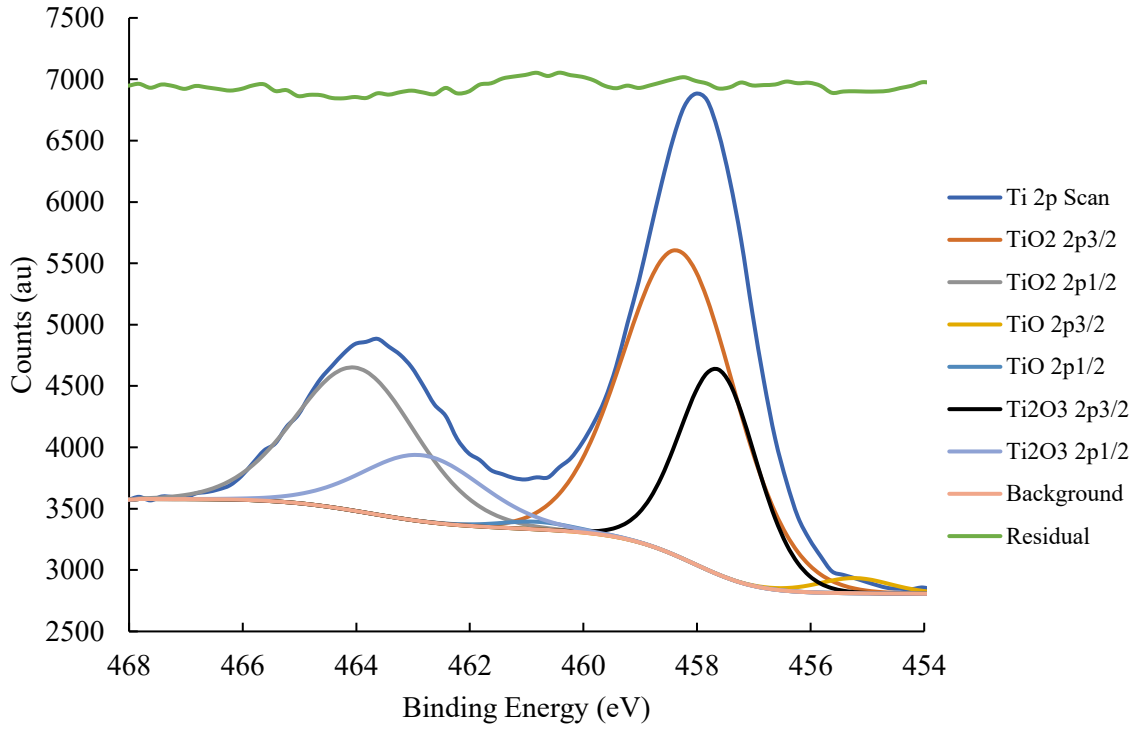

Figure 2.8: High resolution XPS spectra of the Titanium 2p peak for MP+H_2O_2 sample 3.

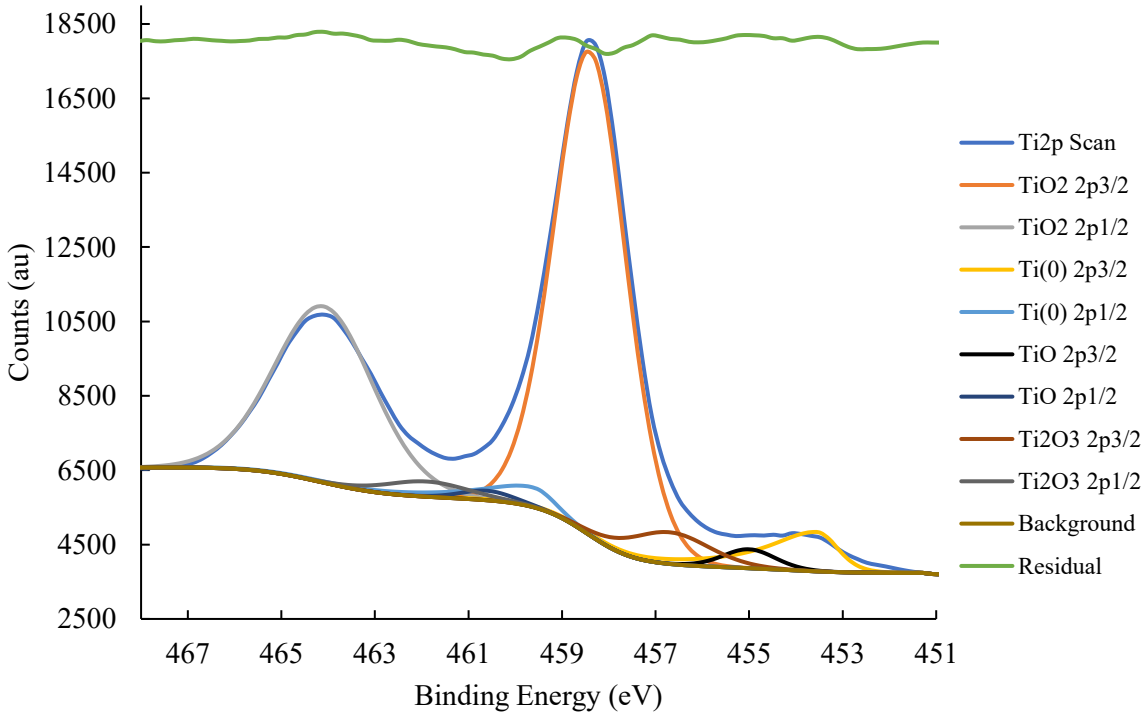

Figure 2.9: High resolution XPS spectra of the Titanium 2p peak of MP+WT sample 3.

The carbon 1s and the oxygen 1s peaks did not substantially change between the two samples groups other than the increase in Ti_2O_3. The oxygen spectra for a MP+WT and for a MP+ H_2O_2 samples are shown in figures 2.10 and 2.11. The metal oxide peaks, Ti_2O_3, C=O, and the C-O peak were located at an average binding energy of 529.9, 531.4, 533.2, and 532 eV for the MP+WT sample. For the MP+ H_2O_2 samples the average binding energy of the peaks was 529.4, 531, 532.8, and 532 eV respectively. Interestingly, no peak was found in the TiC region of the carbon 1s peak. The spectra for the carbon 1s peaks is shown in figures 2.12 and 2.13 for the MP+WT and MP+H_2O_2 samples. Similarly, no intermetallic oxide ($Ti_2Ni_2O_x$) peaks were found but these do overlap with larger peaks, which could explain their absence. As well, these inclusions could be set deeper into the oxide rather than on the surface. The C-C, C-OH, C=O, and O-C=O average peak binding energy was located at 284.8, 286.3, 287.8, and 288.8 eV for both the MP+WT and MP+ H_2O_2 samples. No peaks associated with inclusions were found on the WT, H_2O_2, and the mechanically polished samples, but as was said above due to a small concentration and overlap we likely cannot resolve these peaks. The remaining gas molecules in a high vacuum chamber are usually composed of H_2O and CO. Incident x-rays break down these molecules, leading to the formation of organic molecules when these ions bond together. This gives rise to the adventitious carbon and the associated oxygen detected on a sample. The amount of adventitious carbon found in the XPS spectra is proportional to the length of time the x-rays are incident upon the sample.

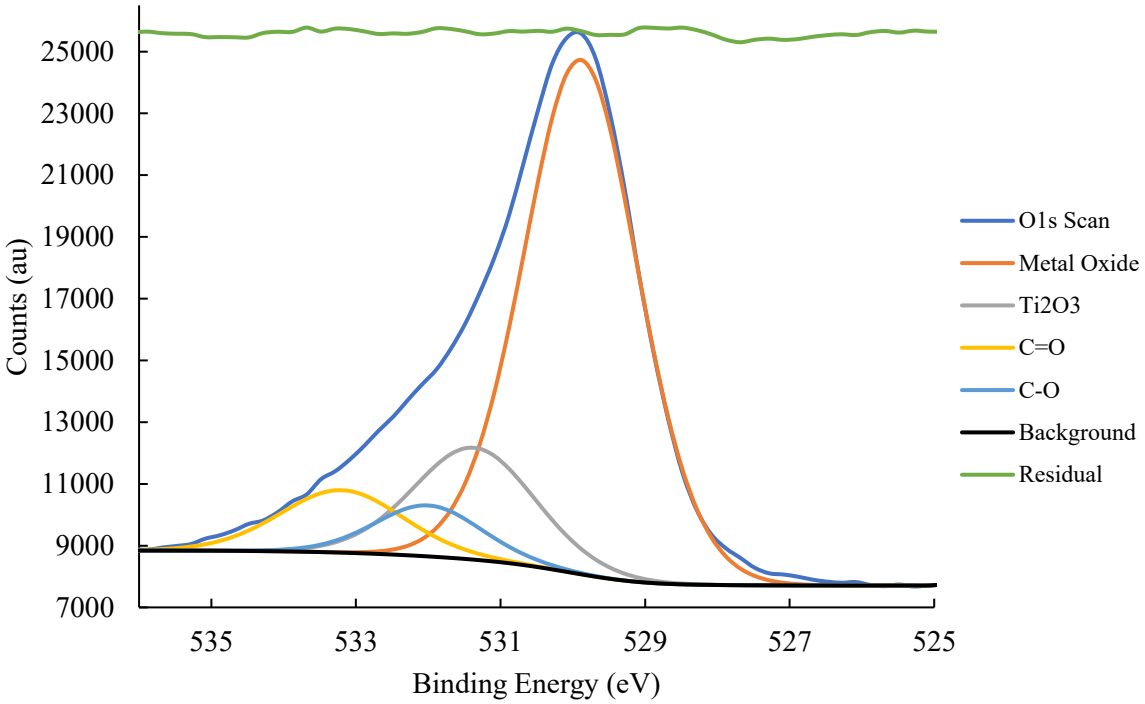

Figure 2.10: High resolution XPS spectra of the oxygen 1s peak for MP+WT sample 3.

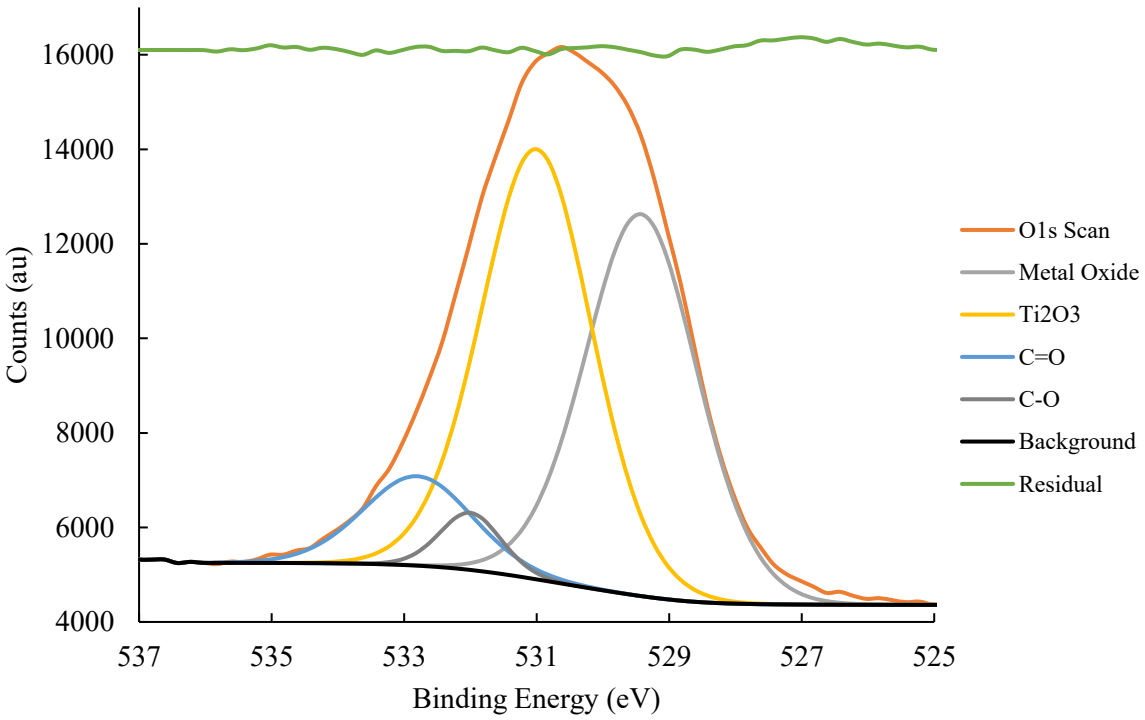

Figure 2.11 High resolution XPS spectra of the oxygen 1s peak for MP+H_2O_2 sample 3.

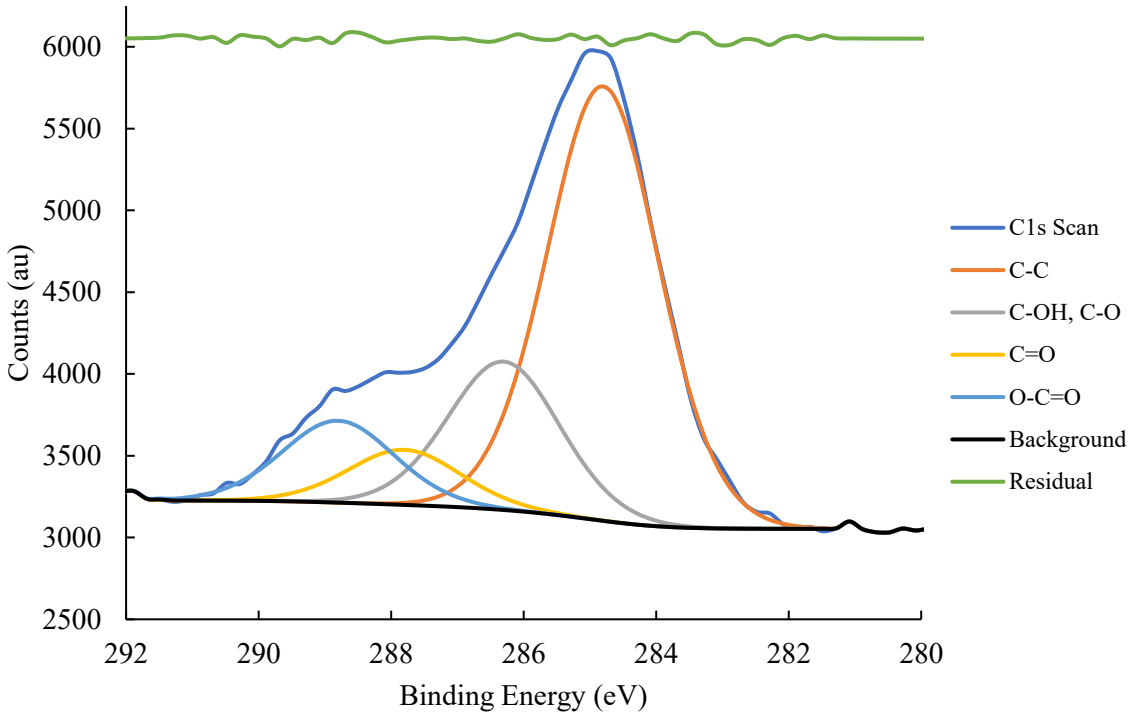

Figure 2.12: High resolution XPS spectra of the carbon 1s peak for MP+WT sample 3.

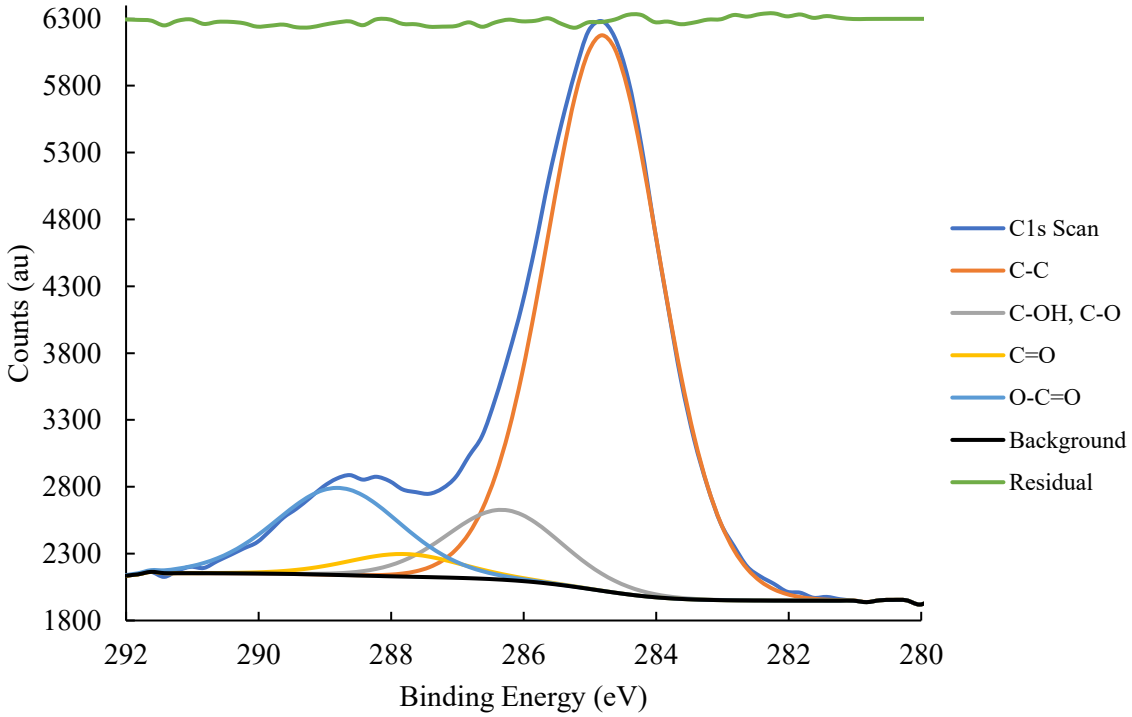

Figure 2.13: High resolution XPS spectra of the carbon 1s peak for MP+H_2O_2 sample 3.

XPS spectra were also taken for wire samples with a variety of surface finishes, the compositional data is summarized in table 2.3. Only one spectrum from each type of surface finish was captured. The fits used for the nitinol plates were also applied to the wire samples with only some minor modifications. The fine drawn as received sample started out with a relatively high Ti/Ni ration. When the water treatment was applied the nickel, peak disappeared into the noise. When the hydrogen peroxide treatment was applied we found the Ti/Ni ratio greatly decreased due to an increase in the amount of Ni detected. When the as received oxide layer was removed the Ti/Ni ratio was also found to decrease. The amount of unoxidized titanium metal changed from 8.3% to 7.3% and 8.3% to 1.7% for the water treated and H_2O_2 treated samples, respectively. The titanium spectra were very similar to those found for the plate samples. But, instead of a large Ti(III) peak, similar in size to the Ti(IV), we found the percentage of Ti(III) was 6.3%, it was 32.5% for the plate samples. Nickel was found in the $Ni(OH)_2$ state for the AS sample, with a 2p3/2 binding energy of 855.68 eV. The H_2O_2 treated nickel spectra is similar to those found for the H_2O_2 treated plates, figure 2.7. Using the same fitting parameters for the plates, we found the nickel component was mainly composed of $Ni(OH)_2$, 77.0%, with some NiO, 23.0%. There was no indication of any metallic Ni(0) present. The as received sample may have contained some NiO but the Ni 2p peaks was too small, relative to the noise, to properly fit multiple peaks. The Ni2p peak for the G600 samples had a binding energy indicative of a metallic species. Both the G600 sample and the water treated G600 sample have a Ni2p3/2 peak at 851.9 eV, indicative of Ni(0). No Ti_2O_3 O1s peaks were needed to fit the wire samples but the binding energies between that and the C-O peak are very close. The Ti_2O_3 signal is likely contained within the C-O peak. To fit the AS sample spectra for the O1s peak a sub-peak at 534.7 eV had to be added, 6.6% of the O1s content. This

binding energy was much too large for a hydroxide peak, ~533 eV and its nature is unknown, not matching any reasonable species. This was the only sample with this unknown peak.

Table 2.3: Shown below is the atomic percent composition of the five different sample types. Only a single sample was scanned from each group. The individual atomic peaks are broken down into the percentage of each chemical species found on the material. The Ti/Ni ratio is also given. The G600+WT C1s data could not be included, the entire peak was not included in the spectra. The "*" in the AS column indicates we cannot be certain of the distribution of NiO and $Ni(OH)_2$.

	G600	G600+WT	AS	AS+WT	AS+H_2O_2
O1s	29	23	66	20	39
C1s	67	73	25	77	56
Ni2p	1	0	1	0	2
Ti2p	3	4	4	9	4
Ti/Ni	5	20	12	NA	2
C1s					
C-C	81	-	76	50	58
C-OH, C-O	12	-	17	43	21
C=O	2	-	3	2	16
O-C=O	5	-	4	4	5
O1s					
Oxide	32	43	40	19	33
C=O	25	8	23	39	46
C-O	41	49	31	42	21
Unknown	0	0	7	0	0
Ni2p					
$Ni(OH)_2$	0	0	100	0	77
NiO	0	0	*0	0	23
Ni Metal	100.0	100	0	0	0
Ti2p					
TiO_2	73	80	85	88	85
Ti_2O_3	4	9	7	2	10
TiO	7	2	3	3	4
Ti Metal	16	8	6	7	2

2.4.2 Nitinol Wire Potentiodynamic Experiment

The results for the potentiodynamic experiments are listed in table 2.4. Nitinol wire samples were prepared using a variety of surface treatments. The samples were

tested in two different electrolyte solutions. The as received samples exhibited the lowest breakdown potential of all the surface treatments. The acidic NaCl-HCl solution decreased the breakdown potential and increased the corrosion potential for the as-received sample. In figure 2.14, the cyclic voltammetry curve is plotted for three as received samples. Figure 2.15 shows the CV plots of two 600 grit samples (G600), one water treated (WT). Figure 2.12, shows the CV plots for two G600 samples, one is water treated. Both the as received (AS) and the as received and water treated (AS+WT) samples exhibit a similar curve with oxide breakdown and severe corrosion beginning around 800 mV. The AS sample tested in the acidic solution exhibits a similar catastrophic breakdown, albeit at a lower potential. But, the AS sample in the acidic solution has a larger current density across all potentials. In acidic solutions, at low potentials, there is a large current spike followed by a dramatic drop in current. This spike is indicative of the shift from the active to passive region in a metal, it is illustrated in both figures 2.14 and 2.16. The flade potential, where this transition occurs, becomes more positive as the pH decreases [39]. This potential shift explains why this flade peak was not seen when samples were tested in the NaCl electrolyte as opposed to the acidic electrolyte. Similarly, the acidic electrolyte significantly decreased the H_2O_2 treated samples corrosion potential.

Table 2.4: The results from potentiodynamic tests are tabled below. The breakdown (Eb), repassivation (Ep), and the open-circuit potential (Eocp) is listed for each different surface treatment and electrolyte. The number of samples tested and the number that did corrode is listed. As well, the difference between the breakdown and corrosion potential is listed. The standard deviation is listed beside each value. These potentials are reported relative to the SCE electrode.

Treatment	Electrolyte	Eb (mV)	Ep (mV)	Eocp (mV)	No. Samples	No. Breakdown	Eb-Ecorr
As received	NaCl	780 (60)	280 (10)	-420 (50)	6	5	700 (80)
As received	NaCl-HCl	560 (40)	130 (20)	-329 (30)	5	5	890 (50)
H_2O_2 Treated	NaCl	-	-	-597 (30)	4	0	-
H_2O_2 Treated	NaCl-HCl	-	-	-410 (80)	4	0	-
Water Treated	NaCl	890 (110)	270 (30)	-500 (10)	9	5	1390 (110)
600 Grit	NaCl	870 (80)	230 (0)	-290 (20)	3	3	1160 (80)
600 Grit Water Treated	NaCl	-	-	-510 (10)	3	0	-

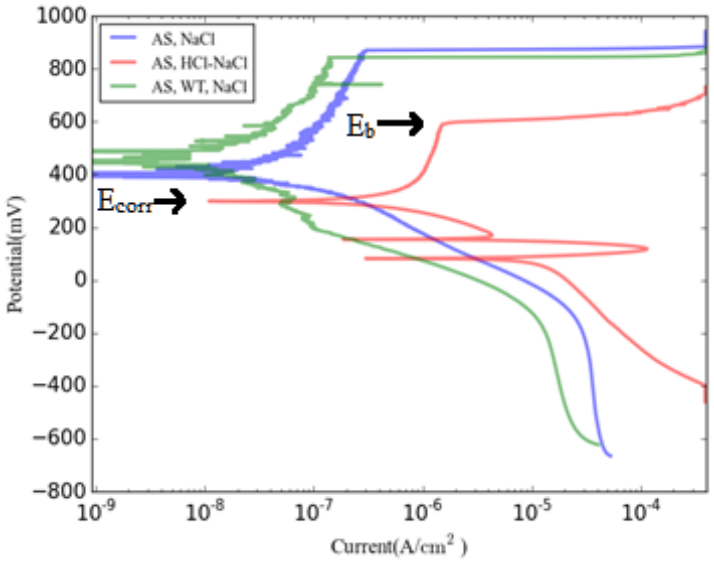

Figure 2.14: Cyclic voltammetry plots for two AS samples tested in a NaCl and a NaCl-HCl electrolyte and an AS+WT sample. The two arrows indicate the typical positions of the breakdown (E_b) and corrosion potentials (E_{corr})..

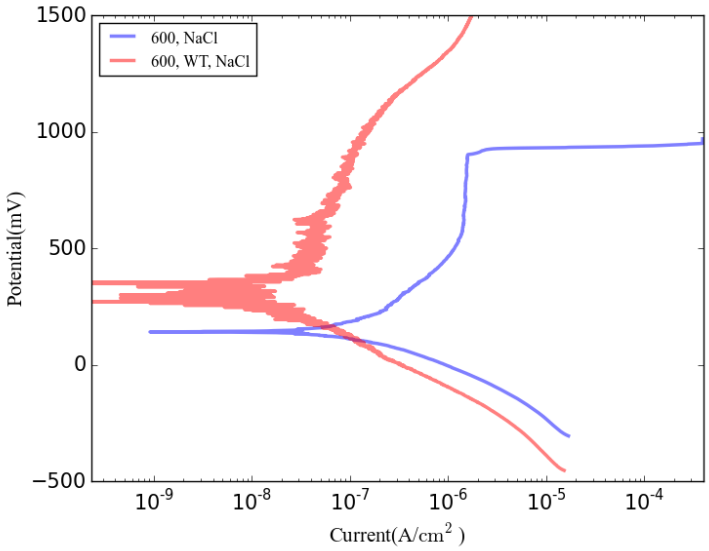

Figure 2.15: Cyclic voltammetry plots for a G600 wire and a G600+WT sample.

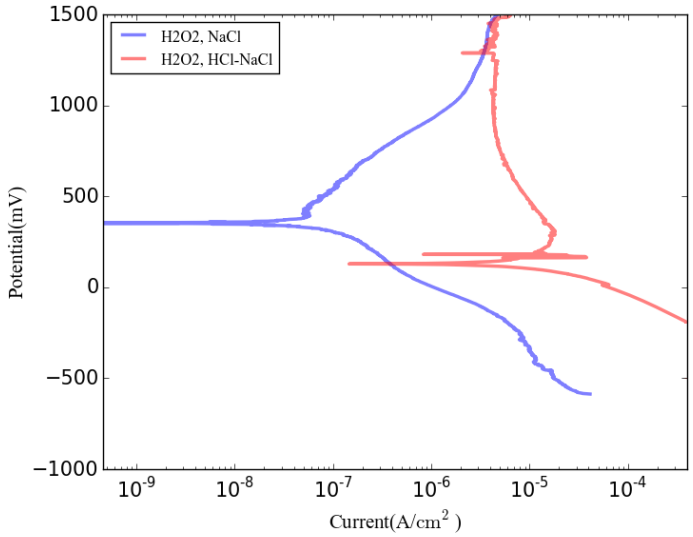

Figure 2.16: Cyclic voltammetry plots for two AS+H_2O_2 samples tested in NaCl and NaCl-HCl electrolytes.

The AS+ H_2O_2 samples tested in both the NaCl+HCl and NaCL solutions exhibited no breakdowns and no corrosion. Cyclic voltammetry plots of the AS+H_2O_2 samples are shown in figure 2.16. As expected, AS+H_2O_2 sample in the acidic solution

has a much higher current density throughout the entire potential range. Both samples show no corrosion up to the 1500 mV, the sample in the NaCl solution exhibits a slight increase in the current as the potential increases. The rate of current increase in the hydrogen peroxide samples tested in the NaCl electrolyte flattens out as the potential increases. This is due to water splitting, which becomes significant at potentials around 1500 mV, leading to an exponential rise in current. In the acidic solution water splitting occurs at a potential well above 1500 mV which is why the current stays relatively constant at high potentials. Hydrogen ions are produced by the oxidation side of the water splitting reaction. This reaction will be inhibited by a large concentration of hydrogen ions and will therefore require a higher potential to occur. The samples which had their native oxide layer removed with 600 grit sand paper had a more noble potential in comparison to the as received samples. The cyclic voltammetry plots for two G600 samples in which one had undergone water treatment is shown in figure 2.15. We can see that the G600+WT sample undergoes no corrosion up to 1500 mV. In comparison the G600 sample has a clear breakdown where the current catastrophically increases independent of potential. When the AS samples underwent water treatment their breakdown potential was not significantly different compared to the AS samples without treatment. But, when the G600 samples underwent the water treatment, similarly to the AS+H_2O_2 samples, no corrosion was detected.

The structure of the oxide layer can be illustrated using low resolution SEM as displayed in figures 2.17 for an AS sample, 2.18 and 2.19 for a AS+H_2O_2 sample, 2.20 for a G600 sample, 2.21 for a AS+WT, and 2.22 for a AS+WT sample. Oxide grains with a width on the order of 1 μm can be observed on the surface of the as received sample. In comparison the AS+H_2O_2 sample exhibited no clearly discernible grains. Cracks can be readily observed across these samples aligned along the axial direction

of the wire. These cracks widely vary in both their width and length. When the water treatment was applied to the as received sample the oxide grains are not as discernible in as in figure 2.14. No visible difference was detected between the G600 sample with and without the water treatment. Figure 2.20 illustrates some residual oxide remaining on the sample surface, a small amount was found on all G600 samples.

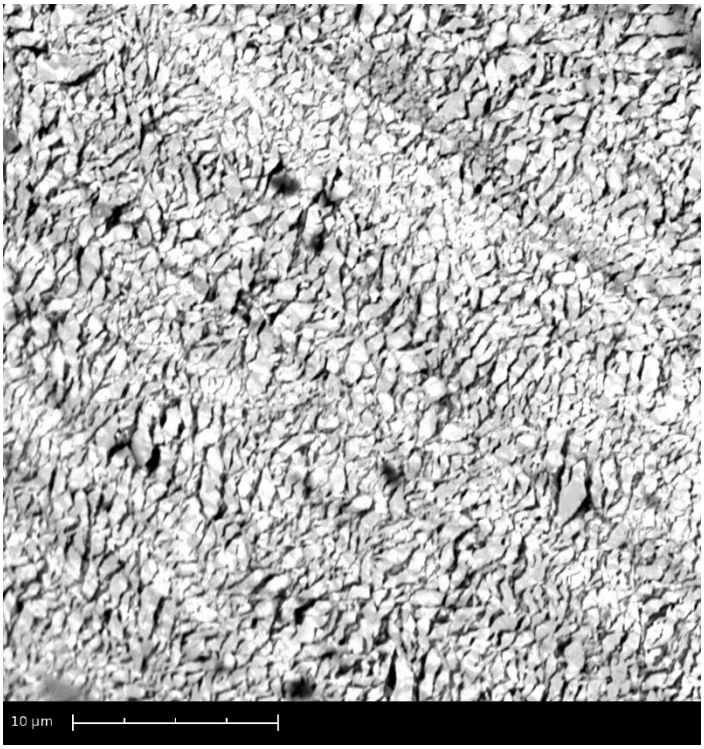

Figure 2.17: An SEM image of an AS nitinol samples oxide layer.

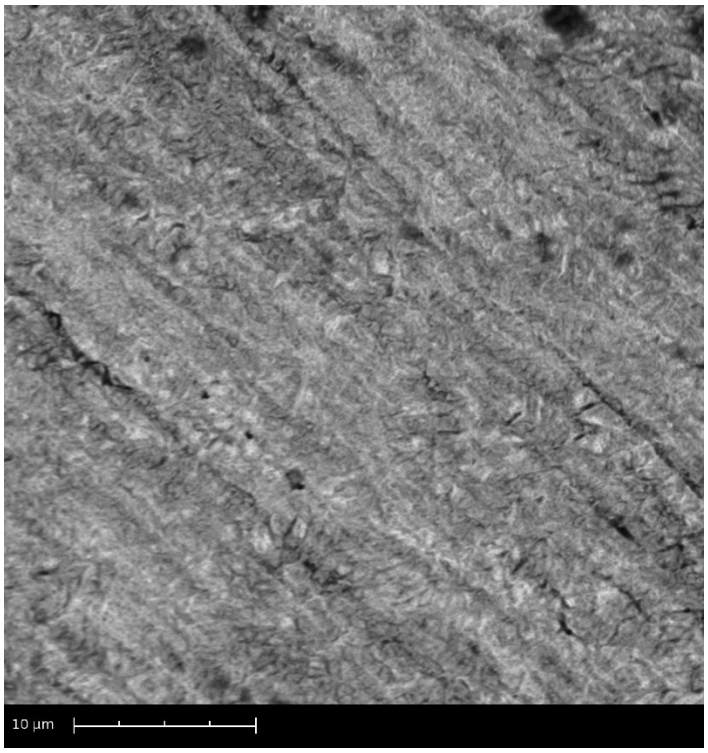

Figure 2.18: An SEM image of an AS+H_2O_2 nitinol samples oxide layer.

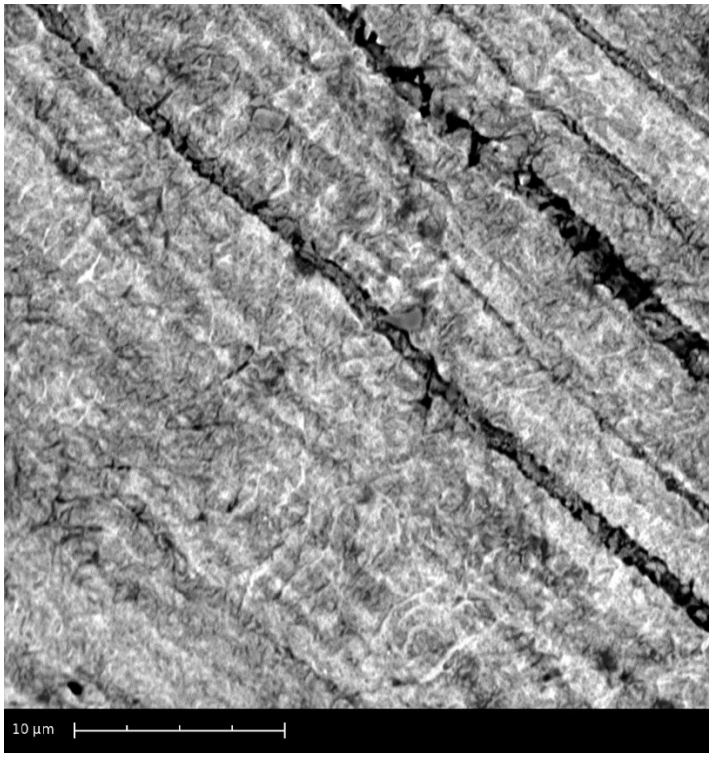

Figure 2.19: An SEM image of a AS+H_2O_2 nitinol samples, the same sample as in fig 2.15, oxide layer.

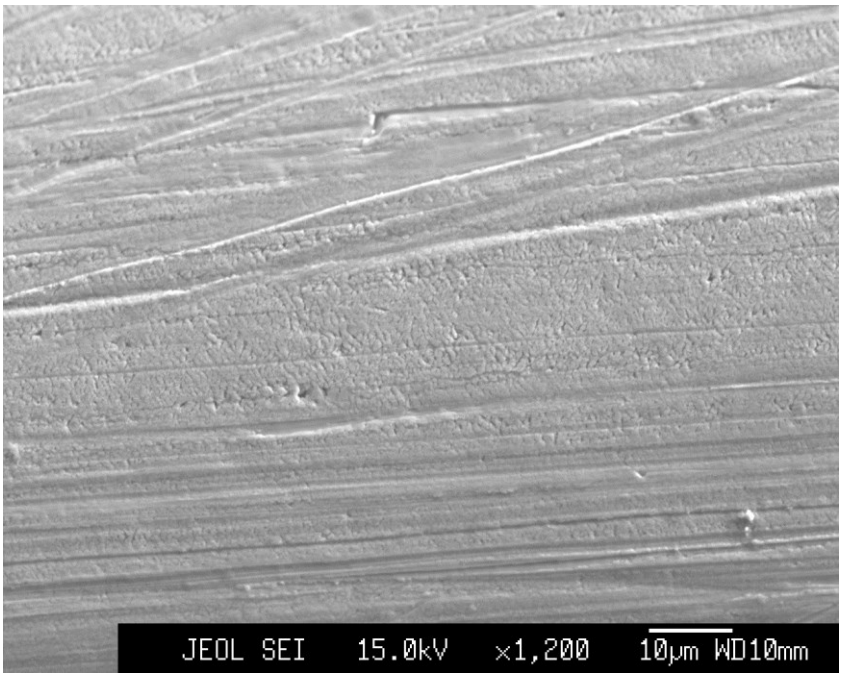

Figure 2.20: An SEM image of G600 nitinol samples oxide layer.

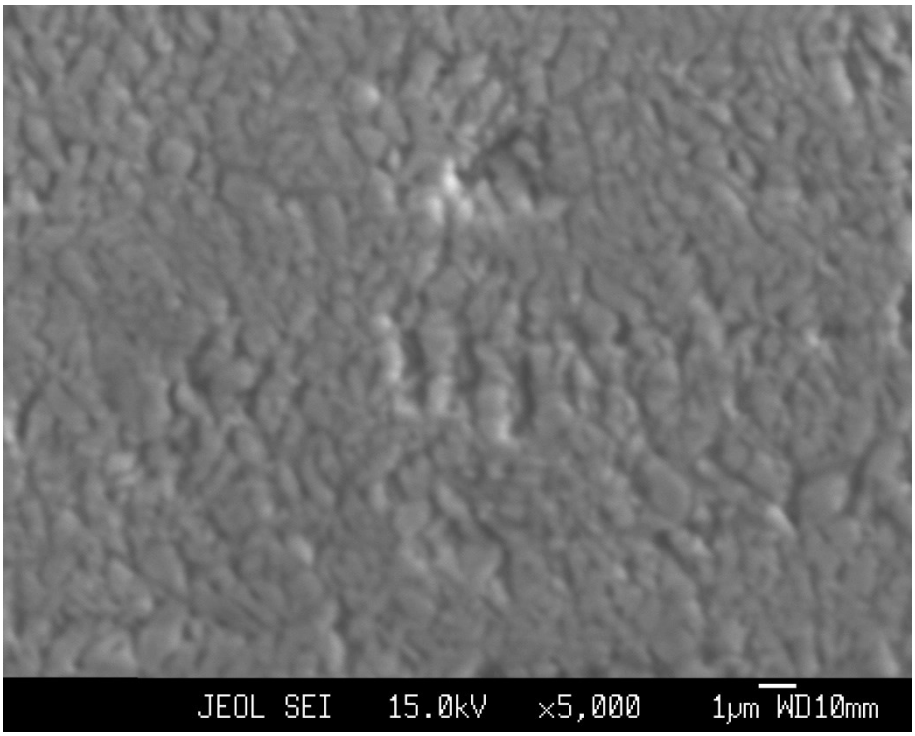

Figure 2.21: An SEM image of an AS+WT nitinol samples oxide layer.

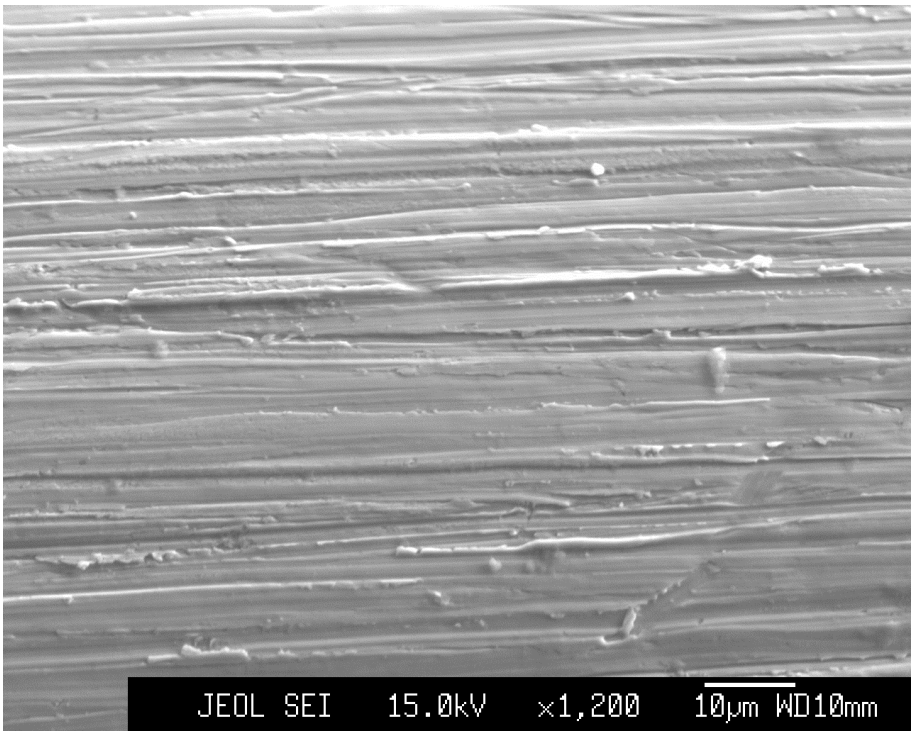

Figure 2.22: An SEM image of a G600+WT nitinol samples oxide layer.

2.4.3 Mass Loss Tests

The data from the mass loss experiment, described in section 2.3.2, is summarized in figure 2.23. The AS+H_2O_2 samples had a far superior corrosion resistance compared to all other surface finishes. The G600+WT samples had a very similar mass loss curve up to day 3 but then it dramatically fell off and approaches the same level as the AS and G600 samples. Extra tests were conducted for day 5 of exposure to confirm this dramatic increase in corrosion. Interestingly the AS+WT samples had a superior corrosion performance compared to the G600+WT samples. There was still a large degree of variation in their corrosion performance after several extra samples were tested. The AS+H_2O_2 samples lost approximately 15% of its mass, after 6 days, while the as received samples lost 47% of its mass after 6 days. The 600 grit samples had a slightly better corrosion performance compared to the AS samples.

One 600 grit sample removed after the third day of exposure was broken in several pieces. The large error bars were likely caused by this one sample fracturing exposing more metal to the electrolyte.

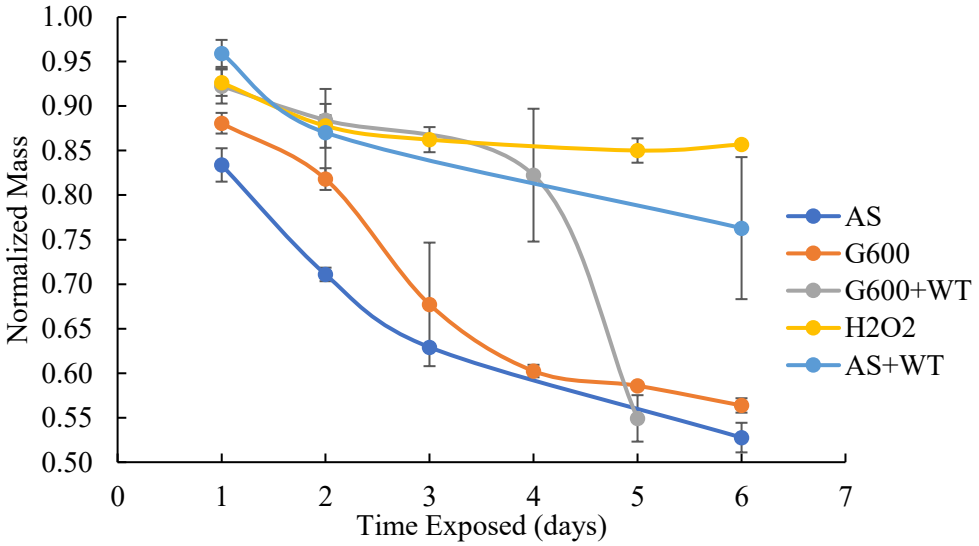

Figure 2.23: The normalized mass loss versus the duration the wire was exposed to .028 M $FeCl_3$ solution for the as received (AS), 600 grit polished (G600), hydrogen peroxide treated (H_2O_2), as received and water treated (AS+WT), and 600 grit polished and water treated (G600+WT).

2.4.4 Disc Imaging Experiment

For the polished discs tested in 1.2 M HCl, 13 out of 14 samples corroded. The average open circuit and breakdown potentials were -78±17 mV and 295±31 mV, respectively. Corrosion always initiated from the edge of the nitinol wires, never from the center. Large hydrogen bubbles formed and obstructed the view of the corrosion process. But, a common thread can be found between the different samples. Corrosion usually initiated from one edge region, sometimes more than one, and propagated as a front across the sample, consuming the surface if experiment was not immediately ended. The applied potential was removed on the order of 15 minutes after the start of an experiment to preserve features shown in the video. After the first corrosion spot

was detected small holes or pits would form in front of this initial region. These holes would spread around the pit until, the small pits expanded enough to merge with the large pit. To allow an SEM analysis the sample surface had to survive the trial. This was the reason repassivation potentials could not be found in this experiment.

Figure 2.24 shows stills from the corrosion of one of the polished nitinol wires. The grey areas correspond to the uncorroded polished nitinol surface. The dark areas are regions that are corroding or are covered obscured by a hydrogen bubble; in this case these bubbles do not obscure the corrosion front. In the first panel, taken 8 minutes and 28 seconds (8:28) after the start of recording, we can see the corrosion front consuming the material. Several hydrogen bubbles are present over the corroded area but none block viewing the corrosion front. Looking along the top right section of the front a dendritic like small area of corrosion precedes the front, indicated by an arrow. In the next panel, 8:37, the corrosion pits are aligned in front of this dendritic line of corrosion, shown by the arrow. These dots can also be seen in the bottom left section of the front in a similar dendritic like pattern, an arrow marks this location. Six seconds later, 8:43, similar dots are found ahead of the front, top right section, while the area previously covered by dots has mainly merged into one continuous dark section. At 8:51 this area around the black dots is similarly corroded until nothing can be observed. At 8:53 and 9:00 we see this process continue, more black dots form ahead of the front which then merge together before new dots are produced further ahead. This sample was destroyed in the corrosion test so no SEM could be performed on it.

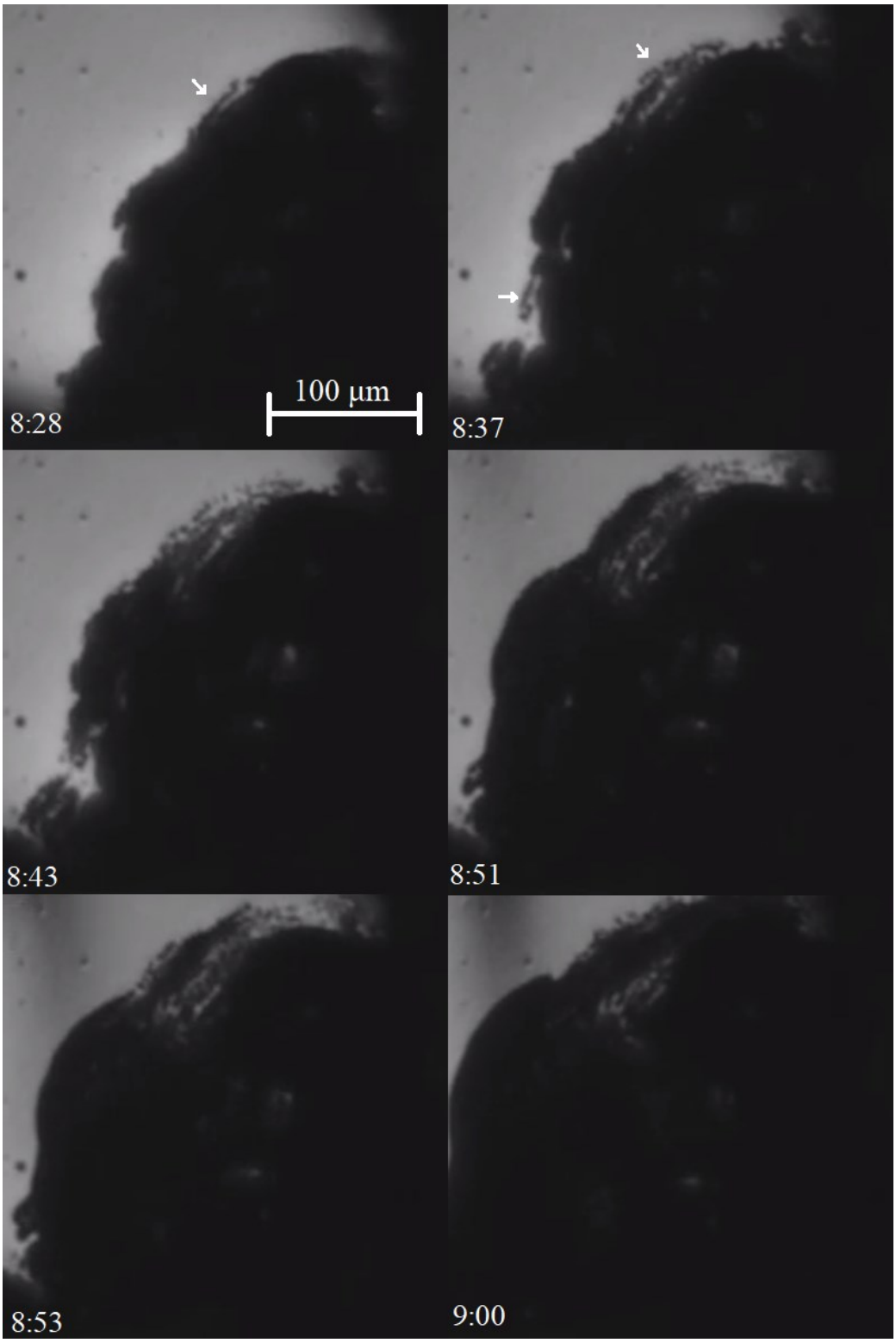

Figure 2.24: Images of the corrosion of 1 µm polished nitinol sample 1, first image was taken at 8:28 and the last one at 9:00. The stamps time are given in units of minutes:seconds.

A similar pattern for corrosion propagation can be seen in another experiment, the image shown in figure 2.25, sample 6. The first panel shows the corrosion that has already occurred up until that point. The second panel, 15:12, shows a dark spot that formed in front of a small corrosion front, marked by a white arrow. At 15:21 we can see that this spot has grown larger in size. At the same time faint, smaller dots can be seen forming the direction of the white curved arrows. Five seconds later, 15:26, corrosion starts to occur at another spot marked by an arrow. Between 15:37 and 15:40 the front expands to the point marked by the arrow. Several dark spots are apparent at the edge of the front which increase in number between 15:37 and 15:40. Going back to the first location, initial arrow, of corrosion the faint spots can be seen expanding towards the corrosion front, marked by the two white arrows. The front then, 16:13, consumes that area between itself and these spots in a rapid expansion. The cyclic voltammetry scan was stopped at that point, to preserve the surface, and SEM was performed.

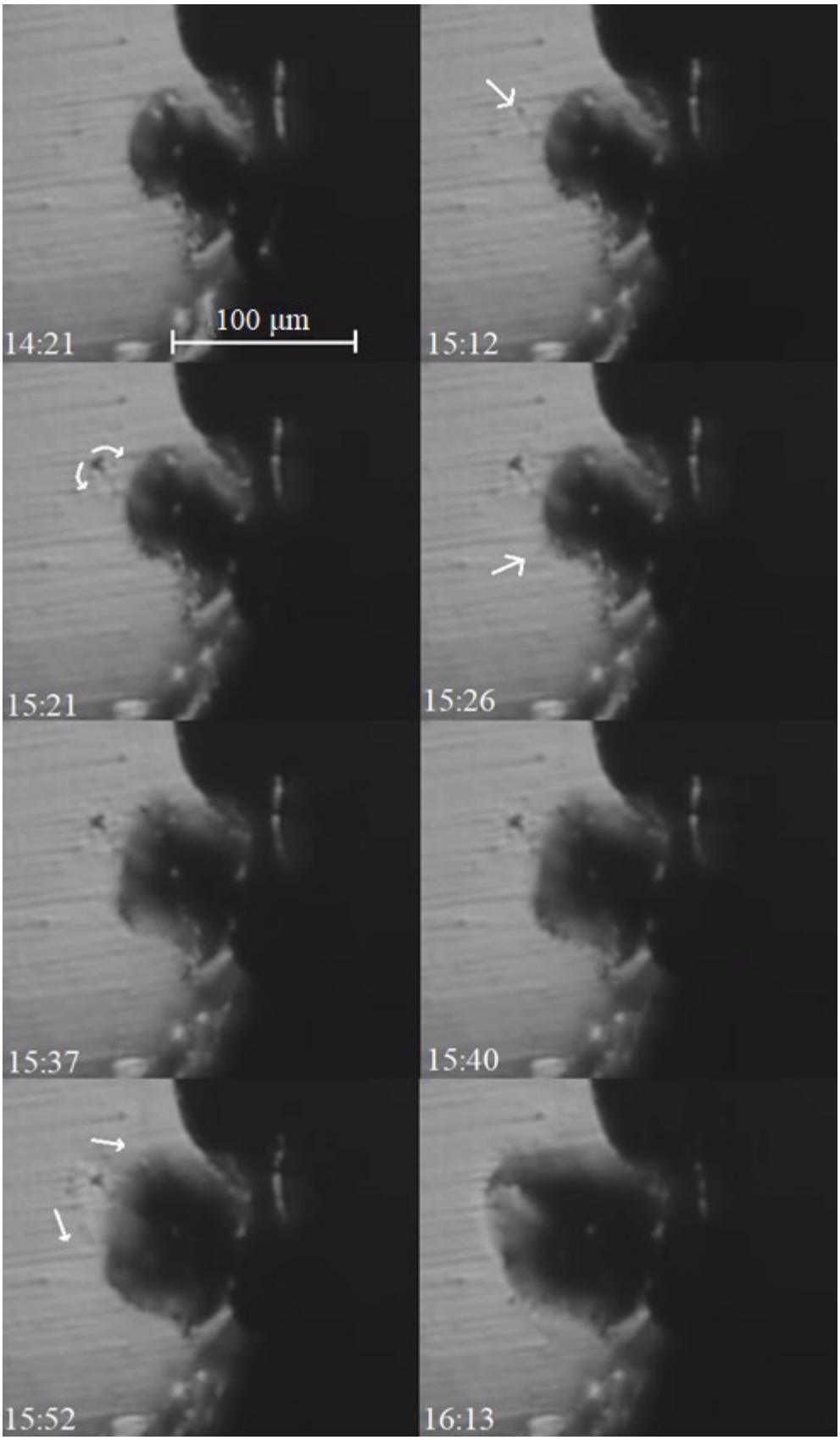

Figure 2.25: Images of the corrosion of 1 µm nitinol sample 6, first image was taken at 14:21 and the last one at 16:13. The stamps time are given in units of minutes:seconds.

SEM micrographs are shown for sample 6 in figures 2.26, 2.27, and 2.28. Several severely corroded regions can be seen in figure 2.26. The area that was investigated in figure 2.25 is shown in figure 2.27. Small holes in the sample can be seen in front of the corrosion pit on all sides. This is very pronounced at the bottom of the image, labeled by the number 1. Where the corrosion pit curves the front of small holes curves with the pit. This front is similar in shape to those that were viewed in the video of the experiment. The array of holes labeled by the number 2 are likely formed from corrosion at the top of the sample, figure 2.26, rather than the corrosion region shown in figure 2.27. The SEM images show the black dots found in the video of the sample are indeed corrosion pits. Similarly, this front like pattern can be viewed in figure 2.28, this region was blocked from view by a bubble during the experiment. Here we see a front of small holes that are located ahead of a corrosion pit arrayed in a front like manner. Clearly these pits are not randomly aligned, but instead are structured in a circular pattern around different regions of corrosion. We can see a very similar feature at the top of the sample in figure 2.26. Similar features are present around the large hole that formed in the bottom of the sample. These can be seen in the remaining undissolved areas on the edge of the sample.

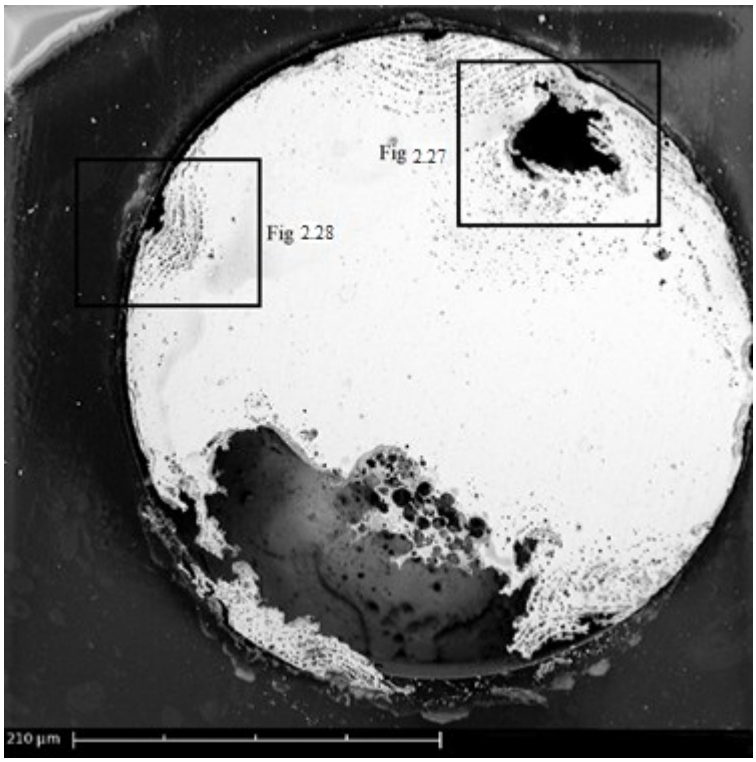

Figure 2.26: An SEM micrograph of sample 6 after corrosion was stopped at, at 16:13 as shown in figure 2.25. The dark grey region surrounding the nitinol disc is the protective heat shrink Teflon tubing.

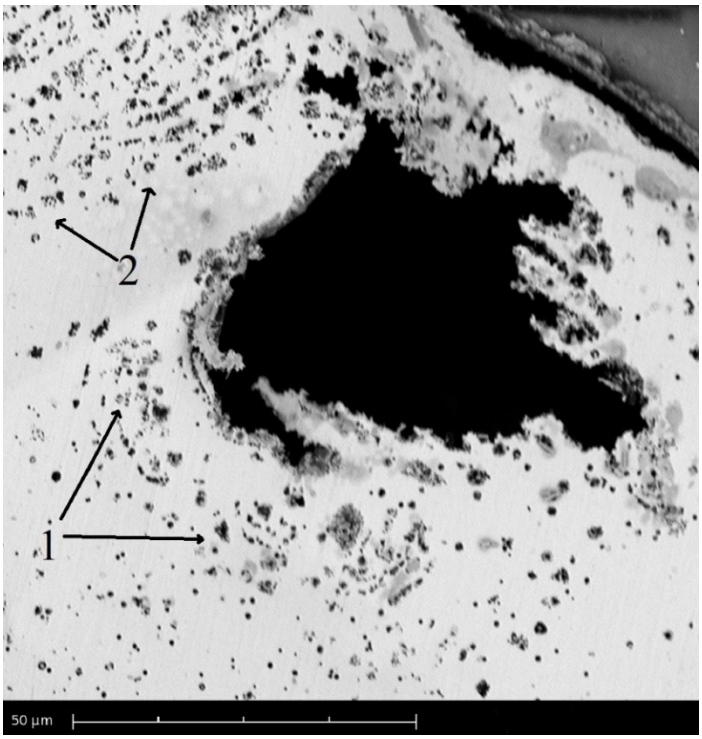

Figure 2.27: An SEM micrograph of the region of corrosion on sample 6, which was shown in figure 2.25. The Teflon heat shrink tubing, dark grey, can be seen in the top right hand corner. Number 1, indicates a corrosion front derived from region of corrosion found in this image while the front labelled by number 2 is from a neighboring, unseen, region of corrosion.

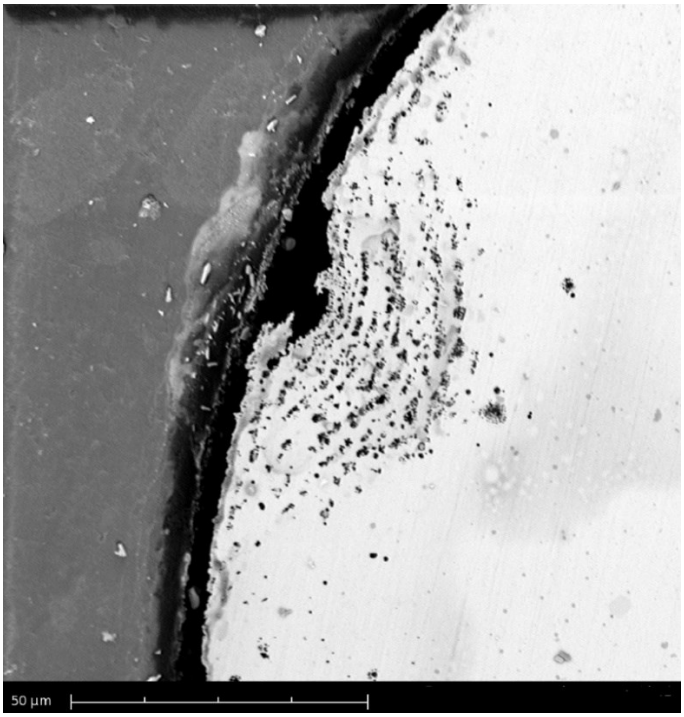

Figure 2.28: An SEM micrograph of the region of corrosion on sample 6, this area is located on the left-hand side of figure 2.26. The dark grey region on the left of the image shows the Teflon heat shrink tubing.

Sample 14 displayed a similar pattern for the propagation of the corrosion front to both samples 1 and 6, figure 2.29. Starting at the first panel, at 17:52, a similar front of corrosion pits is formed. These pits form around the corrosion front with a circular patter that was found in several other samples. In this sample the front propagated from the top to the bottom of the surface cutting it in half. The front in this case does not extend to the new formed corrosion pits like occurred in samples 1 and 6. But, even without this expansion the corrosion pits form on the surface of the sample in the same way. SEM micrographs were shown in figures 2.30, 2.31, and 2.32 for sample 14. The circular front of small corrosion pits that was shown forming in figure 2.29 can be seen in figure 2.31. This front is further away from the larger corrosion region seen in both sample 1 and sample 6. In the other two samples the fronts of corrosion pits were found close, on the order of 2 μm, to the larger corrosion region. In figure 2.32 we see a more typical structure of the small pit corrosion front. There are smaller corrosion pits that are located away from the main corrosion front which have their own small corrosion pits forming a circle around this larger pit. This phenomenon can be seen in several places in figure 2.32.

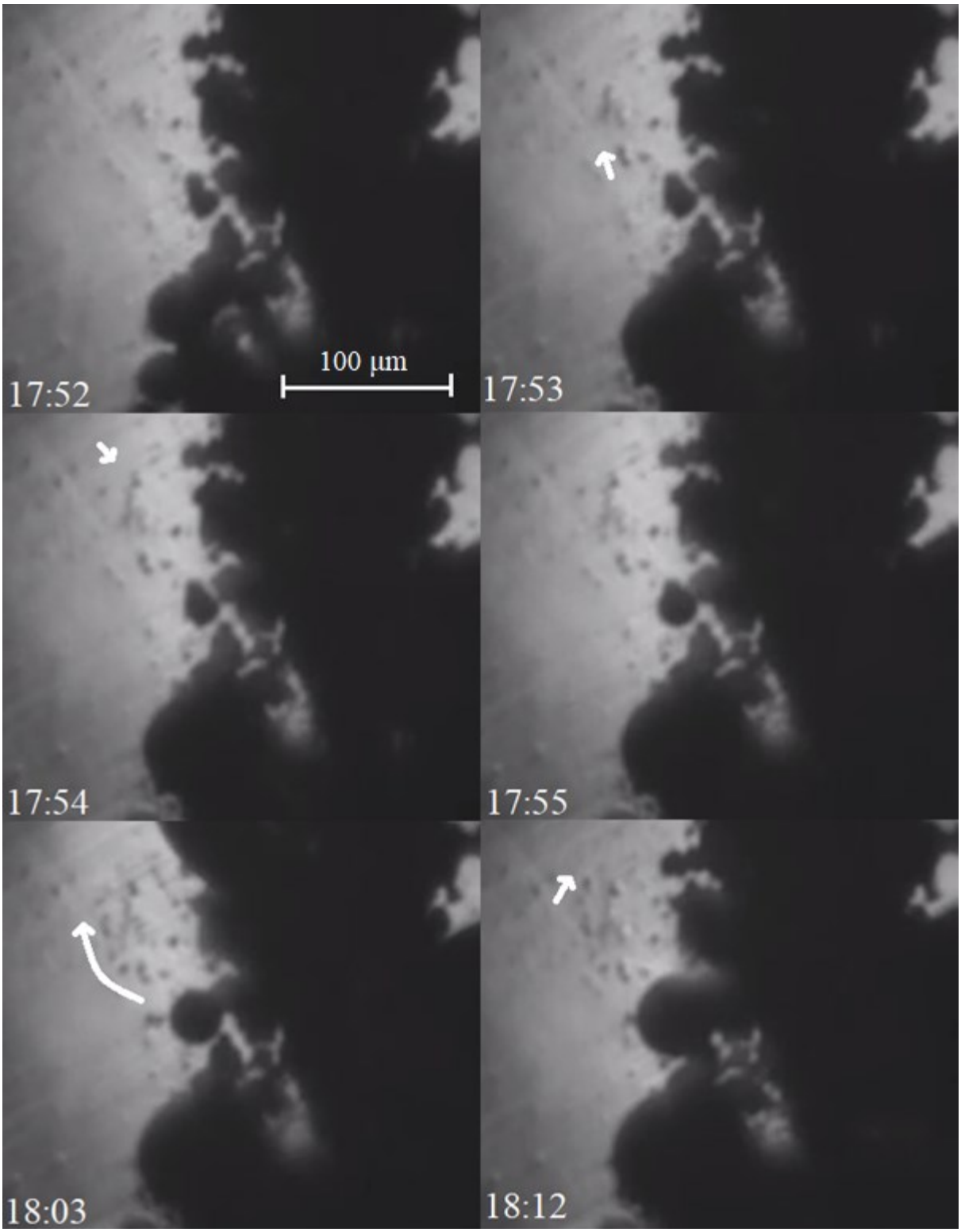

Figure 2.29: Images of the corrosion of 1 µm nitinol sample 14, first image was taken at 17:52 and the last one at 18:12. The stamps time are given in units of minutes:seconds.

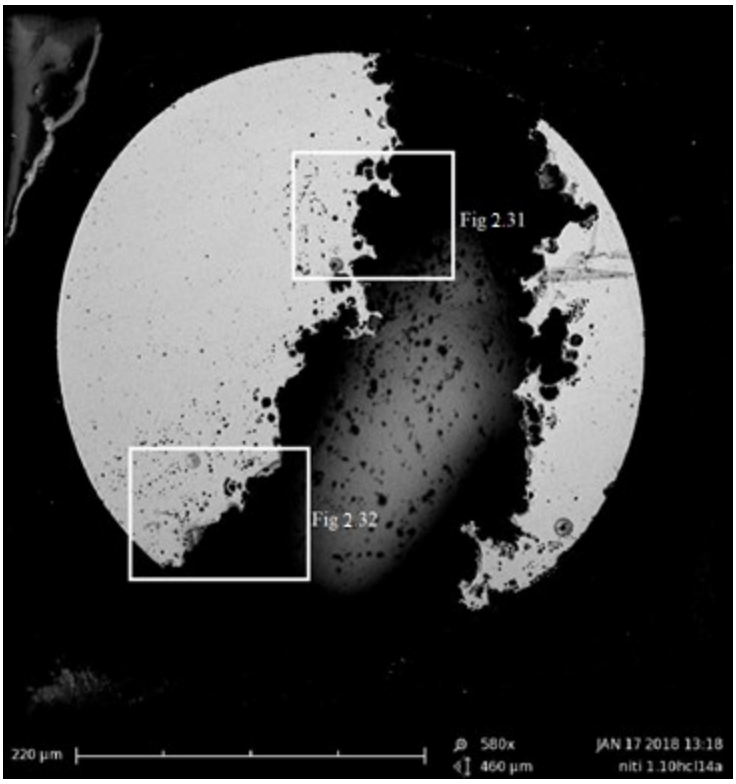

Figure 2.30: An SEM micrograph of sample 14 after corrosion was stopped at, 18:12 as shown in figure 2.29. The heat shrink Teflon tubing surrounds this nitinol disk but can only be faintly seen.

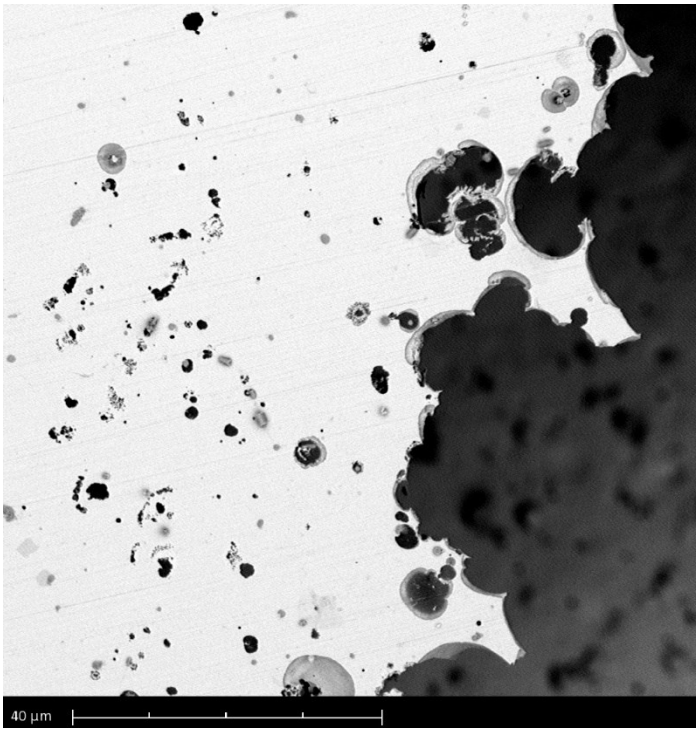

Figure 2.31: An SEM micrograph of the region of corrosion on sample 14, which was shown in figure 2.30.

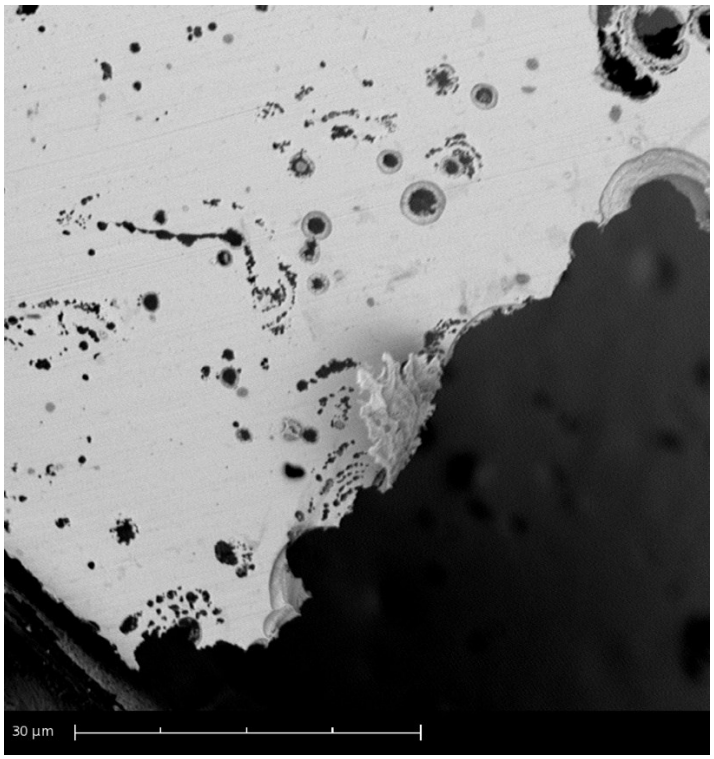

Figure 2.32: An SEM micrograph of the region of corrosion on sample 14, this area is located on the bottom left of the sample on figure 2.30. The Teflon heat shrink tubing can be seen in the bottom left hand corner of the image.

The evolution of a corrosion front is illustrated in figure 2.33 for sample 12. In the second panel, 16:17, a corrosion pit can be seen faintly to have originated on the sample surface. This pit grows quickly and more faint pits can be seen growing in front of it, 16:23. More pits grow to the left of this initial region of corrosion. The shadow that moves across the sample in each frame, except 16:39, is a stream of metal particles that are being released from the corrosion pit into the solution. In the final frame we can make out new corrosion pits that are beginning to form in front of the old region of pits. The corrosion pits varied in size from ~1 µm to several µm in their various stages of growth. In some samples the small corrosion pits are quickly consumed by the larger front while other times the main front does not expand up to these smaller fronts. But, due to limited visibility caused by hydrogen bubbles much of the corrosion front cannot be viewed for the duration of the experiment. Therefore, it is hard to tell

if these fronts of small pits are always consumed by the large front, and in our case if the experiment was stopped before this could occur.

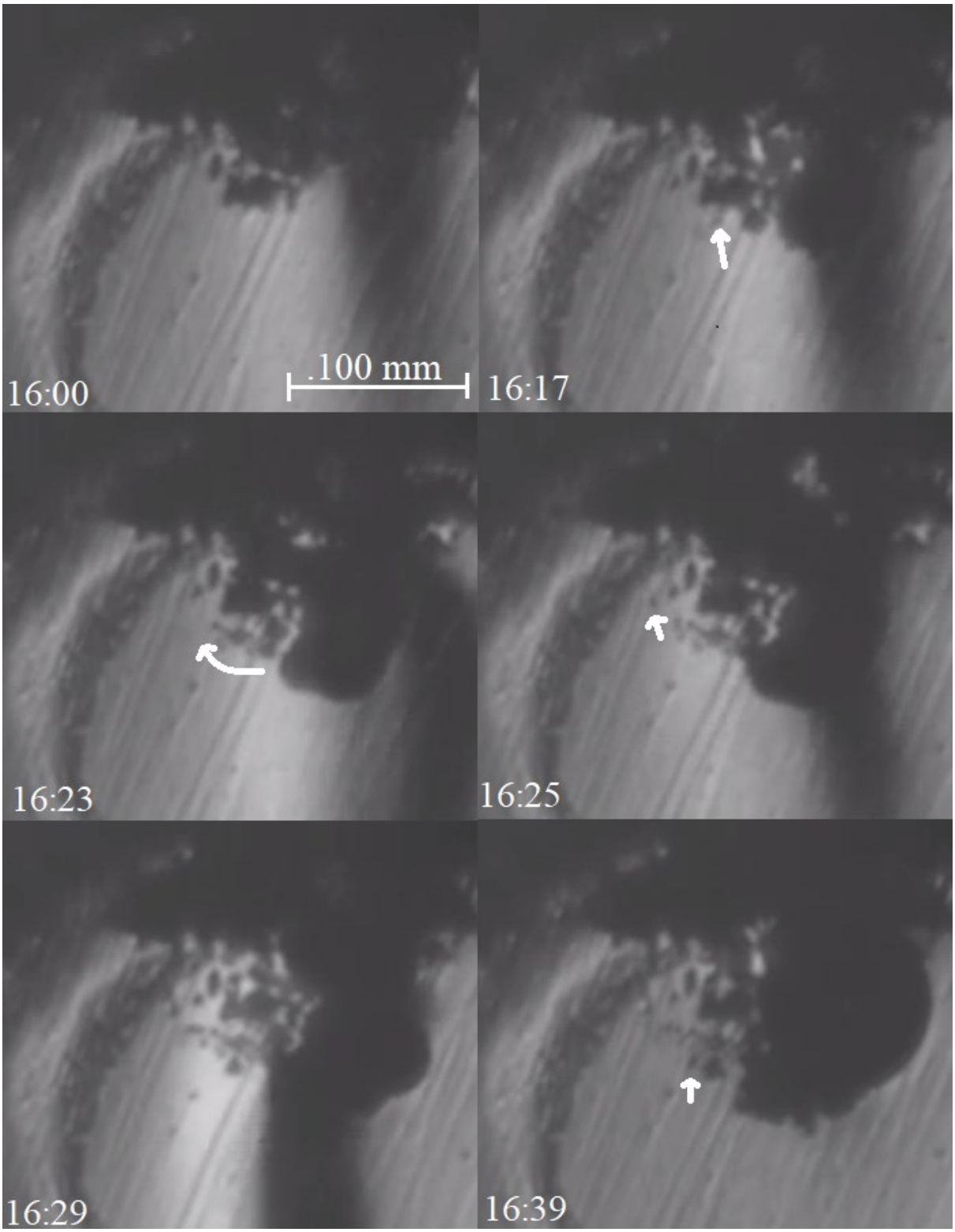

Figure 2.33: Images of the corrosion of 1 μm nitinol sample 14, first image was taken at 16:00 and the last one at 16:39. The stamps time are given in units of minutes:seconds.

2.4.5 Grazing Incidence X-Ray Diffraction

The background scan for the double-sided tape, incidence angle of 1°, is shown in figure 2.34. This scan has three peaks which are found at 14.1º, 23.8°, and 26.3º. There are no diffraction peaks from 26.3° until 90º. Figure 2.35 shows the GIXRD plot for two 1 μm polished nitinol plate samples. There are three clearly visible peaks in each of the two samples at 42.4º, 61.9º, and 78.1° for sample 1 and 42.9º, 61.9º, and 78.9° for sample 2. These three peaks appear in the all three types of samples but the two peaks at ~61.9º and ~78º differ in relative intensities between different individual samples. Using the QualX software these GIXRD plots were matched to the austenite phase of nitinol, a plot of the peak positions for austenite overlayed with the experimental data from one trial is shown in figure 2.36. The first two peaks found in this plot were not accounted for by the austenite phase. The second peak located at 25.7° overlaps precisely with the largest peak from the TiO_2, anatase phase. This will be elaborated on in the next paragraph. Figure 2.37 shows that when the angle of incidence is reduced from 1.5º to 1° the signal from these peaks decreases. If the two peaks do indeed correspond to TiO_2 you would expect the signal to increase as the angle is decreased, when the measurement is more surface sensitive. When the angle of incidence is set at 10º the peak at 25.7º overlaps with the peak from the background tape scan, 26.0º. Therefore, the peak at 25.7º could be due to the tape background not the oxide layer. Chu *et al.* attributed this same peak, ~25.7º, to the anatase phase of TiO_2. They used a glancing angle of 1.0º but their sample was thicker, 0.5 μm [31].

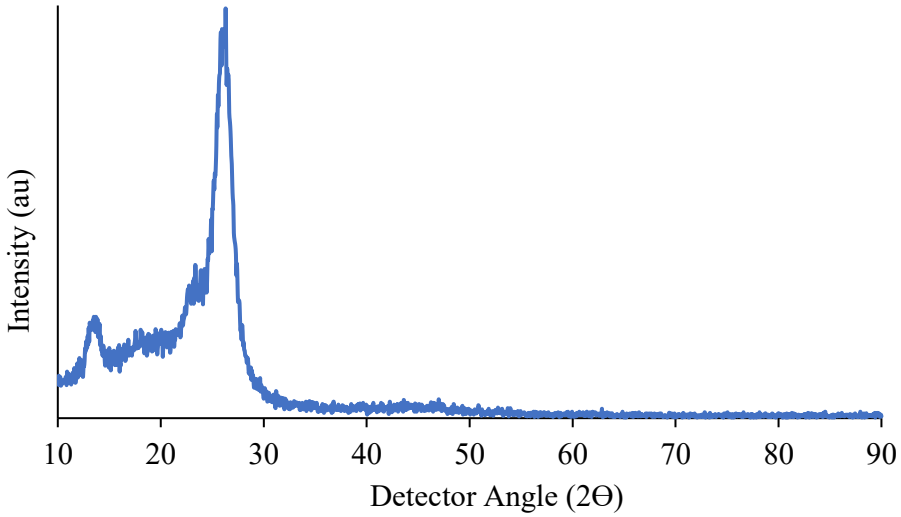

Figure 2.34: The GIXRD plot for the double-sided tape with a 1.5º incidence angle.

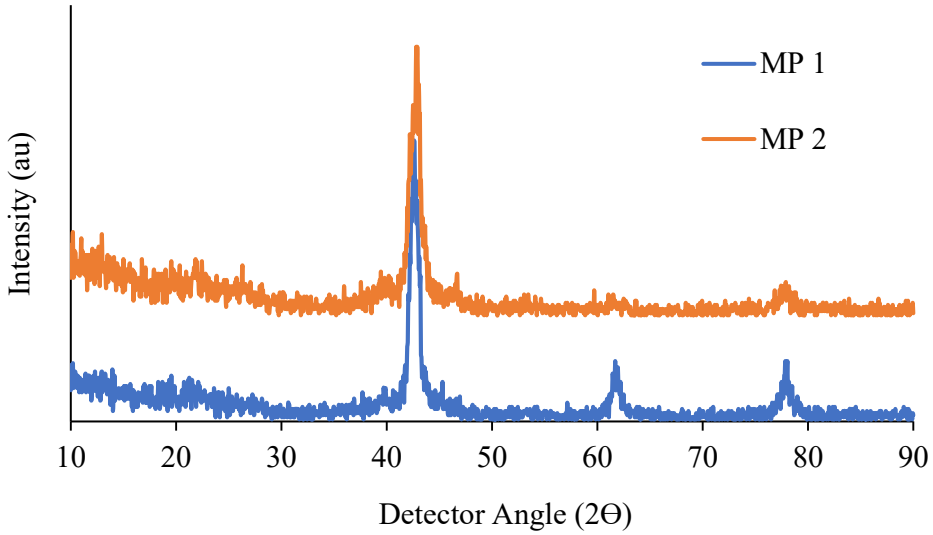

Figure 2.35: The GIXRD plot for the 1 μm mechanically polished nitinol plates with a 1º incidence angle.

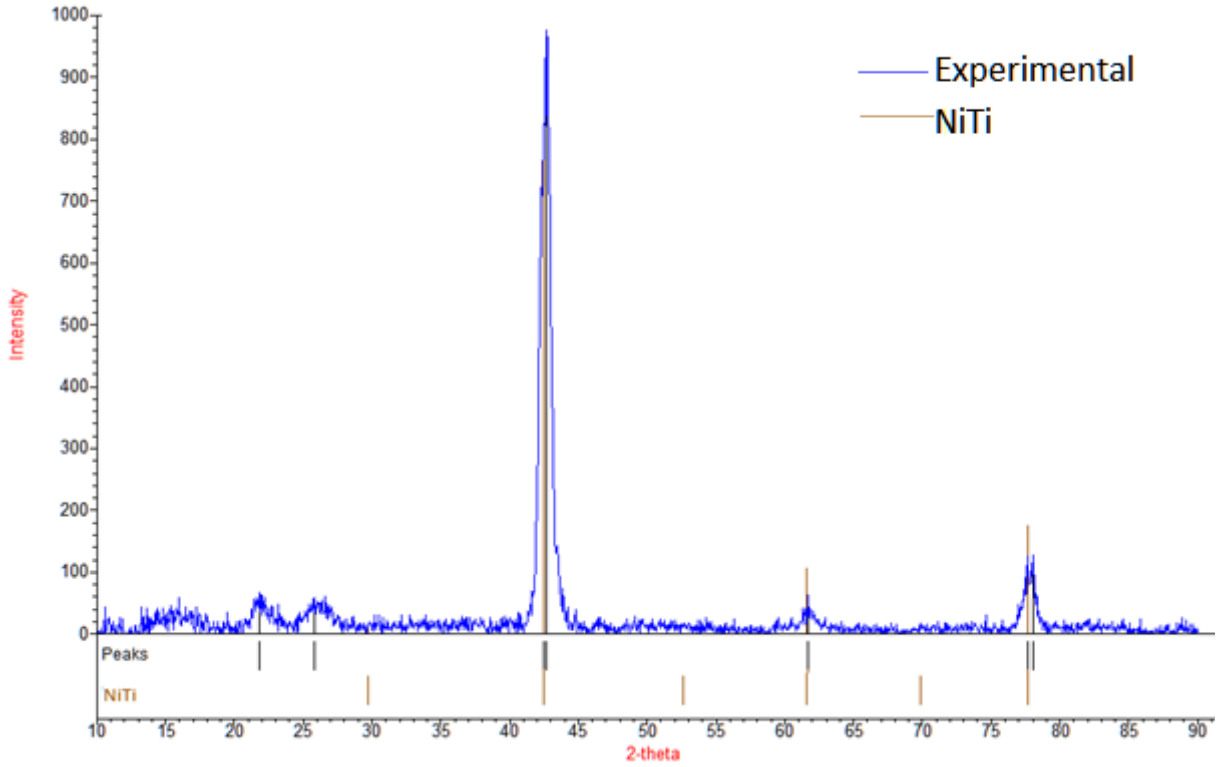

Figure 2.36: The blue curve shows the background subtracted GIXRD scan for the 1 μm nitinol sample 3, angle of incidence 1.5º. The black lines below the GIXRD curve are the locations of the diffraction peaks while the brown lines are the locations of the experimentally derived austensite peaks.

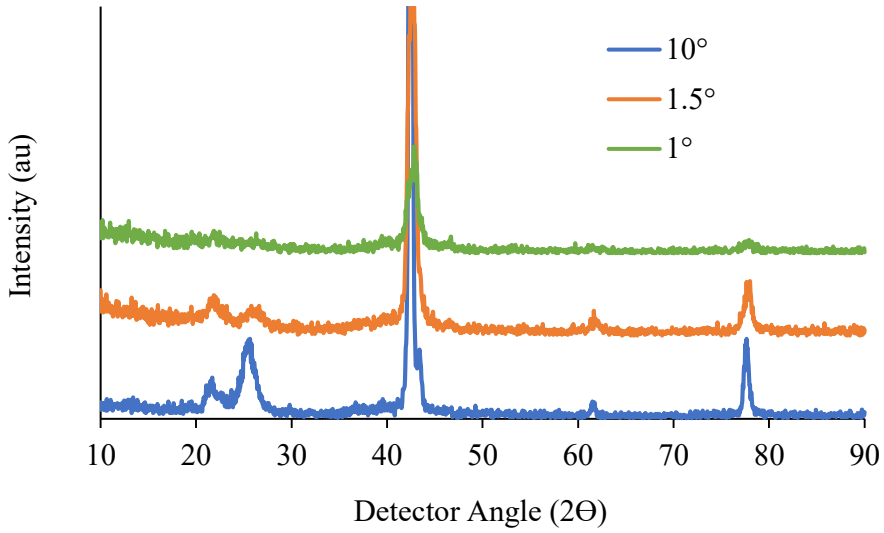

Figure 2.37: The GIXRD plot for 1 μm polished nitinol plates with angles of incidence angle of 10°, 1.5º, 1°.

The two groups of treated samples exhibit very similar GIXRD plots to those from the polished samples. All three groups of samples exhibited peaks at 46.8º. These peaks were the most well defined and the largest for the H_2O_2 treated samples then followed by the WT and then the MP samples. This peak is generated by the Ni_3Ti phase, Ni_3Ti is known to be created from the high temperature oxidation of NiTi, this spectrum is shown in figure 2.37 which compares an experimental H_2O_2 spectra to the known peak positions of Ni_3Ti. As you oxidize NiTi you create a Ti deficient region at the interface between the oxide and the substrate, described in section 2.2.7. The Ni_3Ti XRD spectra also contributes to the peak that merges into the right-hand side of the tallest austensite peak. The same experimental spectrum was also used in figures 2.41, and 2.42 as was used in 2.40.

In figure 2.41 we compare the anatase peaks to the experimental spectrum. It would be surprising that definite TiO_2 peaks were not detected for the H_2O_2 samples, due to its thicker oxide. The anatase peak matches up very closely to the peak located at 25º as stated in the previous paragraph but could be due to the double-sided tape. Similarly, there is a good matchup for the peaks located at 37.5° and 55°. The anatase XRD spectra has a prominent peak at 48º, very close to the Ni_3Ti peak at 46.8º. But, since the 48° peak does not match the experimental spectra we are likely seeing very little signal from TiO_2. This peak would be small relative to the peak at 25.7º but this would not explain the presence of the peak at 35.7º which is theoretically less intense. The GIXRD pattern shown by Chu *et al.* strongly resembles our own, Chu *et al.* did not show or perform the scan past 40º. They associated this wide peak to be from an amorphous anatase phase [31]. Our MP sample would have a very thin oxide layer, ~2-4 nm, producing a signal of negligible strength. You would expect the signal associated with the MP anatase phase to stay negligible as you increase the angle of incidence, but

it does not. We have evidence for the amorphous anatase phase on the MP+H_2O_2 and MP+WT samples; but, the results for the MP sample at different incidence angles and the lack of a peak at 48º contradicts this. The rutile TiO_2 phase similarly does not match up to the experimental spectra. Rutile is progressively favoured by high temperature (>500ºC) oxidation and therefore less likely, in our case, to be detected in comparison to anatase [30].

NiO peaks overlaid with the experimental data is shown in figure 2.42. We see that the NiO peaks could contribute to the asymmetric large peak, along with Ni_3Ti, at the center of the material. As well, the peak at 37º matches up with the NiO peak located within 0.1º of its given position. But, the NiO peak at 64º is not matched with any experimental peak, the experimental peak close by is not asymmetric. It is also unlikely that there is detectable NiO without corresponding TiO_2 peaks due to the much higher TiO_2 concentration detected using XPS. The same interpretation of the XRD pattern the shown in figures 2.36 and 2.40-2.42, H_2O_2 treated sample 2, holds for the other 8 samples. The Ni_3Ti peak is strongest for the H_2O_2 samples, it is much smaller for the water treated samples and H_2O_2 sample 1. Similarly, we did not detect any definite anatase peaks in any of our 9 samples due to the large 1.5º angle of incidence and contradictory MP results. The GIXRD spectra confirm our samples are composed of superelastic nitinol and contain Ni_3Ti within the top 200 nm of the surface. Ni_3Ti was found to be distributed in a layer close to the metal/oxide interface by Chu *et al.* [46]. To adequately determine if the sample was polycrystalline or amorphous using GIXRD you would need to decrease the angle below the critical angle.

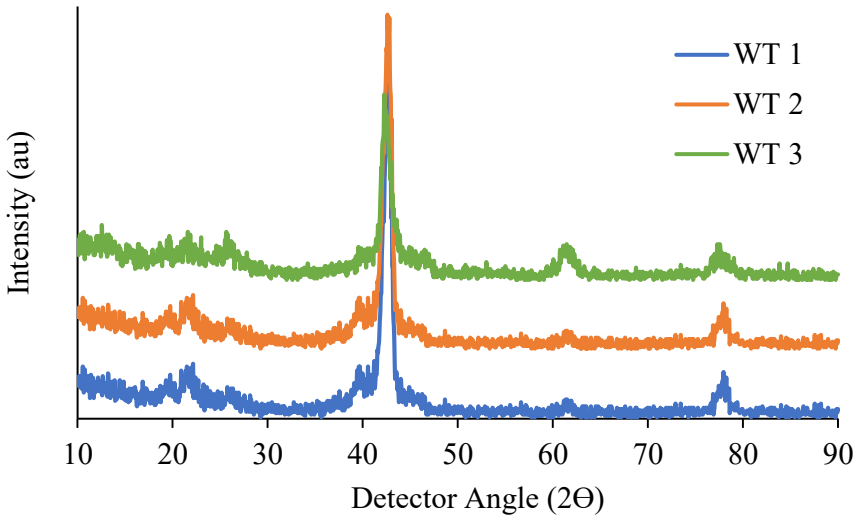

Figure 2.38: The GIXRD plot for the 1 µm polished and then water treated nitinol plates with a 1.5º incidence angle.

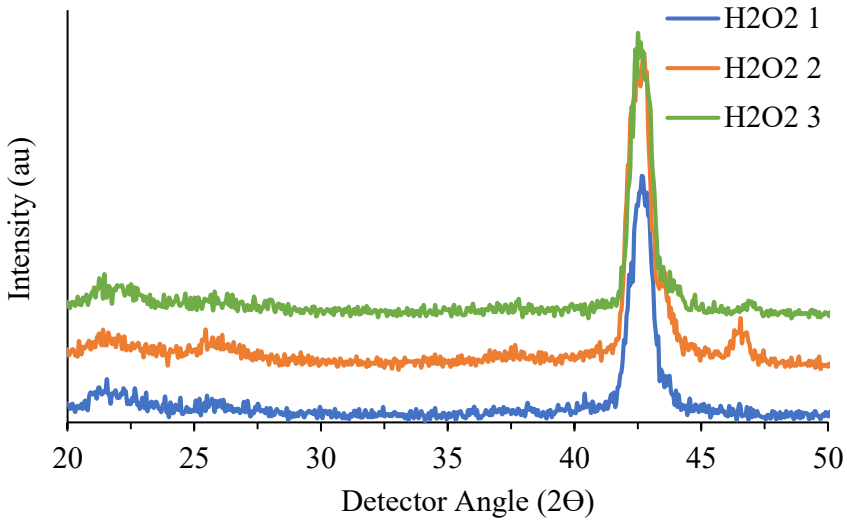

Figure 2.39: The GIXRD plot for the 1 µm polished and then hydrogen peroxide treated nitinol plates with a 1.5º incidence angle.

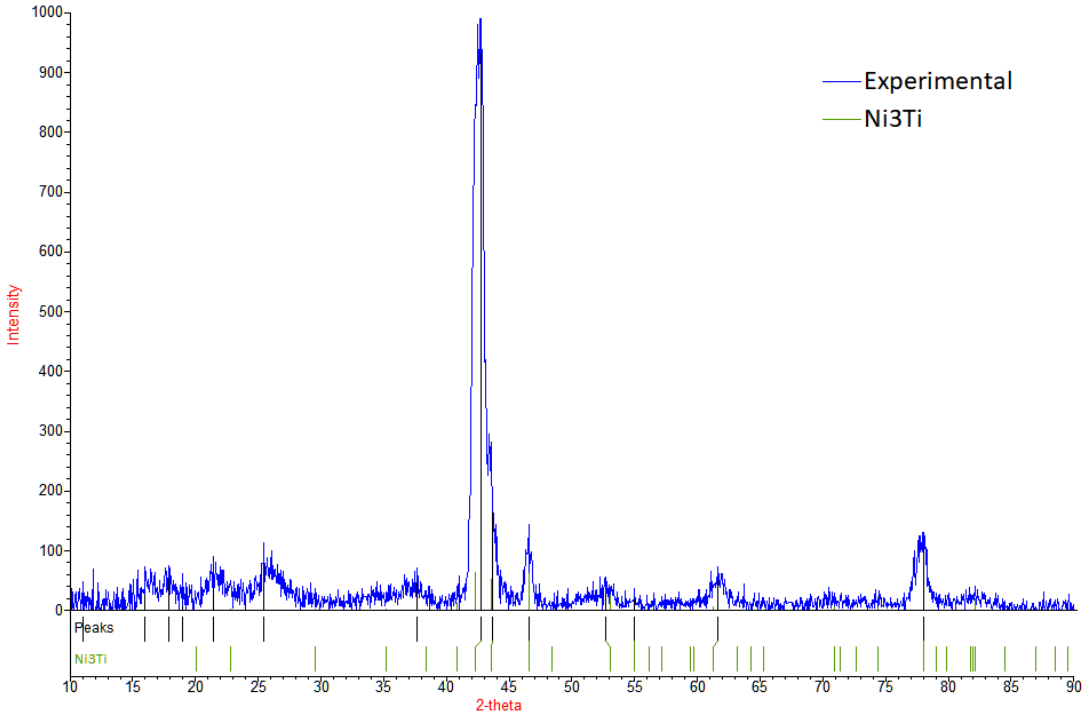

Figure 2.40: The blue curve shows the background subtracted GIXRD scan for H_2O_2 treated sample 2. The black lines below the GIXRD curve are the locations of the diffraction peaks while the brown lines are the locations of the known Ni_3Ti peaks.

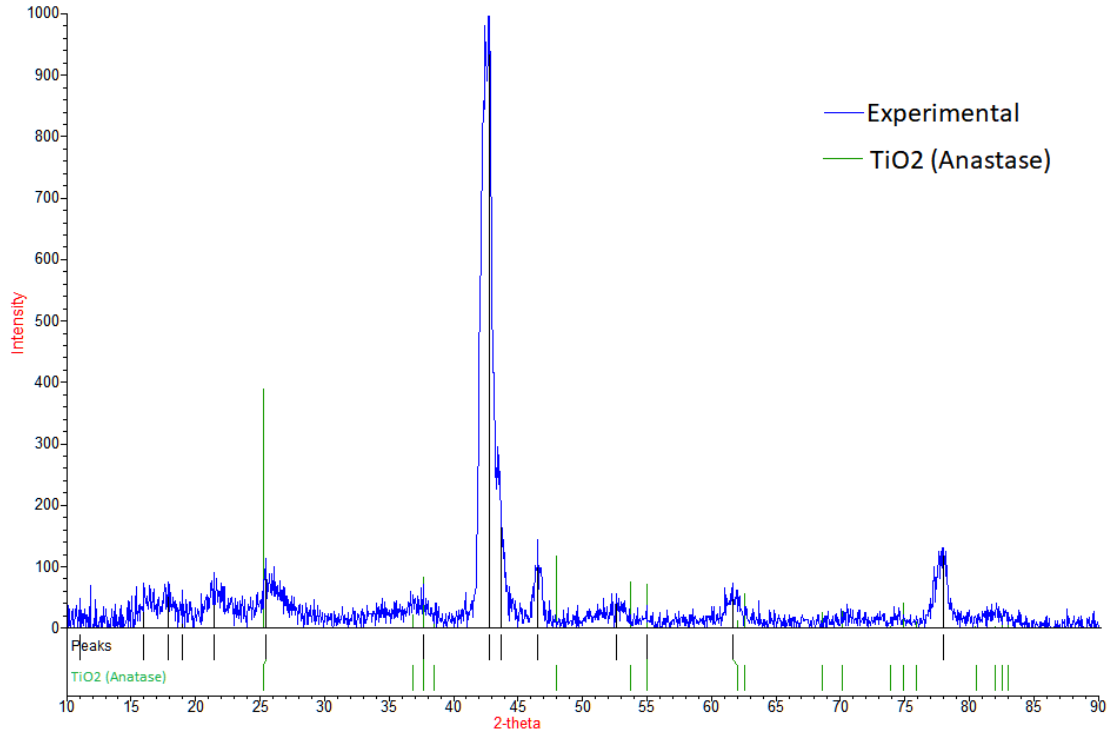

Figure 2.41: The blue curve shows the background subtracted GIXRD scan for H_2O_2 treated sample 2. The black lines below the GIXRD curve are the locations of the diffraction peaks while the brown lines are the locations of the known TiO_2 peaks.

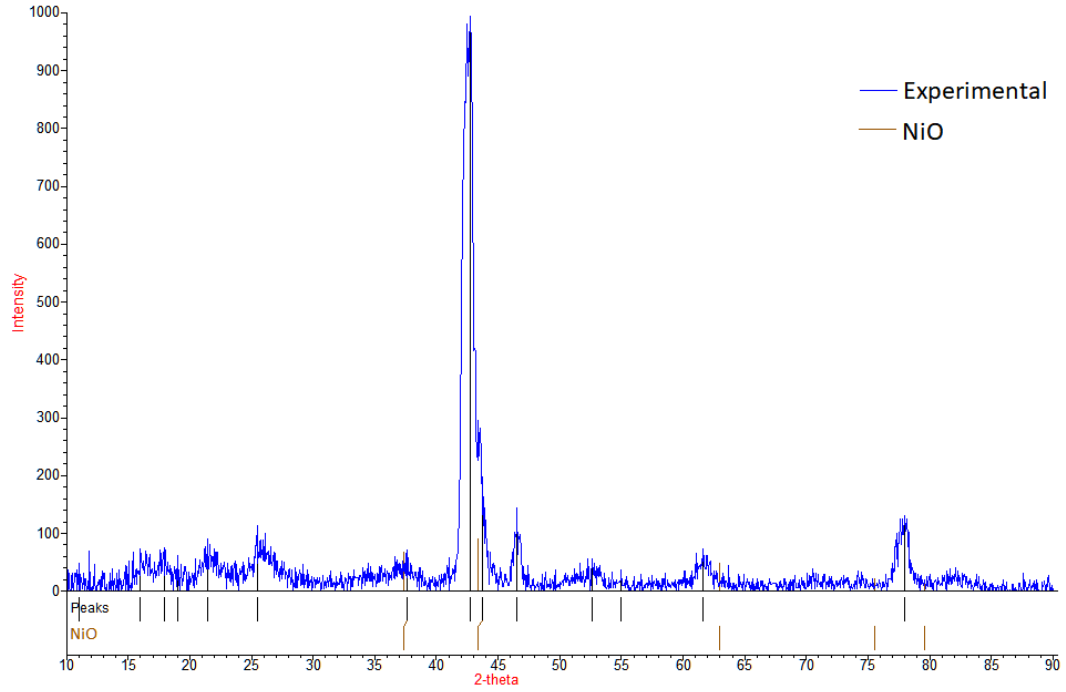

Figure 2.42: The blue curve shows the background subtracted GIXRD scan for H_2O_2 treated sample 2. The black lines below the GIXRD curve are the locations of the diffraction peaks while the brown lines are the locations of the known NiO peaks.

2.5 Discussion

2.5.1 Effect of Surface Finish on Corrosion

The as received oxide layer exhibits the poorest corrosion resistance of all the surface finishes. This trend held when the samples were tested in both the NaCl and the NaCl-HCl solutions. Unsurprisingly the samples tested in the NaCl-HCl solution had a lower breakdown potential. A low pH allows an easier dissolution of the oxide and a greater concentration of hydronium ions, reactants in the cathodic reaction, push the reaction towards greater dissolution. Shabalovskaya *et al*. measured the breakdown potential of a fine-drawn nitinol wire to be 488±58 mV [51] while we found a value of 780±62 mV. They performed their experiments at 40ºC. The heightened temperature would account for some of this gap. An increase in temperature from 20ºC to 40ºC reduced the breakdown potential from 1.22 V and 1.17 V to 1.14 V and 1.08 V

respectively in SS 316 and SS 304 [8]. The remaining gap is likely due to the concentration of inclusions in the surface of the material, and differences in the treatments after the wire was drawn, which will vary between different manufacturers of nitinol. When this oxide layer was removed with mechanical polishing the corrosion performance did increase, but not by a huge margin. While the surface will be roughened the original oxide layer will be removed; a roughened surface, as explained in section 2.2.8, will negatively affect the corrosion resistance but removing the as received oxide will induce the opposite effect. Interestingly considering the superior G600 performance, from our XPS data the Ti concentration and Ti/Ni ratio is larger for the as received oxide compared to the G600 sample. Furthermore, the AS sample had a greater concentration of TiO_2 in comparison to the G600 sample. A greater concentration of TiO_2 in the oxide layer and a larger Ti/Ni ratio does not then guarantee a greater degree of corrosion resistance when comparing between different surface treatments.

When comparing the G600 and AS surface finishes the composition of the surface is not sufficient to predict the relative corrosion resistance. The physical structure and thickness of the oxide layer must also be considered. The as received oxide layer is covered dotted with oxide grains. These high energy grain boundaries are highly susceptible to corrosion. As well, the as received oxide layer is thicker than the air grown oxide which leads to cracking due to unit cell volume mismatch. The grain size of the air grown oxide is unknown, it cannot be observed using SEM. Cracks are higher energy surfaces which are more susceptible to corrosion, section 2.2.8. These properties will also negatively impact the corrosion resistance of the oxide layer. From our data the physical composition of the oxide layer is potentially less important compared to the structure of the oxide layer and its thickness.

2.5.2 The Effect of the Hydrogen Peroxide Treatment

The hydrogen peroxide treatment increased the nickel concentration on the sample surface substantially, approximately seven times in comparison to the MP+WT plate samples. The nickel concentration in our samples decreased when the MP samples were boiled in distilled water. This means that increased concentration of nickel on the surface after H_2O_2 treatment is not due to increased diffusion caused by a greater temperature. Therefore, the oxidation due to H_2O_2 must be responsible for the greater nickel concentration. This result is unlike the one found by Chu *et al.,* who found a substantially reduced surface nickel concentration after a treatment in hydrogen peroxide [31]. They also predicted the $TiNi_3$ layer would not be produced by the H_2O_2 treatment. Since we did not chemically etch our samples, some residual $TiNi_3$ layer should be expected due to the presence of the as received oxide. But, the $TiNi_3$ peak was stronger in 2 of the 3 hydrogen peroxide treated samples compared to the MP samples where it was relatively weak. This indicates that the mechanism proposed by Chu *et al.* may be incorrect or the oxidation mechanism changes when treating non-chemically etched, MP or AS, samples [31]. The increase in Ni was found in both the MP and AS samples, so the presence of the AS oxide cannot account for these differences. This increase was not found in the studies by Shabalovskaya *et al.* and Chu *et al.* [31, 45]. This difference must be due to the lack of chemical etching performed on our samples. Perhaps the peroxide oxidizes the $TiNi_3$ layer preferentially leading to an increase in oxidized nickel species in the material. Or this layer retards the oxidation into the sample as predicted by Chu *et al.* switching the mechanism to the outward growth model proposed by Chu *et al.* [46]. The H_2O_2 treated nitinol Ni2p XPS spectra bear a striking resemblance to the those found by Shabalovskaya *et al.* taken from nitinol samples heat treated at 500ºC for 15 minutes. They also reported the oxides

layer was a similar blue colour indicating a similar thickness [35]. The same researchers also studied the effect of the hydrogen peroxide treatment on the surface chemistry of nitinol. They found the 3% hydrogen peroxide treatment decreased the nickel concentration on the surface of a chemically nitinol from 14% to 5%. But, unlike our own findings their ratio of Ti/Ni was substantially larger, 3:1 instead of our 1:1 ratio [45]. This difference is likely due to chemical etching prior to their treatment. Chemical etching removes the nickel enriched sublayer that provides most of the nickel that would have been oxidized. When nitinol samples were chemically etched prior to heat treatment the resulting oxide layers were depleted of nickel. Without this initial step of chemical etching the heat-treated oxide has a high nickel concentration [35]. The hydrogen peroxide treatment is not uniquely good at creating a nickel free oxide but instead the concentration depends partially on the state of the pre-treatment surface. The hydrogen peroxide treatment does indeed increase the corrosion resistance; but, it has a lower Ti/Ni ratio compared to the MP, AS, and MP+WT samples. As discussed in section 2.2.4, nitinol wires with higher surface nickel concentrations increased the rate of cell death when surrounded by cultured rat cells [26].

Even with a lower Ti/Ni ratio we saw a very large increase in the corrosion resistance of the peroxide samples; eliminating breakdowns in the oxide layer with an applied potential up to 1.5 V, and reducing the current density measured across all applied potentials. Shabalovskaya *et al*. found the H_2O_2 treatment increased nitinols corrosion resistance above the level of chemically etched samples. Their chemically etched samples also exhibited no breakdowns, but the current was reduced at all potentials when the H_2O_2 treatment was applied [45]. This treatment substantially improved the corrosion resistance of the nitinol wires with a fine-drawn golden AS oxide, it inhibited breakdowns up to 1.5V, where oxygen evolution starts to saturate

the measured current. When the pH of the electrolyte was reduced from neutral to 1.2, the hydrogen peroxide treated samples still did not corrode. The peroxide treatment increased the percentage of oxygen deficient titanium oxide, Ti_2O_3, in the oxide layer of nitinol plates, this phenomenon was not found in the H_2O_2 treated as received wires. This may be due to the difference in the surface finish of the two samples. But, ultimately there is no indication from our data or from the literature that an oxide rich in Ti_2O_3 negatively impacts the corrosion resistance.

While this treatment does substantially increase the corrosion resistance the greater nickel content found at the surface is a cause for concern. We were not able to determine with a high degree of certainty if the resulting oxide layer was polycrystalline or amorphous due to the small signal to noise ratio of the oxide peaks. A greater concentration of nickel close to the surface would inevitably increase the amount of nickel leaching out from the stent but due to the thicker oxide diffusion from deeper in the oxide layer would be impeded. The hydrogen peroxide treatment is an easy way to improve the corrosion performance of nitinol wires even without any previous surface treatments, but this comes at the cost of a higher nickel content in the oxide. Any hydrogen peroxide produced around the implant, due to inflammation, will improve the corrosion resistance up to a point, where the increased thickness may eventually induce cracking in the oxide lowering the corrosion resistance.

2.5.3 The Effect of the Water Treatment

The treatment in boiling water improved the corrosion resistance of both the as received and G600 samples. When the AS samples were water treated, some corroded at the same breakdown potential as untreated samples while others exhibited no

corrosion up to 1.5 V. The samples exhibit excellent corrosion resistance when the original oxide layer is removed and then are treated. In this case, no corrosion was detected on any of the samples tested. From the XPS data the water treatment increased the TiO_2 concentration in the oxide layer while reducing the nickel concentration in both the G600 and AS samples. The amounts of both unoxidized titanium and nickel decreased when the samples underwent water treatment. Unoxidized metal should only be found close to the interface between the oxide layer and the substrate, and of course in the substrate. Previous studies have shown that the water treatment combined with chemical etching can substantially increase the corrosion resistance. But, in potentiodynamic sweeps there was no difference detected in the shape of the CV plot or the value of the breakdown potential between chemical etching and chemical etching plus water treatment [51]. The GIXRD data hinted that the oxide formed due to water treatment may be amorphous. More work is needed to determine if this is indeed the case. This study has shown that the water treatment greatly increases the corrosion resistance without prior chemical etching. The water treatment is as effective as both the H_2O_2 treatment and chemical etching at raising the breakdown potential, eliminating breakdowns up to 1.5 V in 0.9% NaCl.

2.5.4 Mass Loss Experiment

The various surface finishes that lost the most mass over time also had the lowest breakdown potentials. The AS samples had the worst corrosion performance and had the lowest breakdown potential compared to all those tested. When this oxide was removed the breakdown, potential did increase by a small but significant margin. We can see that the G600 samples lost slightly less mass over time in comparison to

the AS samples, which mimics this difference in breakdown potential. Moving to the water treated AS samples the picture gets more complicated. The actual breakdown potential was the same as the AS samples for those that did corrode. But, 4 out of 9 samples did not corrode. This is likely the source of the large error bars found in the AS+WT samples. But, if the AS+WT samples that did corrode had the same mass loss behaviour as the AS samples we should expect an even worse corrosion performance. Either the water treatment changed something in the oxide layer that did not influence the breakdown potential but increased the materials resistance to mass loss. Or, 3 out of 4 the mass loss samples would have to be from the non-corroding group in the cyclic voltammetry test. Since the breakdown potential and mass loss are strongly correlated the former seems unlikely. It was unsurprising that the H_2O_2 samples had such good corrosion resistance due to the lower current density from the CV plots and breakdown potential lying above 1.5 V. What was more surprising was the poor corrosion performance of the G600+WT samples and their dramatic decrease in mass between the 4^{th} and 5^{th} days of testing. The water treatment increased the concentration of TiO_2 on the surface of the material relative to untreated G600. As well, other studies have shown it increases the oxide layer thickness relative to atmospheric oxidation. A possible explanation for this poor corrosion behavior is the thinner oxide in comparison to the H_2O_2 sample. A thicker oxide would decrease the diffusion of chloride anions into the oxide-metal interface. The AS+WT would also have a much thicker oxide compared to a G600+WT sample but this would not explain the large difference in the breakdown potential. In this case the high, >1.5 V, breakdown potential did not accurately predict the relative corrosion performance of the G600+WT and the H_2O_2 samples. But, due to hydrogen evolution the relative true breakdown potentials could not be determined. Likely the H_2O_2 samples would have a higher value of E_b.

2.5.5 Comparison Between the Corrosion Treatments

Sullivan *et al*. found that stents with breakdown potentials below 600 mV displayed corrosion after 6 months implanted in porcine arteries [21]. All the nitinol wires tested in this study had a breakdown potential above this value. There are a few caveats in comparing these two values. The first is that the study is testing stents while ours was testing wires. Stents have joints which are more susceptible to corrosion than the purely straight sections of a wire. As well, their study was performed at body temperature [21]. The breakdown potential would be higher if it was performed at room temperature and with a stent instead of a wire. But, the breakdown potential was sufficiently high for even the AS samples to still be impervious to corrosion in a pig based on this study. The AS samples performed worst, in all the corrosion tests, in comparison to the other surface finishes, followed by the 600 grit samples. The hydrogen peroxide treatment had the best corrosion performance in terms of both the breakdown potential and the mass loss data. The only drawback for the hydrogen peroxide treatment was the increase in the nickel concentration, found after the treatment of both the mechanically polished and as received samples. The water treatment applied to the 600 grit samples also eliminated corrosion up to a potential of 1.5V and the titanium to nickel ratio was far greater than the AS and the H_2O_2 treated, plate, samples. But, aggressive corrosion and a high level of mass loss was found after 5 days of immersion in $FeCl_3$. There is a trade off in comparing which of the sample treatments have the best properties for an implant in terms of the biocompatibility and corrosion resistance. For the H_2O_2 samples, there is a higher nickel concentration in the oxide but also a thicker oxide layer. Over many stress cycles this could lead to further cracking which may deteriorate long term corrosion resistance. A study by Shabalovskaya *et al.* held 30% H_2O_2 treated nitinol wires in tension, with a 6% strain

in a 0.9% NaCl electrolyte, for 150 hours and detected no corrosion, but they did not test the effects of cycling on the corrosion performance [45]. On the other hand, the WT 600 grit sample had a poor immersion performance $FeCl_3$ in comparison. The superior performance in general comes from the MP+WT samples. A breakdown potential above 1.5V is well above the 600 mV (SCE) limit found by Sullivan *et al.* for pitting corrosion *in vivo*, therefore there should be no corrosion within 6 months of implantation [21]. As well, the lower concentration of nickel assists biocompatibility and reduces the negative effects on the surrounding cells.

2.5.6 Imaging the Corrosion of Nitinol

Corrosion always initiated at the interface between the nitinol wire and the epoxy connecting it to the Teflon tubing. This initial corrosion is clearly not the result of pitting but instead of crevice corrosion, which initiates from small exposed regions on the edge of the sample. When the wires were treated, prior to polishing with H_2O_2 no corrosion was detected from the edges of the sample or from the center. Nitinol plates were originally used to prevent crevice corrosion initiating from the edges. But, the lack of an interface between wire and epoxy inhibited corrosion to such an extent that no localized corrosion was ever observed, even in highly acidic solutions. Eventually a solution with a low enough pH initiates general corrosion after the dissolution of the oxide layer. This very high corrosion resistance, much higher than most other experiments performed with 1 μm polished nitinol tabulated in section 2.2.8, is reminiscent of the study performed by Bai and Rotermund, in fact our sample had the same surface area [47]. The average surface area for nitinol samples throughout the literature is on the order of 1 cm^2; the ground flat samples in our study had an area of

0.0011 cm^2. Intermetallic and carbide inclusions are known from XPS sputtering studies to be enriched at the oxide substrate interface, as talked about in section 2.2.8. This discrepancy is likely due to the very small surface area that will include few inclusions. Due to exposing a cross section of substrate as the new surface the sample will have a substantially lower inclusion density. Therefore, to image nitinol corrosion without initiating corrosion via crevice corrosion a larger sample should be used. The breakdown potential should fall to more reasonable values even while using a 0.9% NaCl electrolyte. This comes with two drawbacks: either you image only a small area of the surface potentially missing the corrosion entirely or you image the entire sample but with a lower magnification. This would prevent high resolution images of pit initiation and the initial stages of propagation.

While corrosion always initiated from the edge of the sample due to crevice corrosion, pitting corrosion did appear as corrosion fronts propagated. The front did not just expand in a linear fashion but instead, as was shown section 2.3.4, propagated via the formation of small corrosion pits. These small pits formed ahead of the front and grew until they merged with the front. Clearly some regions at the head of the front are more favoured than others, if not continuous corrosion would have occurred, linear front propagation. The same mechanism described in section 2.2.9 for SS, will apply in the case of nitinol. Metal cations and hydrogen ions will diffusive out of the corrosion front into the surrounding regions. The surrounding electrolyte will get progressively more acidic inducing corrosion preferentially near the front. This was found to reduce the thickness of the oxide near the corrosion pit [64]. The clear hemispherical patterns found in front of corrosion pits form due to the weakening of the surrounding oxide. Corrosion pits then weaken the area ahead of these new pits leading to another row of pits forming. These hemispherical fronts present a very clear

structure which is unlikely to be due to the distribution of inclusions. In stainless steel, corrosion pits are distributed close to a few initial pits but still initiate all over the surface. In Nitinol corrosion pits were only found close to fronts. It is unclear why in some cases the initial region of corrosion propagates and envelops the hemispherical fronts ahead of this region and in other cases it does not. In these cases the small pits could be repassivating preventing their growth and the propagation of the initial corrosion front. We were not able to induce corrosion without the use of crevice corrosion. Therefore, our data provides no evidence as to where corrosion would initiate when no crevices were present. As well, we can see no theoretical reason why the detected mode of corrosion propagation would be different if it originated from a corrosion pit rather than from a crevice; however experimental evidence with no crevice present would be beneficial. An interesting application of our imaging system would be to first perform an EDS scan of the surface. This would allow the identification of inclusions in the oxide layer. Then the sample could be imaged while it corroded, and effect of inclusions on the preferred direction and mechanism of corrosion propagation could be determined.

2.6 Conclusion

We found the fine-drawn as received nitinol wires had the worst overall corrosion resistance, but the breakdown potential was still quite high. Removing the original oxide layer leads to a more noble breakdown potential. The water treatment, when applied to the mechanically polished sample, inhibits localized corrosion. The corrosion resistance of the as received and water treated samples eliminated breakdowns in some samples while in others it had no measurable effect. The water

treatment reduced the nickel concentration in the oxide layer by a substantial margin. As well, other studies have shown that water treated nitinol samples leach out substantially less nickel ions than non-treated samples. The hydrogen peroxide treatment increased the corrosion resistance, eliminating all breakdowns. But, the treatment did increase the surface concentration of nickel by a large margin. This would lead to an increased rate of cell death around the implant. From this work the water treatment appears to be the clear favourite when biocompatibility, and not just the corrosion resistance is taken into consideration. We determined that nitinol, in 1.2 M HCl after initiating from a crevice, corrodes via small corrosion pits that form ahead of the initial corroded site in front like pattern. These then expand, merging with the initial site. This process then repeats until the surface repassivates.

Chapter 3: Aluminum Corrosion

3.1 Introduction

3.1.1 Introduction

Aluminum is the second most common metal used in industry today. Aluminum is very malleable and has a low-density. Aluminum alloys are much less malleable than pure aluminum (Al 1100, 99.9% Al with 0.1% Cu), making them much more useful in most industrial applications. Alloying to create a less malleable and higher strength material lowers the corrosion resistance of the material relative to alloys of a higher purity [74]. Aluminum 5052, is composed of 97.2% Al, 2.5% Mg, and Cr 0.35%; it is commonly used in marine applications, because it is known to have excellent corrosion resistance against seawater while maintaining a high strength. The 5XXX series of aluminum is used in marine applications such as in the construction of boat hulls, where it would encounter chlorine rich seawater. In these marine applications the material will experience moving water from tides, currents, and propulsion. Due to the aggressive nature of seawater as an electrolyte, it would be useful to determine the effects of flow on the corrosion of aluminum. There is little experimental evidence in the literature on the effect of relatively low flow velocities on corrosion. We will determine the relative breakdown potentials of aluminum samples, with and without electrolyte flow, using cyclic voltammetry scans to assess the relative corrosion resistances. To the best of our knowledge, the effect of electrolyte flow on the breakdown potential has not been previously investigated. Furthermore, we will image the surface of the aluminum samples, using a light microscope, during the cyclic voltammetry tests. This will provide information about the severity and the mechanism of corrosion, both when the flow is turned on and off.

3.2. Literature Review

3.2.1 Aluminum Corrosion Mechanism

Aluminum is widely known to be susceptible to pitting corrosion in chloride based solutions, in acidic solutions uniform corrosion generally occurs. Reboul *et al.* proposed a 10-step mechanism for the initiation of corrosion pits by chloride ions in aluminum [75]. This mechanism is shown in figure 3.1. They proposed that chlorine ions adsorb onto flawed regions of the metals oxide layer. Many of these flaws are caused by inclusions and various intermetallic particles that disrupt the surrounding oxide layer. This is one of the key reasons why high purity aluminum has a higher corrosion resistance compared to alloys such as Al 5052. During the reaction intermetallic particles and copper inclusions serve as sites for the cathodic reaction. Wang *et al*. found that intermetallic particles located on the surface of aluminum, such as Mg_5Al_8, are anodic relative to the aluminum matrix [76]. These particles acted as initiation sites for pitting corrosion in the Al 5XXX series of alloys [38, 76, 77]. Some intermetallic particles are also known to be cathodic relative to the matrix. The subsequent increase in pH around these inclusions can also destabilize the oxide layer close to the precipitate providing more sites for corrosion initiation [38, 76, 77]. Corrosion pits will form around these particles. Due to the small size and constricted nature of the pit the aggressive electrolyte will not easily be diffusive outside. Similarly, to the mechanism described in section 2.2.3, free metal ions in these pits will react with water molecules creating hydrogen ions thereby lowering the pH. An aluminum chloride complex will form on the bottom of these new pits due to saturation of the pit electrolyte preventing repassivation. These complexes will dissolve, in the metastable pitting regime, and the pit will repassivate as it grows larger, increasing electrolyte exchange with the external solution. Some of these pits will not repassivate

because of a stable $AlCl_3$ layer, that forms on the bottom of the corrosion pit due to supersaturation, that is renewed faster than it dissolves. There is a critical current density below which this repassivation will occur so reducing the electrode potential can lead to repassivation of the stable corrosion pits [78]. An increasing electrode potential, increases the current density around the working electrode and therefore inside of the metastable corrosion pits. The pit will continue to corrode until the current density drops below the critical value and the pit dilutes causing the dissolution of the aluminum chloride layer [75].

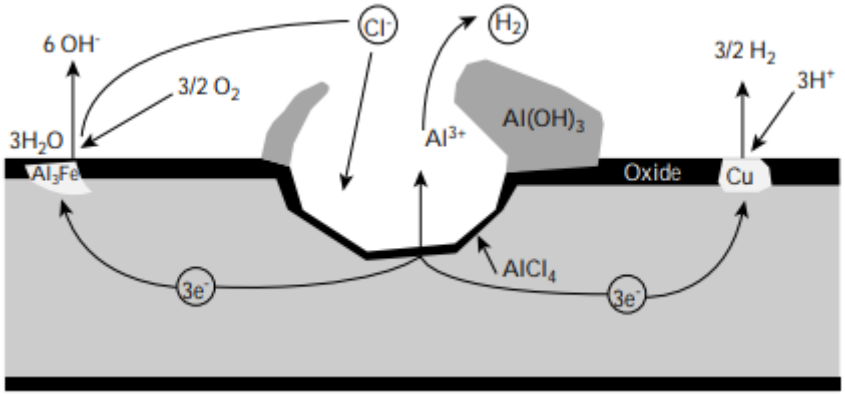

Figure 3.1: This diagram shows the mechanism for pit propagation in aluminum [75].

3.2.2 Spatial Effects of Aluminum Corrosion

Aluminum is known to commonly corrode via one of three mechanisms: filiform, pitting, and general corrosion. Filiform corrosion occurs only when the material is covered by a layer of paint, organic coating, or a thick oxide from anodization [74, 79]. We have none of these prerequisites in this study. Whether pitting corrosion or general corrosion occur depends on the distribution and type of inclusions and intermetallic particles found in the material. As discussed above in section 3.2.1, inclusions are known to be the initiation sites for corrosion. This is made more

complicated by the variety of different aluminum alloys, which contain different inclusions and therefore exhibit different types of corrosion behaviours. In the case of the high strength Al 2XXX series, 3-5% Cu, it is known to undergo severe pitting under certain conditions. Pitting is induced by the Al-Cu-Mg, anodic to the matrix, and Al-Cu-Mn-Fe-Si particles, cathodic to the matrix. Shell shaped inclusions are found throughout Al 2XXX; they have an Al-Cu-Mg exterior and an Al-Cu-Mn-Fe-Si interior, which form a galvanic couple [79]. The oxide around these couples is weakened and cannot re-oxidize inducing the formation of highly localized corrosion. J.H.W. de Wit found that if Al 2024 was quenched <54 s after exposure to air the shells were not large enough for pitting to dominate over general corrosion [79]. Donatus *et al.* compared the corrosion of three separate Al alloys: Al 2024, Al 5083, and Al 6082 [80]. An SEM investigation after the corrosion of Al 2024 found pitting corrosion surrounding cathodic and anodic inclusions, a similar result to other researchers [38, 76, 77, 79]. Al 5083 on the other hand was found to have a substantially different corrosion mechanism. Al 5083 corroded with a filiform-like channelling mechanism, an SEM image of their results is shown in figure 3.2 [80]. Instead of corroding via pitting corrosion, Al 5083 is expressing crystallographic corrosion. Donatus *et al.* said that the corrosion initiated at the grain boundaries which are rich in Al_3Mg_2 inclusions [80]. These Al_3Mg_2 inclusions will preferentially dissolve enabling corrosion to initiate at the grain boundaries. Several researchers have found evidence that in Al 5086 corrosion will propagate along the <100> crystalline direction while bounded by {100} planes [81, 82]. If the channels propagate in any other direction the active surface area would increase with time. This would decrease the current density until the channel repassivates [82].

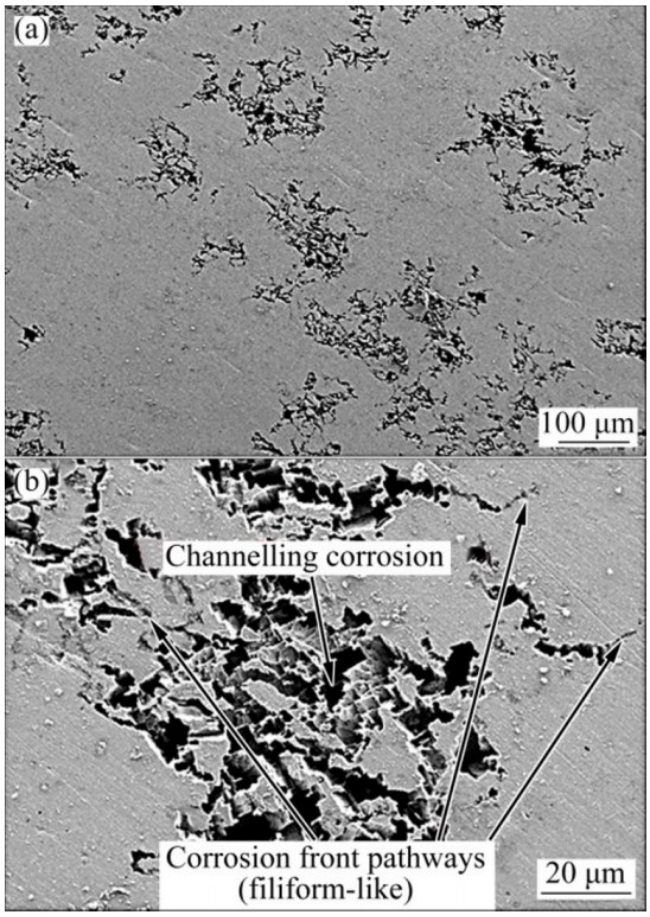

Figure 3.2: An SEM image of a corroded Al 5083 plate from the research of Donatus *et al.* [80].

3.2.3 Effect of Flow on Corrosion

Evgeny *et al.* tested the effects of laminar and turbulent flow on the corrosion of low carbon steel in a 4M HCl solution at 80°C. They used a rotating cylinder electrode (RCE) to create laminar, 5 rpm, and turbulent flow, 6000 rpm, conditions. The researchers found that turbulent flow leads to a larger current density and more severe corrosion of rough samples, 120 grit. But, the different flow regimes had little effect on the corrosion rates when smooth, 1200 grit, samples were tested. This study did not test samples in still solutions [83]. P.V. Scheers studied the effect of the flow velocity on the corrosion rate of mild steel in synthetic mineral water. He used both an

RCE electrode and a pipe system to determine the corrosion rates of the material. Scheers found that the corrosion rate linearly increases with the flow rate for both the RCE and pipe tests; the flow rate was varied between 0.25 m/s and 3.5 m/s. This linear increase held in neutral and basic solution; in acidic solutions the corrosion rate increased logarithmically with the flow rate [84]. Researchers have shown that, depending on the material, a stagnant solution can lead to severe corrosion. In SS 316 the average pit depth was measured after exposure to seawater for 13 months. Samples in seawater moving at 1.5 m/s had an average pit depth of 0.10 mm while samples in stagnant seawater were found to have pits 1.89 mm deep on average. There was a substantial increase in the number of pits when the sample was left in stagnant seawater [85]. A study by Wight and Godard confirmed the same trend in Al 1100 that was found in SS316. They varied the flow rate between .005 m/s and .05 m/s and measured the density and depth of the resulting corrosion pits. The samples were immersed for 1 week at room temperature. They found that the density of corrosion pits and the average depth decreased as you increased the flow rate until no corrosion was detected at a flow speed of 0.05 m/s [86]. The United States Navy commissioned a study to investigate the effect of highly turbulent flows on the corrosion of aluminum. The study found that the corrosion rate increased exponentially as the velocity of the seawater was increased from 3 m/s to 30 m/s in both Al 1100 and Al 5456 [87]. The literature on the effect of flow rate on corrosion suggests a general trend of an increasing corrosion rate with increasing flow velocity. But, several reports suggest that flow rates with a low velocity can inhibit corrosion instead of inducing it.

3.3. Materials and Methods

3.3.1 Wire Flow Experiment

The corrosion cell to test wires under flow was built out of a 2-ft long PVC pipe, 1.27 cm inner diameter. The pipe had threaded ends allowing the attachment of stainless steel 316 barbed pipe-tube connectors. Three 2 mm diameter holes were drilled in the top of the tube for the electrodes. The hole for the working electrode was placed 1 cm towards the inflow end of the tube. This was to prevent the reference and counter electrodes from disrupting the flow prior to hitting the working electrode. These two electrodes were placed 1 cm behind the working electrode towards the out-flow end. A miniature Ag/AgCl electrode (eDAQ, model ET073) and a 2 cm long platinum wire was used as the reference and counter electrodes respectively. Al 1100 wires (McMaster Carr) were used for this experiment as the working electrode. The tip of the wire was coated with epoxy to prevent corrosion at the rough cut end. In total a 1 cm long aluminum wire was exposed to the electrolyte. Above the exposed section of the wire, heat shrink tubing was shrunk onto the wire and the open end epoxied to prevent crevice corrosion at the tube-wire interface. After sample preparation the wires were sonicated in acetone and then ethanol for 15 minutes and dried with a heat gun. The electrode junction with the pipe was made watertight with silicone glue.

To propel the electrolyte a VicTsing 920 gallon per hour submersible pump was used. This pump was placed in a beaker filled with 2.5 L of .154 M NaCl, 0.9%, solution (ACP 99% ACS reagent). The pump in the reservoir beaker was at approximately the same height as the sample to eliminate any effect of different gravitational potential energies on the flow speed. The pump was run until a steady state temperature was reached, 35°C, before an experiment was initiated. Before and

after an experiment the pump was rinsed with distilled water and then run in a reservoir of distilled water to eliminate any contaminants from previous experiments. Due to the pumps plastic construction and since it has internal parts it could not be dried with a heat gun. Instead, it was wiped off and then allowed to air dry. The flow rate at the working electrode for this specific cell and pump was calculated to be 8.4 m/s. The experimental set up is shown in figure 3.3.

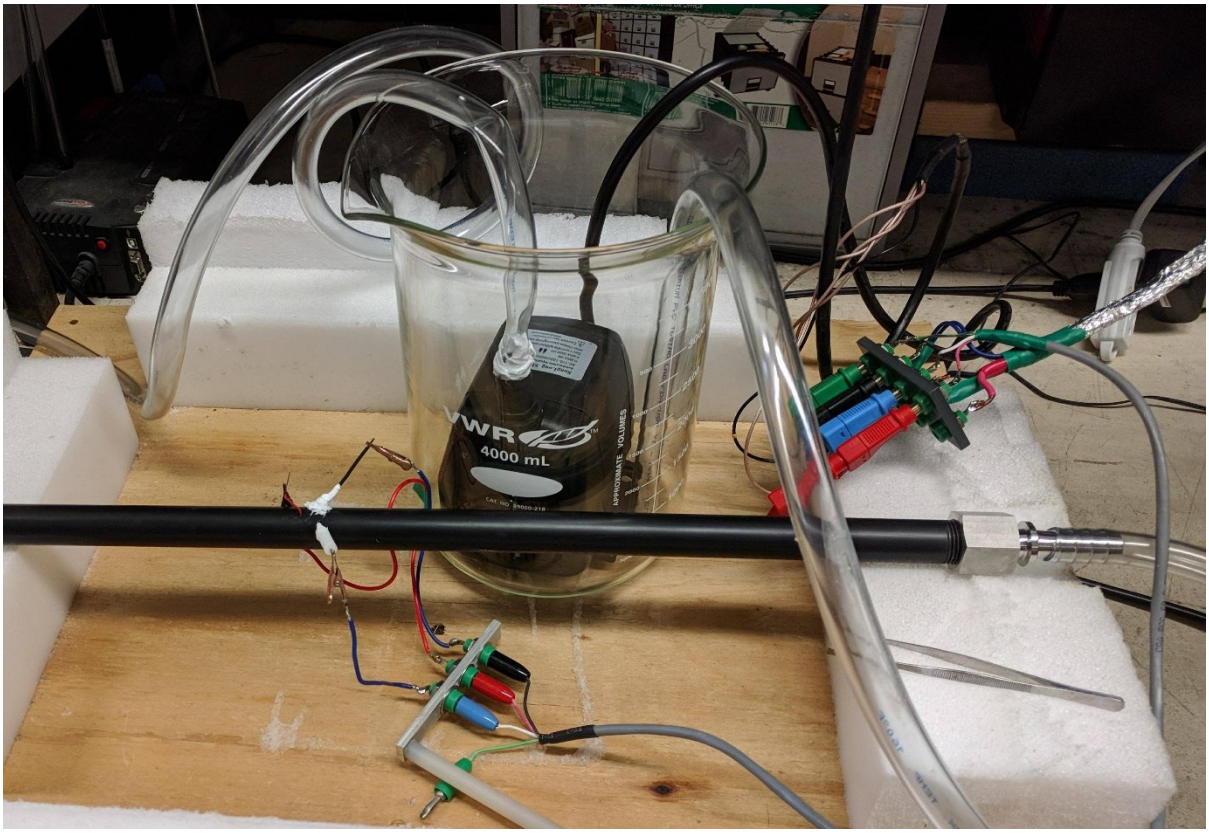

Figure 3.3: The wire flow cell set up. The three electrodes are found in the center of the tube: red wire connects to the working electrode, blue wire connects to the reference electrode, and black wire connects to the counter electrode.

The breakdown potential of the wire when the pump was both on and off was tested using an Autolab PGSTAT 2014 potentiostat. The open circuit potential was allowed to stabilize for 30 minutes, after the steady state temperature was reached, prior

to the experiment. The idle solution tests were carried out in the same cell but with pump only turned on long enough to fill the tube. The cyclic voltammetry scan was started with a potential 100 mV below the open circuit potential. The potential was increased at a rate of 0.1 mV/s until a current density of .03 A/cm^2 was reached. The potential was then reversed until the initial potential was reached again.

3.3.2 Plate Flow Experiment

The corrosion of polished Al 5052 plates was also tested using potentiodynamic scans. Plates allowed imaging of the sample surface during corrosion testing. The samples were polished to create a smoother surface which enabled us to resolve small structures on the surface. The plates were mounted onto aluminum pucks with crystal bond adhesive prior to polishing. First the native oxide layer was removed with a 1500 grit silicon carbide pad (Buehler) at 100 rpm. Following this step, the samples were cleaned and polished with 9 μm, 3 μm, and 1 μm diamond suspensions respectively. Between each step the samples were washed with distilled water to prevent any cross contamination of the TexMet cloth polishing pads (Buehler). The samples were sonicated in acetone and then ethanol for 15 minutes after polishing and then dried with a heat gun. To create an electrical contact with the sample a copper wire was soldered onto a piece of copper conductive tape. This was stuck onto the back of the polished sample. The copper wire was covered with heat shrink tubing to prevent the corrosion of non-aluminum areas. The samples were then coated with a lacquer to prevent corrosion of non-imaged areas of the material. This exposed surface area was on the order of .002 cm^2 but varied due to human error.

A special electrochemical cell was designed and produced for this experiment allowing both electrolyte flow and in situ imaging. Figure 3.4 shows the cell schematic, the flat piece of glass, 44 mm long, at the front of the cuvette allowed the imaging of the sample using the optical microscope. The glass was bent in a trapezoidal shape to allow another imaging set up, ellipsomicroscopy for surface imaging (EMSI), to be used. A laser beam perpendicular to the 63 mm angled, 124°, piece of glass would hit the sample surface at the Brewster angle, 56°. A teflon sample, 1x1x.5 cm, holder was placed in the center of the cuvette. A line was cut through the center of the sample to hold the metal samples in place. The samples were glued into the sample holder with silicone glue. A PVC cover had a hole cut into it which allowed the electrode connected to the sample to pass through it. In an experiment this cover was glued into place and the electrode glued to the cover to make a water tight seal. The cover is shown in figure 3.5. The reference electrode and the counter electrode, a platinum plate attached to a platinum wire, as seen in figure 3.5 are glued into place on the left and the right hand side of the cover. A tube was also attached to the top of the cuvette; this allowed air bubbles to escape from the cuvette when the pump was initially turned on. After the trapped air was released the tube was sealed with a clamp.

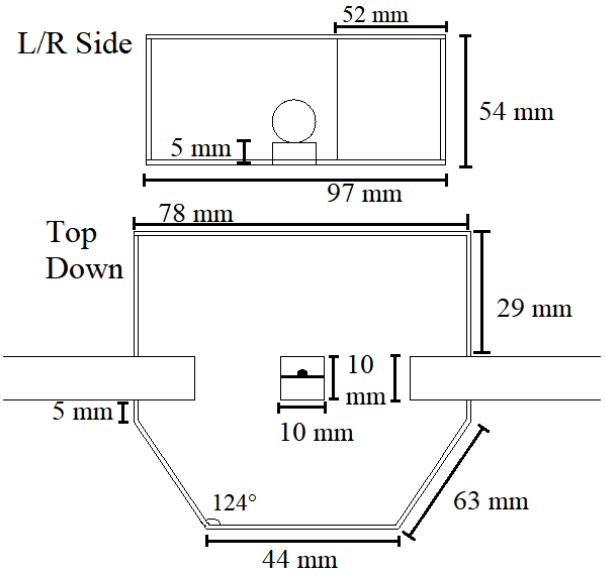

Figure 3.4 The schematic of the corrosion cell. The top image shows the side view of the cuvette. The bottom image shows the cuvette from the top down with the top removed.

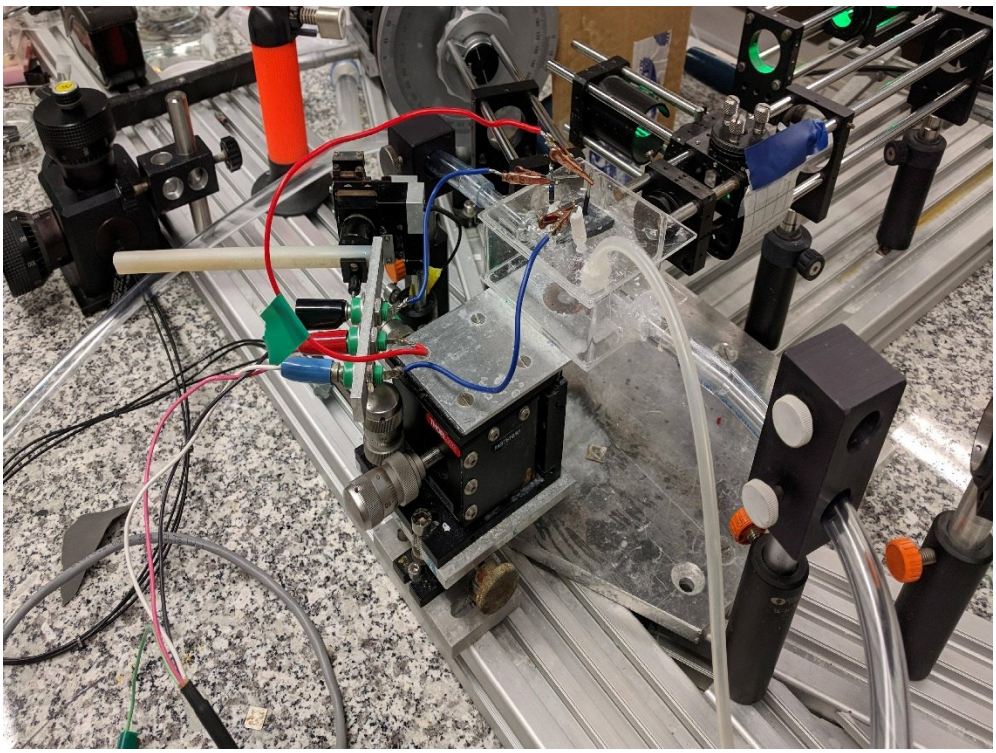

Figure 3.5: An image of an aluminum sample mounted in the cuvette. Note the PVC cover, grey glued into a cut out in the cuvette lid.

These samples were tested in 2.5 L of 0.154 M, 0.9%, NaCl solution (ACP 99% ACS reagent). The electrolyte was pumped through the sample by a VicTsing 400 gallon per hour submersible pump. Similarly, to the wire experiment the pump and reservoir were held at the same height as the aluminum sample. This pump did not change the temperature of the reservoir by more than one degree. The samples were tested with both the pump turned on and turned off. When the pump was turned on there was a flow rate of 0.2 m/s at the sample surface. A miniature Ag/AgCl electrode (eDAQ, model ET073) was used as the reference and a platinum plate suspended by a platinum wire was used as the counter electrode. The same cyclic voltammetry experiment was performed as the experiment with the aluminum wire samples. The image of the sample surface was recorded during each of these experiments, the same imaging set up was used as the one described in section 2.3.5. As well, in another experiment a light was shone on the CCD camera and the flow was subsequently turned on and off. During this a video was taken, the flashing light allowed the determination of when the flow was turned off and on.

3.4 Results

3.4.1 Electrochemical Results

The results for the electrochemical data are tabulated in table 3.1. There was a significant difference (t-test with a 95% confidence interval) between the 1 μm Al 5052 samples with the pump turned on and off. The samples tested when the pump was turned on had a more positive breakdown potential. There was no significant difference between the Al 1100 wires tested with and without electrolyte flow. It is important to keep in mind that the temperature was increased by approximately 15 °C when the flow

rate was turned on. The corrosion potential was significantly lower for the 1 um Al 5052 samples in comparison to the Al 1100 wires. A plot of typical cyclic voltammetry experiments for the Al 5052 and Al 1100 samples are shown in figures 3.6 and 3.7. When comparing the current density between each sample the samples tested with electrolyte flow appear to have a higher current prior to breakdown. This was observed across both the Al 5052 and Al 1100 samples. Other than this fact the shape of the curves was very similar between both the experiments with the flow on and off.

Table 3.1: The summary of the data for the flow experiment. The flow rate, breakdown potential, repassivation potential and the corrosion potential is listed. These potentials are reported against the RCE reference electrode.

Material	Flow Rate (m/s)	Eb (mV)	Ep (mV)	Ecorr (mV)	No. Samples
Al 5052, 1um	0.2	-635 (12)	-716 (8)	-700 (34)	9
Al 5052, 1um	0.0	-727 (8)	-689 (10)	-750 (10)	6
Al 1100, wire (35°C)	8.4	-735 (5)	-765 (4)	-944 (24)	8
Al 1100, wire	0	-730 (5)	-761 (5)	-993 (27)	7

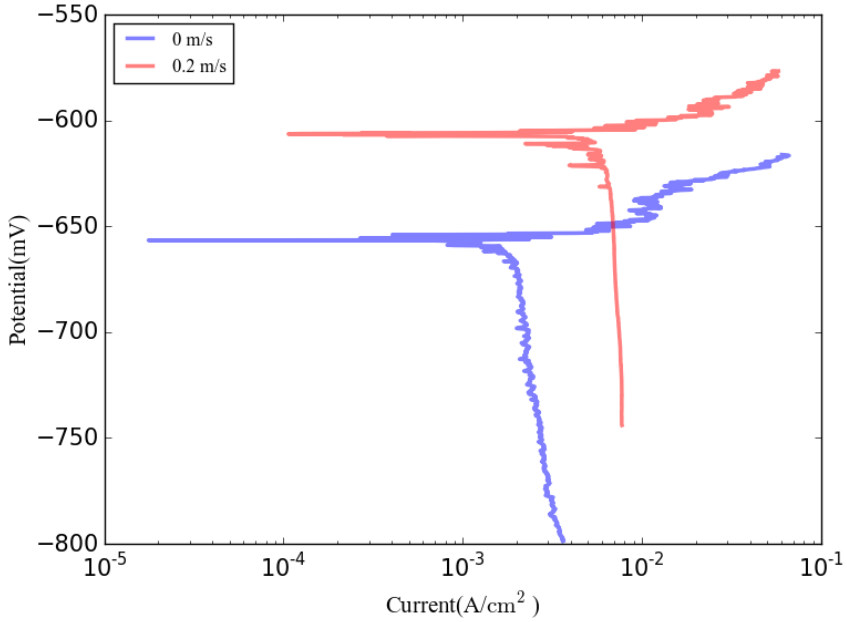

Figure 3.6: A cyclic voltammetry plot of two 1 µm Al 5052 samples under the no flow and 0.2 m/s conditions.

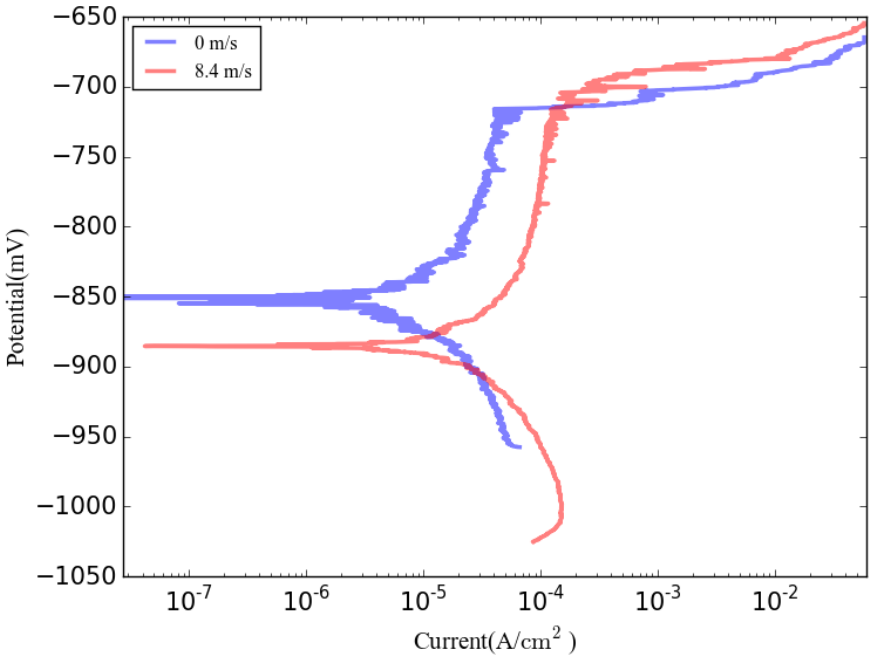

Figure 3.7: A cyclic voltammetry plot of two 1 µm Al 1100 samples under the no flow and 8.4 m/s conditions.

3.4.2 Imaging Results

To further test the effects of the flow rate on corrosion we turned the pump on and off while a video was taken, this was conducted at the open circuit potential. The results from one trial of a 1 µm Al 5052 sample is shown in figure 3.8. Prior to corrosion testing, the potential was allowed to stabilize for thirty minutes during which corrosion did occur, albeit very slowly, on the sample. This is the origin of the corrosion that is seen at the beginning of the experiment. When the pump was turned off hydrogen bubbles formed very quickly on the sample surface. The size and number of the bubbles grew the longer the pump was turned off. But, when the pump was turned on all bubbles were either dislodged from the surface or shrunk until they could not be resolved by the video. No more corrosion was detected on the sample surface while the flow was

turned on. When the pump was turned back on again the bubbles slowly started to reappear and to grow in size indicating a resumption of corrosion.

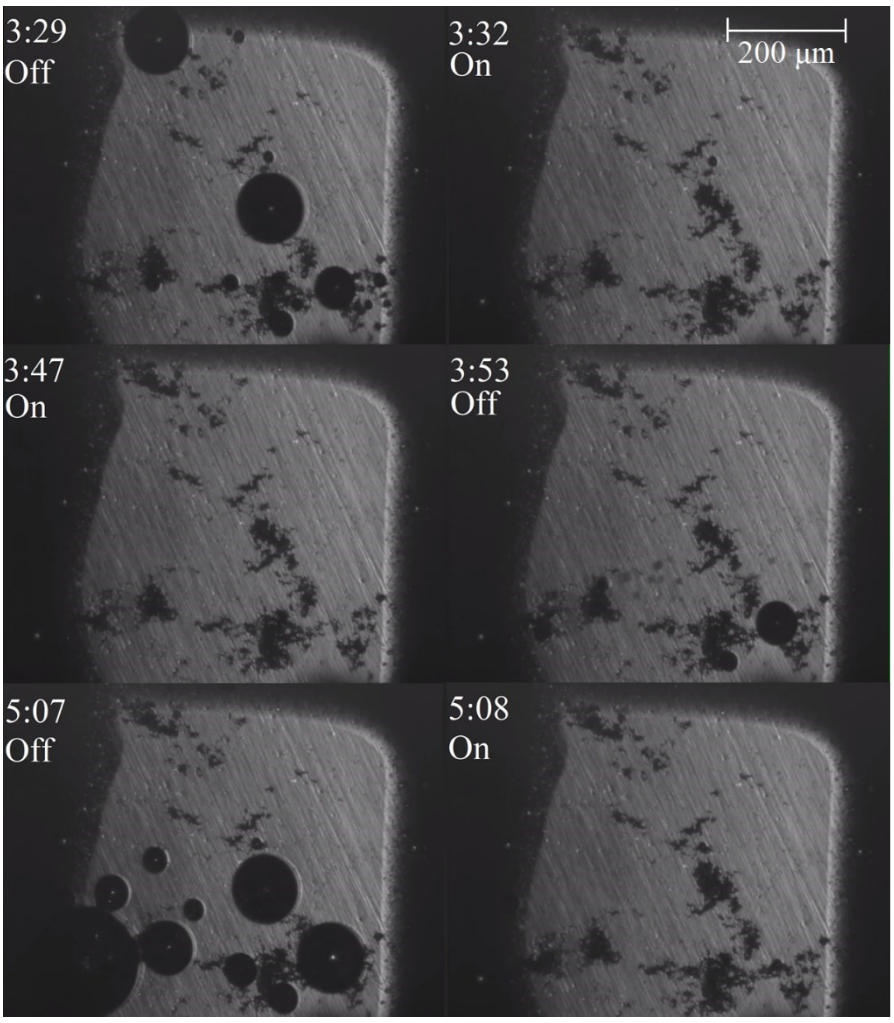

Figure 3.8: Images of a 1 μm Al 5052 sample taken at different times with the pump on and off. The top images show the sample surface when the pump is on and then 3 seconds later turned on. Similarly, the middle and bottom pictures show the sample with the pump on and off and off and then on respectively. The stamps time are given in units of minutes:seconds.

Unlike nitinol, aluminum readily corrodes at the open circuit potential in a 0.9% NaCl solution. Corrosion did not originate at the epoxy-metal interface indicating the corrosion in the videos was not due to crevice corrosion, precursors sites of corrosion are shown in figure 3.8. Images taken during corrosion trials are shown in figures 3.9,

3.10, 3.11, and 3.12. Figure 3.9 shows corrosion when the pump is turned on. The bubbles on the surface remain small unlike when the pump is off. Corrosion initiates simultaneously in two separate regions and spreads relatively radially out from there, the initial site to the right initiated near but not at the lacquer interface. Very similar features can be seen in figure 3.10 where the pump was also activated. We observed no preferential corrosion in the direction of the flow, which was towards the right, in any of these samples. The pump was shut off for the trial shown in figures 3.12. The bubble formation is more rapid in this case and the bubbles grow to a larger diameter.

Aluminum corrosion propagates by thin lines of corrosion that branch off areas already corroding. Further branches break off from the branch propagating away from the initial region, this can be clearly seen in figure 3.11. A similar branching propagation method can be seen in figures 3.9 and 3.12 when look at the furthest edge of the corrosion fronts. Corrosion eventually fills in the area around the new branches. While corrosion propagates with these thin branches the overall propagation extends out relatively radially from the initiation sites, this can be seen in figure 3.9. The presence of moving electrolyte does not alter the corrosion mechanism. Instead the only significant difference observed was a larger rate of hydrogen bubble formation and the larger size of the bubbles when the pump was shut down. The larger rate of bubble formation indicates a higher corrosion rate. Lower breakdown potentials under still conditions further supports this claim. A moving electrolyte will impede the formation of larger hydrogen bubbles; this should explain the absence of large bubbles when flow is inactivated.

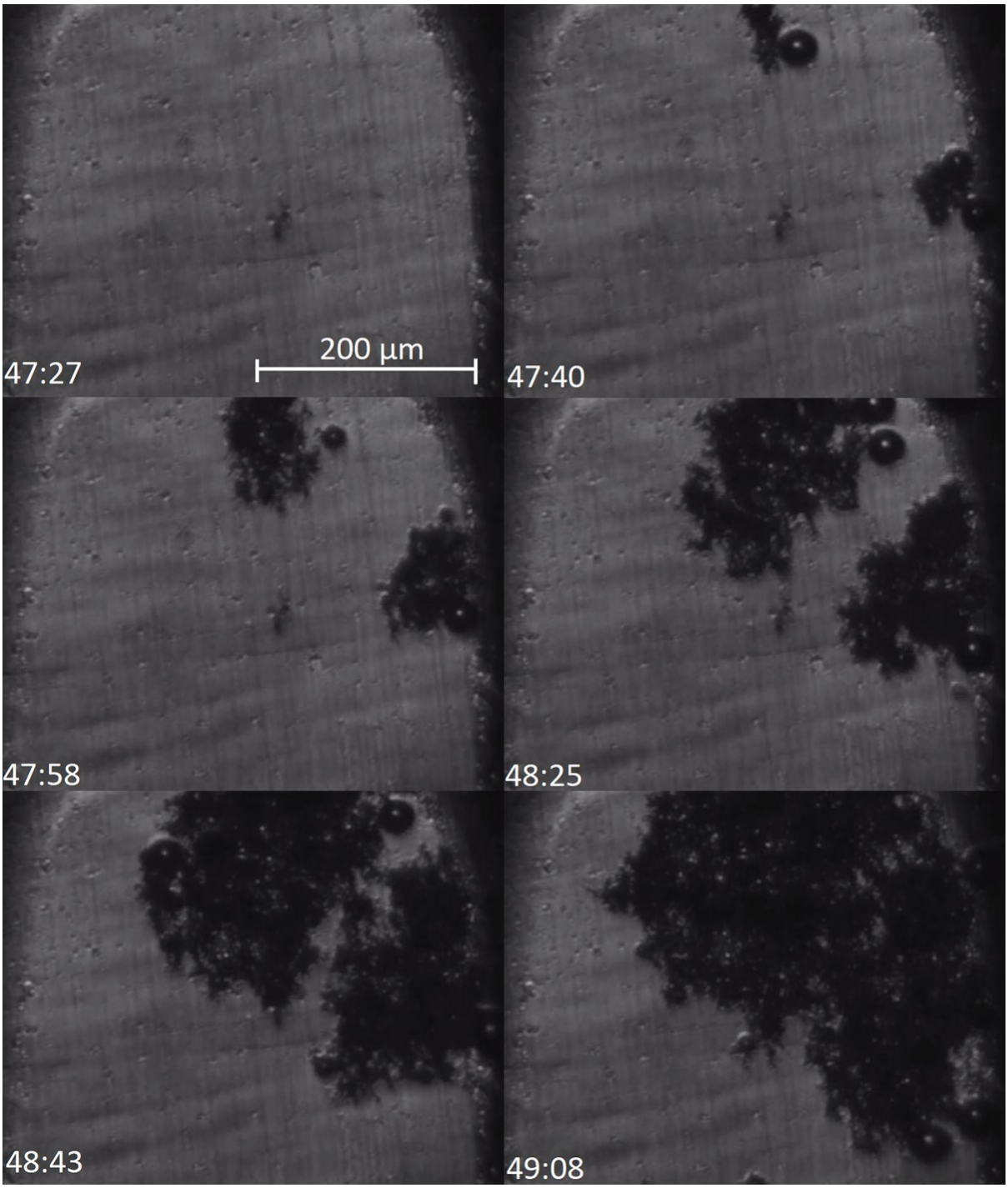

Figure 3.9 Images of the corrosion of a 1 µm Al 5052 sample with flow activated. The stamps time are given in units of minutes:seconds.

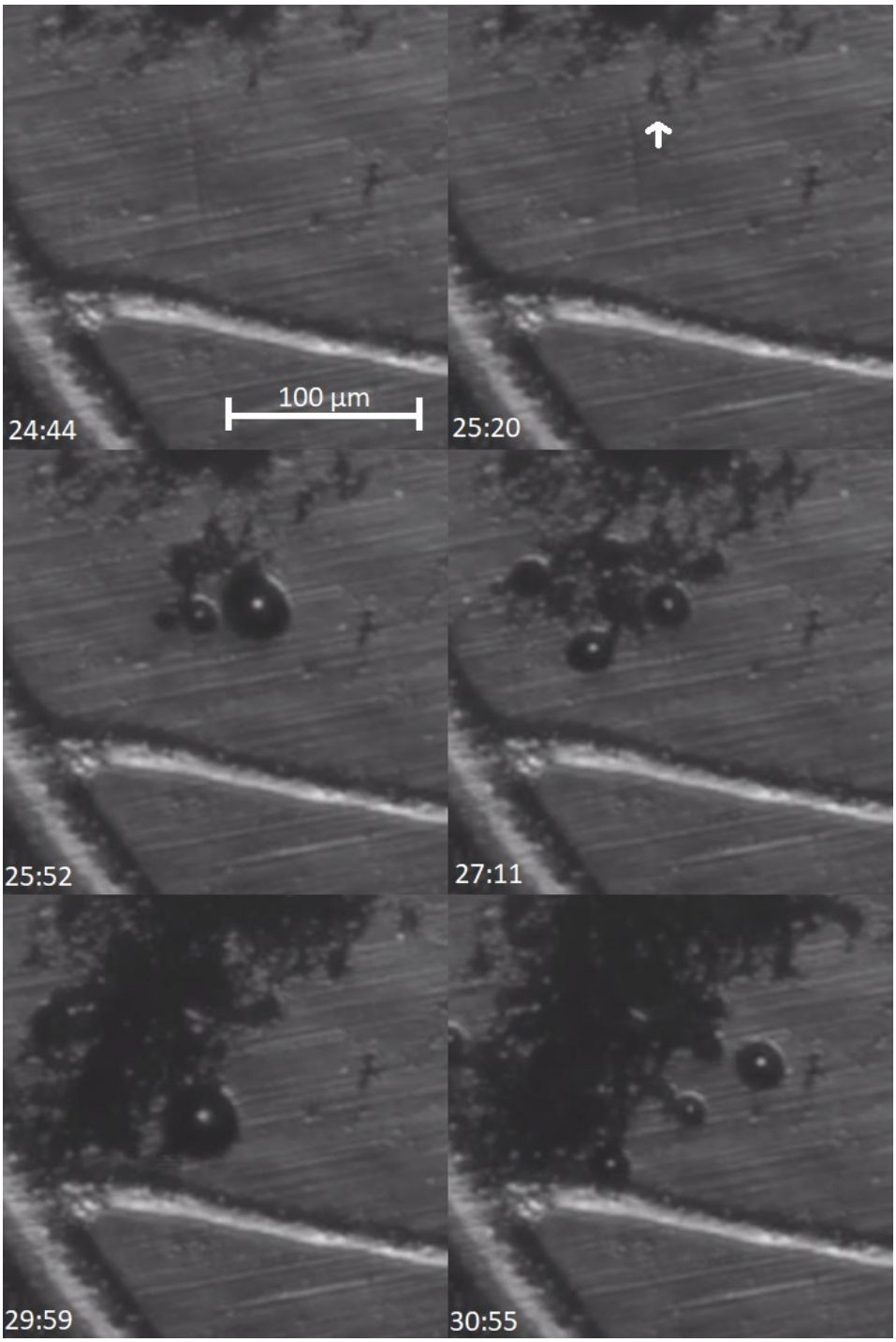

Figure 3.10 Images of the corrosion of a 1 µm Al 5052 sample with flow activated. The arrow indicates the original location of corrosion propagation. The stamps time are given in units of minutes:seconds.

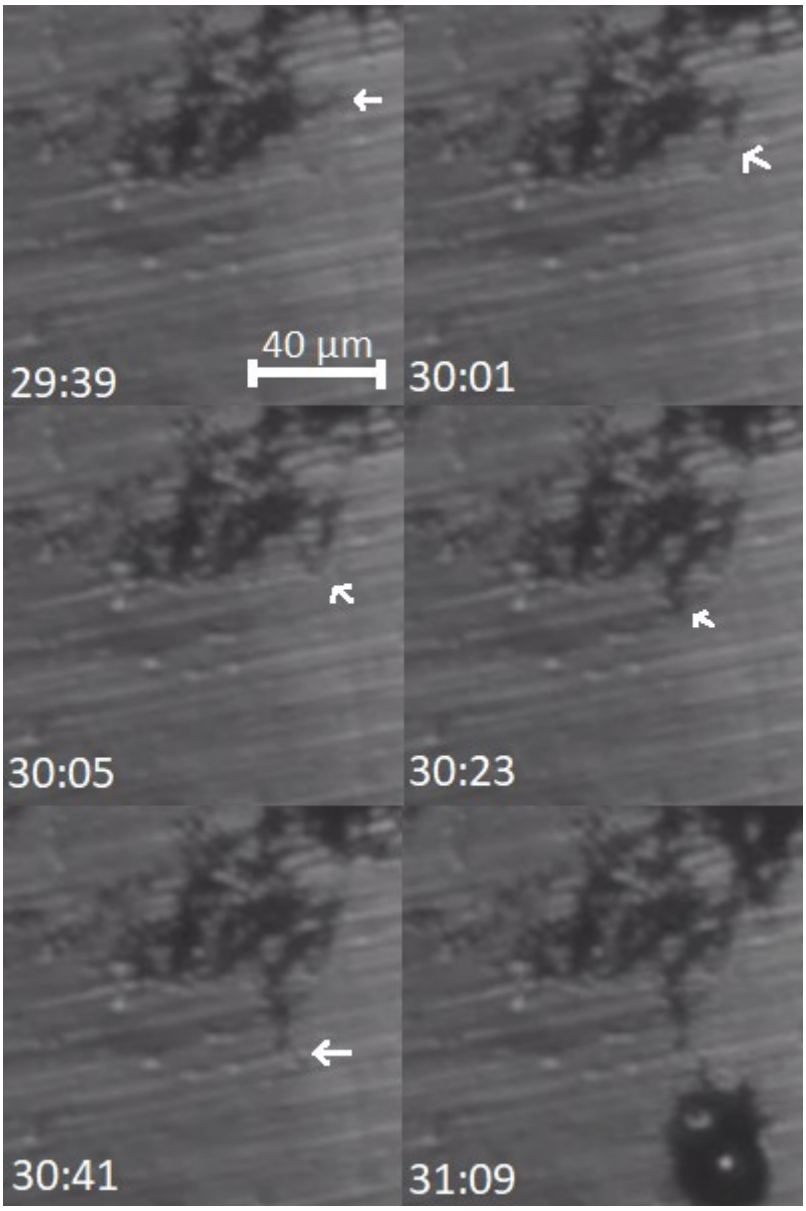

Figure 3.11 Images of the corrosion of a 1 µm Al 5052 sample with flow activated. This sample is the same as the one shown in figure 3.10. The arrows indicate the next stage in corrosion propagation. The stamps time are given in units of minutes:seconds.

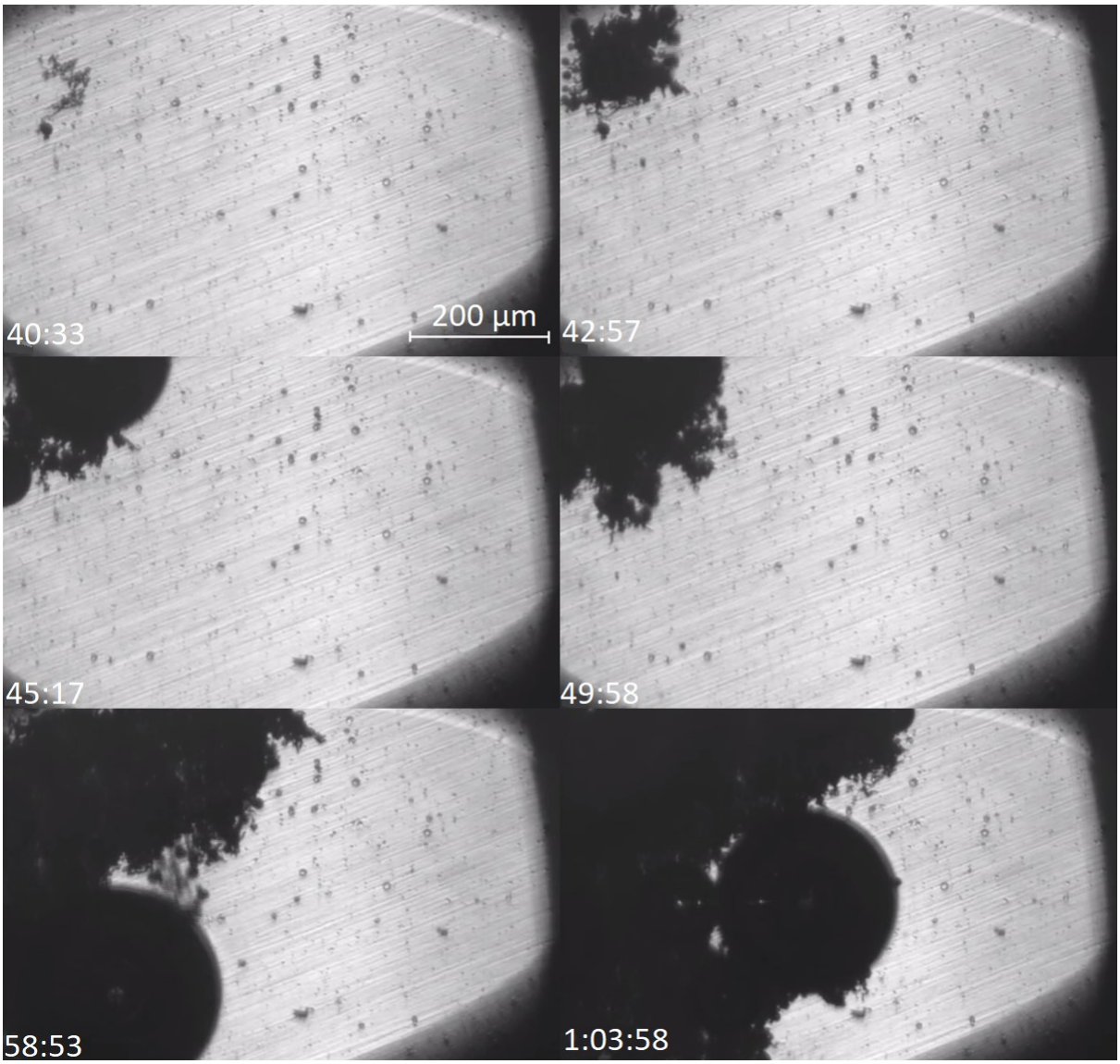

Figure 3.12 Images of the corrosion of a 1 µm Al 5052 sample with flow disactivated. The stamps time are given in units of minutes:seconds.

3.5 Discussion

3.5.1 Corrosion of Aluminum

Differential concentrations of oxygen give rise to localized corrosion in a constrained space where oxygen is consumed and cannot be replenished fast enough. As well, a limited supply of oxygen inhibits the repassivation of the oxide layer in a corrosion pit. Electrolyte movement will augment oxygen diffusion into crevices and

pits thereby making those corrosion hotspots less anodic and allow repassivation. Furthermore, the flow of electrolyte will tend to make conditions more uniform on the surface of the material. Corrosion pits and crevices have an aggressive internal electrolyte and therefore flow will increase diffusion out of the pit and dilute the internal electrolyte reducing the current density inside of the corrosion pit. This allows easier repassivation of corrosion hotspots. These velocity dependent effects can all lead to a reduction in the severity of corrosion [85]. At higher flow velocities turbulence can promote non-uniform conditions such as differential chlorine and oxygen concentrations on the sample surface. In simulations by Organ *et al.* they looked at the effect of stirring on the distribution of corrosion pits. The simulation predicted that the corrosion pits are distributed close together in the region of highest turbulence [88].

Interestingly the Al 5052 plates and Al 1100 wires both had the same breakdown potential in the stagnant case. You would expect Al 1100 to have a larger breakdown potential since it is generally held to be more corrosion resistant. But, since Al 1100 wires and Al 5052 plates had different surface finishes no conclusions can be taken from the indistinguishable breakdown potential. In the case of Al 5052 plates there was a significant increase in the breakdown potential when the pump was turned on, while in the case of the Al 1100 wires there was no significant difference when the pump was turned on. But, the pump increased the temperature of the electrolyte from room temperature to 35°C. A lower breakdown potential is correlated with a poor long-term corrosion resistance. Therefore, Al 5052 kept in a stagnant solution will experience more severe corrosion than a sample in a slowly moving solution. This finding is consistent with the research done by Copson [85] and by Wight and Godard [86]. These researchers found that the density and depth of corrosion pits decreased when the samples were held in a moving solution of electrolyte. These experimental

results have been augmented by our own results where the breakdown potential was found to depend on the flow rate. The temperature increase due to the pump obscures the effect of the faster flow rate on the corrosion of Al 1100. An increasing temperature decreases the breakdown potential of passive metals; corrosion is more severe when exposed to higher temperatures [8]. If only the temperature were increased we would expect the breakdown potential to decrease. The effect of the flow rate must have been to increase the breakdown potential to counteract the effect of the decreasing temperature. We cannot say quantitively what the effect of the faster flow rate is but qualitatively it must be reducing the severity of corrosion relative to still conditions. This seems to contradict the results of both Scheer [84] and Gehring [87]; they found that the corrosion rate increases with the flow rate. First it is important to note that we did not directly measure the corrosion rate but instead measured the breakdown potential as a stand in. Gehring did not measure the corrosion rate for stagnant samples. We are comparing the stagnant to the non-stagnant case while Gehring is comparing between different velocities. It is unclear from our results if the 8.4 m/s case is more severe than the 0.2 m/s case. To test Gehring's results we would need to use aluminum samples with the same surface finish and expose them to increasing flow rates at a constant temperature. We can currently say that relative to the stagnant case salt water flowing with a velocity up to 8.4 m/s will decrease the severity of corrosion in aluminum.

3.5.2 Imaging the Corrosion of Aluminum

The video results corroborate the findings that aluminum in stagnant salt water suffers from more severe corrosion compared to flowing water. When the pump was

shut off hydrogen bubbles rapidly start forming on the surface of the sample. Hydrogen gas forms due to corrosion and is present whenever corrosion is ongoing. Similarly, when the pump is turned on the bubbles immediately decrease in size and disappear. A reduction in the number of hydrogen bubbles should be an indicator of a reduction in the severity of corrosion. You could argue that this difference is due dislodgement of the bubbles from the sample surface and flow inhibiting bubble aggregation. But, the increased breakdown potential corresponds to a reduced severity of corrosion which is corroborated with the production of fewer hydrogen bubbles.

The corrosion of aluminum is substantially different from both the corrosion of nitinol and stainless steel. As described in chapter 1, nitinol corrosion propagates via small corrosion pits that follow in front of a larger corrosion front. Stainless steel on the other hand, does not illustrate corrosion via a large front. Instead, single pits form across the surface. While pits will be preferentially distributed around the initial site of corrosion they do not form a continuous, nitinol, or semi-continuous, aluminum, corrosion front [63]. The corrosion of our Al 5052 plates clearly does not have the same corrosion mechanism as Al 2024 [80]. We do not see any single pits dispersed across the sample forming around inclusions. Instead the corrosion we captured closely resembles the channel corrosion found by Donatus *et al.* for Al 5086 [80]. This is unsurprising since we are testing a very similar alloy of aluminum, Al 5052. Donatus *et al.* performed potentiodynamic tests in still solutions to corrode their Al samples but they did not provide the potential range at which the test was conducted. Different sweep rates and potential ranges would account for the much greater degree of corrosion found on our samples. During corrosion aggressive electrolytes diffuses away from the corroding regions. But, when flow is applied the electrolyte will not uniformly diffuse around the pit. We believed because of this there would have been

preferential corrosion along the direction of flow. But, there was no difference, that we could optically resolve, in the direction of corrosion propagation between the samples tested in the still and flowing solutions. The difference may be to small to be resolved with our microscope in this case. In both cases, corrosion expanded out relatively radially from the sites of corrosion initiation. This may be due to the relatively low flow velocity; but, we did register significant differences in the breakdown potential even with a low velocity. It could be that after passing the breakdown potential the critical current density can be reached in region surrounding the corrosion initiation site even with a less aggressive analyte, due to diffusion facilitated by flow.

This phenomenon should be investigated further using potentiostatic tests, instead of potentiodynamic, so meaningful corrosion propagation speeds can be calculated in the direction with and against the flow. As well, it would be interesting to test if at higher flow velocities corrosion propagates preferentially, in one, direction in Al 5083 samples. If there are indeed changes in the preferred direction of propagation, then the experiment could be expanded to include other alloys such as the Al series 2XXX where pitting corrosion usually dominates as the main mode of corrosion. This could provide more information on the evolution of corrosion under flow like conditions that Al 5XXX series of alloys operate in. Another interesting future project could be to scan a similar sized surface of an aluminum alloy with energy dispersive x-ray spectroscopy (EDS) to create an elemental map of the surface before and after corrosion. Combined with surface imaging, you could determine what role inclusions play in the propagation of corrosion away from the initial sites.

3.6 Conclusion

We have found that corrosion is more severe in stagnant solutions and is reduced when a 0.2 m/s flow is turned on. When a much larger flow rate, 8.4 m/s, is activated we found that corrosion did not become more severe relative to the stagnant case. Our findings are consistent with the results of both Copson [85] and by Wight and Godard [86]. But, our study was the first within our knowledge that determined the effects of the flow rate on the breakdown potential. These results were corroborated by our videos of the surface when the pump was turned on and off. Hydrogen bubbles which are indicative of corrosion increase rapidly in number when the pump is shut off and decrease rapidly when it is turned on. For the time when cathodic potential fails aluminum parts should not be kept in solutions of stagnant water and be designed to reduce regions where the solution would remain stagnant. We found the mechanism for Al 5083 corrosion is not via pitting corrosion but instead through channelling corrosion.

Chapter 4: Conclusion

In chapter 2, we found that AS nitinol wires has worse corrosion resistance in comparison to G600 wires. AS+H_2O_2 and G600+WT wires were found to have a very high breakdown potential in comparison to the AS+WT wires which corroded at the same potential as the AS wires. The AS+H_2O_2 wires were found to perform the best in the mass loss tests but also had a relatively high surface nickel concentration.

In chapter 3, we found that the corrosion of aluminum is more severe in stagnant solutions compared to solutions with electrolyte flow. From this study we recommend that aluminum parts are designed to minimize regions where stagnant solutions may be found. We did not find that the corrosion mechanism changes when the flow is shut on and off but this warrants further investigation with larger flow rates.

Works Cited

[1] G. B. Kauffman and I. Mayo, "The Story of Nitinol, The Serendipitous Discovery of the Memory Metal and Its Applications," *TCE,* vol. 1, no. 2, pp. 1-21, 1996.

[2] K. Otsuka and X. Ren, "Physical metallurgy of Ti–Ni-based shape memory alloys," *Prog. Mater. Sci,* vol. 50, no. 1, pp. 511-678, 2005.

[3] L. Petrini and F. Migliavacca, "Biomedical Applications of Shape Memory Alloys," *J. Metall.,* vol. 3, pp. 1-15, 2011.

[4] N.B. Morgan, "Medical shape memory alloy applications-the market and its products," *Mater. Sci. Eng. A,* vol. 378, no. 1, pp. 16-23, 2004.

[5] K. Otsuka and C. M. Wayman, Shape Memory Materials, Cambridge: Cambridge University Press, 1998.

[6] D. O. Halwani, P. G. Anderson, J. E. Lemons, W. D. Jordan, A. S. Anayiotos and B. C. Brott, "In-vivo Corrosion and Local Release of Metallic Ions from Vascular Stents into Surrounding Tissue," *J INVASIVE CARDIOL,* vol. 22, no. 1, pp. 528-535, 2010.

[7] G.S. Frankel, "Fundamentals of Corrosion Kinetics," in *Active Protection Coatings*, New York, Springer, 2016, pp. 17-32.

[8] E. McCafferty, "Crevice and Pitting Corrosion," in *Introduction to Corrosion Science*, New York, Springer, 2010, pp. 263-311.

[9] D.D. Macdonald, "The point-defect model for the passive state," *J. Electrochem. Soc.,* vol. 139, no. 12, pp. 3434-3449, 1992.

[10] W. Khalil, S. Haupt and H. Strehblow, "The thinning of the passive layer of iron by halides," *Werkstoffe u. Korros.,* vol. 36, no. 1, pp. 16-21, 1985.

[11] N. Sato, "Theory for breakdown of anodic films on metals," *Electrochim. Acta.,* vol. 16, no. 10, pp. 1683-1692, 1971.

[12] S. Yu, W. E. O'Grady, D. E. Ramaker and P. M. Natishan, "Chloride ingress into aluminum prior to pitting corrosion - An investigation by XANES and XPS," *J. Electrochem. Soc.,* vol. 147, no. 8, pp. 2952-2958, 2000.

[13] P. C. Pistorius and G. T. Burnstein, "Metastable pitting corrosion of stainless steel and the transition to stability," *Philos. Trans. Royal Soc. A,* vol. 341, no. 1, pp. 531-559, 1992.

[14] W. M. Huang, Z. Ding, C. C. Wang, J. Wei, Y. Zhai and H. Purnawali, "Shape memory materials," *Mater. Today,* vol. 13, no. 8, pp. 54-61, 2010.

[15] R. Rokicki, T. Hryniewicz, C. Pulletikurthi, K. Rokosz and N. Munroe, "Towards a Better Corrosion Resistance and Biocompatibility Improvement of Nitinol Medical Devices," *J. Mater. Eng. Perform,* vol. 24, pp. 1634-1640, 2015.

[16] D. Stoeckel and W. Yu, "Superelastic NiTi Wire," *Wire J Int,* pp. 45-50, 1991.

[17] C. Heintz, G. Riepe, L. Birken, E. Kaiser, M. Morlock, G. Delling and H. Imig, "Corroded nitinol wires in explanted aortic endografts: an important mechanism of failure?," *J Endovasc Ther,* vol. 8, no. 3, pp. 248-253, 2001.

[18] G. Riepe, C. Heintz, E. Kaiser, N. Chakfe, M. Morlock, M. Delling and H. Imig, "What can we learn from explanted endovascular devices?," *Eur J Vasc Endovasc Surq,* vol. 24, no. 2, pp. 117-122, 2002.

[19] D. O. Halwani, P. G. Anderson, B. C. Brott, A. S. Anayiotos and J. E. Lemons, "Surface characterization of explanted endovascular stents:Evidence of in vivo corrosion," *J. Biomed. Mater. Res. B,* vol. 95, no. 1, pp. 225-238, 2010.

[20] P. Filip, J. Lausmaa, J. Muisalek and K. Mazanec, "Structure and surface of TiNi human implants," *Biomaterials,* vol. 22, no. 1, pp. 2131-2138, 2001.

[21] S. J. Sullivan, D. Madamba, S. Sivan, K. Miyashiro, M. L. Dreger, C. Trepanier and S. Nagaraja, "The effects of surface processing on in-vivo corrosion of Nitinol stents in a porcine model," *Acta Biomater,* vol. 62, no. 1, pp. 385-396, 2017.

[22] E. McLucas, Y. Rochev, W. M. Carroll and T. J. Smith, "Analysis of the Effects of Surface Treaments on Nickel Release from Nitinol Wires and Their Impacts on Candidate Gene Expression in Endothelial Cells," *J Matter Sci Med,* vol. 19, no. 3, pp. 975-980, 2008.

[23] C. C. Shih, S. J. Lin, Y. L. Chen, Y. Y. Su, S. T. Lai, G. J. Wu, C. F. Kwok and K. H. Chung, "The cytotoxicity of corrosion products of nitinol stent wireon cultured smooth muscle cells," *J Biomed Mater Res,* vol. 51, no. 1, pp. 395-403, 2000.

[24] M. W. Ries, C. Kampmann, H. J. Rupprecht, G. Hintereder, G. Hafner and J. Meyer, "Nickel Release after implantation of Amplatzer occluder," *Am Heart J,* vol. 145, no. 4, pp. 737-741, 2003.

[25] M. Es-Souni, M. Es-Souni and H. Fischer-Brandies, "Assessing the biocompatibility of NiTi shape memory alloys used for medical applications," *Anal Bioanal Chem,* vol. 381, no. 1, pp. 557-567, 2005.

[26] S.A. Shabalovskaya, "On the nature of the biocompatibility and on medical applications of NiTi shape memory and superelastic alloys," *Biomed. Mater. Eng.,* vol. 6, no. 4, pp. 267-289, 1996.

[27] S. J. Sullivan, M. L. Dreher, J. Zheng, L. Chen, D. Madamba, H. Miyashiro, C. Trepanier and S. Nagaraja, "Effects of Oxide Layer Composition and Radial Compression on Nickel Release in Nitinol Stents," *Shap. Mem. Superelasticity (,* vol. 1, no. 1, pp. 319-327, 2015.

[28] S. Shabalovskaya, J. Anderegg and J. V. Humbeeck, "Critical overview of Nitinol surfaces and their modifications for medical applications," *Acta Biomater.,* vol. 4, no. 1, pp. 447-467, 2008.

[29] C. M. Chan, S. Trigwell and T. Duerig, "Oxidation of a NiTi Alloy," *Surf. Interface Anal.,* vol. 15, no. 1, pp. 349-354, 1990.

[30] A. W. Hansen, L. V. R. Beltrami, L. M. Antonini, D. J. Villarinhn, J. C. K. d. Neves, C. E. B. Marino and C. d. F. Malfatti, "Oxide Formation on NiTi Surface: Influence of the Heat Treatment Time to Achieve the Shape Memory," *Matl. Res.,* vol. 18, no. 5, pp. 1053-1061, 2015.

[31] C. L. Chu, C. Y. Chung and P. K. Chu, "Surface oxidation of NiTi shape memory alloy in a boiling aqueous solution containing hydrogen peroxide," *Mater. Sci. Eng. A.,* vol. 417, no. 1, pp. 104-109, 2006.

[32] S. Barison, S. Cattarin, S. Daolio, M. Musiani and A. Tuissi, "Characterisation of surface oxidation of nickel–titanium alloy by ion-beam and electrochemical techniques," *Electrochim. Acta,* vol. 50, no. 1, pp. 11-18, 2004.

[33] M. M. Patel and R. F. Gordon, "An Investigation of Diverse Surface Finishes on Fatigue Properties of Superelastic Nitinol Wire," in *The International Conference on Shape Memory and Superelastic Technologies*, Pacific Grove, 2006.

[34] H. Nan, Y. Ping, C. Xuan, L. Yongxang, Z. Xiolan, C. Guangjun, Z. Zihong, Z. Feng, C. Yuanru, L. Xianghuai and X. Tingfei, "Blood compatibility of amorhpous titanium oxide films synthesized by ion bean enhanced depostition," *Biomater,* vol. 19, no. 1, pp. 771-776, 1998.

[35] S. A. Shabalovskaya, J. Anderegg, F. Laab, P. A. Thiel and G. Rondelli, "Surface Conditions of Nitinol Wires, Tubing, and As-Cast Alloys. The Effect of Chemical Etching, Aging in Boiling Water, and Heat Treatment," *J. Biomed. Mater. Res. B,* vol. 65, no. 1, pp. 193-203, 2002.

[36] C. L. McBee and J. Kruger, "Nature of passive films on iron-chromium alloys," *Electrochim. Acta.,* vol. 17, no. 8, pp. 1337-1341, 1972.

[37] C. C. Shih, S. J. Lin, K. H. Chung, Y. L. Chen and Y. Y. Su, "Increased corrosion resistance of stent materials by converting current surface film of polycrystalline oxide into amorphous oxide," *J. Biomed. Mater. Res,* vol. 52, no. 2, pp. 323-332, 2000.

[38] Z. Szklarska-Smialowska, “Pitting Corrosion of Aluminum,” *Corros. Sci.,* vol. 41, no. 1, pp. 1743-1767, 1999.

[39] E. McCafferty, “Electrochemical Basis for Passivity,” in *Introduction to Corrosion Science*, New York, Springer, 2010, pp. 209-213.

[40] S. A. Shabalovskaya and J. W. Anderegg, “Surface spectroscopic characterization of TiNi nearly equiatomic shape memory alloys for implants,” *J. Vac. Sci. Technol.,* vol. 13, no. 5, pp. 2624-2632, 1995.

[41] S. Shabalovskaya, G. Rondelli, J. Anderegg, B. Simpson and S. Budko, “Effect of Chemical Etching and Aging in Boiling Water on the Corrosion Resistance of Nitinol Wires with Black Oxide Resulting from Manufacturing Process,” *J. Biomed. Mater. Res. B,* vol. 66, no. 1, pp. 331-340, 2002.

[42] A. Michiardi, C. Aparicio, J. A. Planell and F. J. Gil, “New Oxidation Treatment of NiTi Shape Memory Alloys to ObtainNi-Free Surfaces and to Improve Biocompatibility,” *J. Biomed. Mater. Res. B,* vol. 77, no. 2, pp. 249-256, 2006.

[43] P. E. Klages, Z. Bai, M. Lobban, M. K. Rotermund and H. H. Rotermund, “Enhancing resistance to pitting corrosion in mechanically polished stainless steel 316,” *Electrochem. Common.,* vol. 15, no. 1, pp. 54-58, 2012.

[44] J. Pan, D. Thierry and C. Leygraf, “Hydrogen peroxide toward enhanced oxide growth on titanium in PBS solution: Blue coloration and clinical relevance,” *J. Biomed. Mater. Res. A,* vol. 30, no. 3, pp. 393-402, 1996.

[45] S. A. Shabalovskaya, J. W. Anderegg, A. Undisz, M. Rettenmayr and G. C. Rondelli, “Corrosion resistance, chemistry, and mechanical aspects of Nitinol surfaces formed in hydrogen peroxide solutions,” *J Biomed Mater Res Part B,* vol. 100, no. 6, pp. 1490-1499, 2012.

[46] C. L. Chu, S. K. Wu and Y. C. Yen, “Oxidation behavior of equiatomic TiNi alloy in high temperature air environment,” *Mater. Sci. Eng.,* vol. 216, no. 1, pp. 193-200, 1996.

[47] Z. Bai and H. Rotermund, “The intrinsically high pitting corrosion resistance of mechanicallypolished nitinol in simulated physiological solutions,” *J. Biomed. Mater. Res. B,* vol. 99, no. 1, pp. 1-13, 2011.

[48] W. Theisen and A. Schuermann, “Electro discharge machining of nickel–titanium shape memory alloys,” *Mater. Sci. Eng. A.,* vol. 378, no. 1, pp. 200-204, 2003.

[49] M. Wohlschlögel, R. Steegmuller and A. Schubler, “Effect of Inclusion Size and Distribution on the Corrosion Behavior of Medical-Device Grade Nitinol Tubing,” *J. Mater. Eng. Perform,* vol. 23, no. 7, pp. 2635-2640, 2014.

[50] B.G. Pound, “Pit initiation on nitinol in simulated physiological solutions,” *J. Biomed. Mater. Res. B,* vol. 106, no. 4, pp. 1605-1610, 2019.

[51] S. Shabalovskaya, G. Rondelli, J. Anderegg, J. P. Xiong and M. Wu, “Comparative Corrosion Performance of Black Oxide,Sandblasted, and Fine-Drawn Nitinol Wires in Potentiodynamicand Potentiostatic Tests: Effects of Chemical Etching andElectropolishing,” *J. Biomed. Mater. Res. B,* vol. 69, no. 2, pp. 223-231, 2004.

[52] S. A. Shabalovskaya, G. C. Rondelli, A. L. Undisz, J. W. Anderegg, T. D. Burleigh and M. E. Rettenmayr, “The electrochemical characteristics of native Nitinol surfaces,” *Biomaterials,* vol. 30, no. 1, pp. 3662-3671, 2009.

[53] B.G. Pound, “The electrochemical behavior of nitinol in simulated physiological solutions,” *J. Biomed. Mater. Res. A,* vol. 85, no. 4, pp. 1103-1113, 2007.

[54] L. E. Eiselstein, D. Steffey, A. Nissan, N. Corlett, R. Dugnani, E. Kus and S. G. Stewart, “Acceptance Criteria for Corrosion Resistance of Medical Devices: Statistical Analyisis of Nitino. Pitting in Vivo Enviroments,” *J Mater Eng Perform,* vol. 18, no. 5, pp. 768-780, 2009.

[55] B. Thierry, M. Tabrizian, O. Savadogo and L. H. Yahia, “Effect of surface treatment and sterilization processes onthe corrosion behavior of NiTi shape memory alloy,” *J. Biomed. Mater. Res. B,* vol. 51, no. 4, pp. 685-693, 2000.

[56] B.G. Pound, “Susceptibility of nitinol to localized corrosion,” *J. Biomed. Mater. Res. A,* vol. 77, no. 1, pp. 185-1911, 2005.

[57] A. Tuissi, G. Rondelli and P. Bassani, “Plasma arc melting (PAM) and corrosion resistance of pure NiTi shape memory alloys,” *Shap. Mem. Superelasticity,* vol. 1, no. 1, pp. 50-57, 2015.

[58] X. Zhang, Z. H. Jiang, Z. Yao, Y. Song and Z. D. Wu, “Effects of Scan Rate on the Potentiodynamic Polarization Curve Obtained to Determine the Tafel Slopes and Corrosion Current Density,” *Corros. Sci.,* vol. 51, no. 3, pp. 581-587, 2009.

[59] T. T. Lunt, J. R. Scully, V. Brusamarello, A. S. Mikhailov and J. L. Hudson, “Spatial Interactions among Localized Corrosion Sites Experiments and Modeling,” *J. Electrochim. Soc,* vol. 149, no. 5, pp. 163-173, 2002.

[60] B. Wu, J. R. Scully and J. L. Hudson, “Cooperative Stochastic Behavior in Localized Corrosion,” *Electrochim. Acta.,* vol. 144, no. 5, pp. 1614-1620, 1997.

[61] T. T. Lunt, S. T. Pride, J. R. Scully and J. L. Hudson, “Cooperative Stochastic Behavior in Localized Corrosion,” *J. Electrochem. Soc.,* vol. 144, no. 5, pp. 1620-1629, 1997.

[62] T. T. Lunt, V. Brusamarello, J. R. Scully and J. L. Hudson, “Interactions among Localized Corrosion Sites Investigated with Electrode Arrays,” *Electrochem. Solid State Lett.,* vol. 3, no. 6, pp. 271-274, 2000.

[63] C. Punckt, M. Bolscher, H. H. Rotermund, A. S. Mikhailov, L. Organ, N. Budiansky, J. R. Scully and J. L. Hudson, “Sudden Onset of Pitting Corrosion on Stainless Steel as a Critical Phenomenon,” *Science,* vol. 305, no. 1, pp. 1133-1135, 2004.

[64] M. Dornhege, C. Punckt, J. L. Hudson and H. H. Rotermund, “Spreading of corrosion on stainless steel simultaneous observation of metastable pits and oxide film,” *J. Electrochem. Soc,* vol. 154, no. 1, pp. C24-C27, 2007.

[65] G. Williams, N. Birbillis and H. N. McMurray, “Controlling factors in localised corrosion morphologies observed for magnesium immersed in chloride containing electrolyte,” *Faraday Discuss,* vol. 180, no. 1, pp. 313-330, 2015.

[66] G. Williams and H. N. McMurray, “Localized Corrosion of Magnesium in Chloride-Containing Electrolyte Studied by a Scanning Vibrating Electrode Technique,” *J. Electrochem. Soc.,* vol. 155, no. 7, pp. C340-C349, 2008.

[67] P. W. Chan, E. L. Mire and E. A. Marquis, “Microstructure of localized corrosion front on Mg alloys and the relationship with hydrogen evolution,” *Corros. Sci.,* vol. 128, no. 1, pp. 253-264, 2017.

[68] “Standard Reference Test Method for Making Potentiostatic and Potentiodynamic Anodic Polarization Measurements,” *ASTM Standards G5 – 94,* 2011.

[69] M. Birkholz, “Grazing Incidence Configurations,” in *Thin Film Analysis by X-Ray Scattering*, Weinheim, Wiley-VCH, 2006, pp. 143-165.

[70] P. E. Klages, M. K. Rotermund and H. H. Rotermund, “Simultaneous holographic, ellipsometric, and optical imaging of pitting corrosion on SS 316LVM stainless steel,” *Corros. Sci.,* vol. 65, no. 1, pp. 128-135, 2012.

[71] A. P. Grosvenor, M. C. Biesinger, R. S. Smart and N. S. McIntyre, “New Interpretations of XPS spectra of nickel and oxides,” *Surf. Sci,* vol. 600, no. 1, pp. 1770-1779, 2006.

[72] M. C. Biesinger, B. P. Payne, L. W. M. Lau, A. Gerson and R. S. Smart, “X-ray photoelectron spectroscopic chemical state quantification of mixed nickel metal, oxide and hydroxide systems,” *Surf. Interface. Anal,* vol. 41, no. 1, pp. 324-332, 2009.

[73] M. C. Biesinger, L. W. M. Lau, A. R. Gerson and R. S. Smart, “Resolving surface chemistry states in XPS analysis of first row transition metals, oxides and hydroxides: Sc, Ti, V, Cu and Zn,” *Appl. Surf. Sci.,* vol. 257, no. 1, pp. 887-898, 2010.

[74] E. Ghali, “Aluminum and Aluminum Alloys,” in *Uhlig's Corrosion Handbook*, R. W. Revie, Ed., Pennington, Wiley, 2011, pp. 715-745.

[75] M. C. Reboul, T. J. Warner, H. Mayer and B. Baroux, “A Ten Step Mechanism For The Pitting Corrosion of Aluminum Alloys,” *Corros. Rev.,* vol. 15, no. 3, pp. 471-495, 2011.

[76] B. Wang, L. Zhang, Y. Su, Y. Xiao and J. Liu, “Corrosion Behavior of 5A05 Aluminum Alloy in NaCl Solution,” *Acta. Metall. Sin.,* vol. 26, no. 5, pp. 581-587, 2013.

[77] A. Aballe, M. Behencourt, F. J. Botana, M. J. Cano and M. Marcos, “Influence of cathodic intermetallics distribution on the reproducibility of the electrochemical measurements on AA5083 alloy in NaCl solutions,” *Corros. Sci.,* vol. 45, no. 1, pp. 161-180, 2003.

[78] S. T. Pride, J. R. Scully and J. L. Hudson, “Metastable Pitting of Aluminum and Criteria for the Transition to Stable Pit Growth,” *J. Electrochem. Soc.,* vol. 141, no. 11, pp. 3028-3040, 1994.

[79] J.H.W. de Wit, “New knowledge on localized corrosion obtained from local measuring techniques,” *Electrochim. Acta.,* vol. 46, no. 1, pp. 3641-3650, 2001.

[80] U. Donatus, G. E. Thompson, J. A. Omotoyinbo, K. K. Alaneme, S. Aribo and O. G. Agbabiaka, “Corrosion pathways in aluminium alloys,” *Trans. Noferrous. Met. Soc. China,* vol. 27, no. 1, pp. 55-62, 2017.

[81] M. Baumgartner and H. Kaesche, “Aluminum pitting in chloride solutions: morphology and pit growth kinetics,” *Corros. Sci.,* vol. 31, no. 1, pp. 231-236, 1990.

[82] R.C. Newman, “Local chemistry considerations in the tunnelling corrosion of aluminium,” *Corros. Sci.,* vol. 37, no. 3, pp. 527-533, 1995.

[83] B. Evgeny, T. Hughes and D. Eskin, “Effect of surface roughness on corrosion behaviour of low carbon steelin inhibited 4 M hydrochloric acid under laminar and turbulent flow conditions,” *Corros. Sci.,* vol. 103, no. 1, pp. 196-205, 2016.

[84] P.V. Scheers, “The effects of flow velocity and pH on the corrosion rate of mild steel in a synthetic minewater,” *J. S. Afr. Inst. Min. Metall,* vol. 92, no. 10, pp. 275-281, 1992.

[85] H.R. Copson, “Effect of Velocity on Corrosion by Water,” *Ind. Eng. Chem,* vol. 44, no. 8, pp. 1745-1752, 1952.

[86] T. E. Wight and H. P. Godard, “Laboratory Studies on the pitting of aluminum in aggresive waters,” *Corrosion,* vol. 10, no. 1, pp. 195-198, 1954.

[87] G.A. Gehring, “Corrosion of Aluminum Alloys in High Velocity Seawater,” Deparment of the Navy Office of Naval Research Metallurgy Program, Arlington, 1979.

[88] L. Organ, J. R. Scully, A. S. Mikailov and J. L. Hudson, “A spatiotemporal model of interactions among metastable pits and the transition to pitting corrosion,” *Electrochim. Acta.,* vol. 51, no. 1, pp. 225-241, 2005.